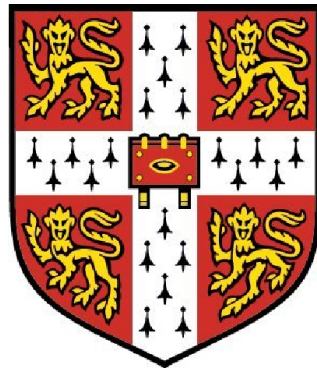


Optoelectronic and photonic control of single quantum dots



Samuel James Dewhurst

Wolfson College

University of Cambridge

A thesis submitted for the degree of

Doctor of Philosophy

April 2010

Declaration

This thesis describes work carried out in the Semiconductor Physics Group at the Cavendish Laboratory and the Cambridge Research Laboratory of Toshiba Research Europe Limited, from October 2006 to March 2010.

This dissertation is the result of my own work and contains nothing which is the outcome of work done in collaboration except where specifically indicated in the text. It has not been submitted in part, or as a whole, for any degree at this, or any other, university. It does not exceed 60,000 words.

S. J. Dewhurst, April 2010

Publications

Slow-light-enhanced single quantum dot emission in a unidirectional photonic crystal waveguide

S. J. Dewhurst, D. Granados, D. J. P. Ellis, A. J. Bennett, R. B. Patel, I. Farrer, D. Anderson, G. A. C. Jones, D. A. Ritchie and A. J. Shields
Applied Physics Letters **96**, 031109 (2010).

Oxide-apertured microcavity single-photon-emitting diodes: simultaneous confinement of current and light

D. J. P. Ellis, A. J. Bennett, S. J. Dewhurst, P. Atkinson, C. A. Nicoll, D. A. Ritchie and A. J. Shields
Journal of Physics: Condensed Matter **20**, 454212 (2008).

Cavity-enhanced radiative emission rate in a single-photon-emitting diode operating at 0.5 GHz

D. J. P. Ellis, A. J. Bennett, S. J. Dewhurst, C. A. Nicoll, D. A. Ritchie and A. J. Shields
New Journal of Physics **10**, 043035 (2008).

Single electron-spin memory with a semiconductor quantum dot

R. J. Young, S. J. Dewhurst, R. M. Stevenson, P. Atkinson, A. J. Bennett, M. B. Ward, K. Cooper, D. A. Ritchie and A. J. Shields
New Journal of Physics **9**, 365 (2007).

Controlling the polarization correlation of photon pairs from a charge-tunable quantum dot

R. J. Young, S. J. Dewhurst, R. M. Stevenson, A. J. Shields, P. Atkinson, K. Cooper and D. A. Ritchie

Applied Physics Letters **91**, 011114 (2007).

Acknowledgements

This work would not have been possible without the help and expertise of a number of people.

I'd like to thank Andrew Shields and David Ritchie for their supervision and guidance throughout my PhD. Thanks must also go to EPSRC and Toshiba Research Europe Ltd. for financial support.

I have been fortunate enough to work with Daniel Granados for the majority of my time in Cambridge, and I am very grateful for all his help and advice. I am also particularly indebted to Robert Young for assistance in the early stages of this work, David Ellis for his help with processing and Anthony Bennett for many useful discussions. I'd also like to thank Mark Stevenson, Martin Ward, Raj Patel and Niklas Skold for their assistance at various stages.

Ian Farrer and Christine Nicoll were responsible for the growth of the samples in this work, David Anderson performed the electron beam lithography, and Ken Cooper processed the samples used in Chapter 4, my thanks go to all of you.

Warmest thanks go to everyone at Toshiba, the Cavendish and Wolfson College who I have had the pleasure to live and work with over the last few years.

Finally, I'd like to thank my parents for their support and encouragement over the years.

Summary

The area of quantum information promises to deliver a range of new technologies in the fields of quantum computing and quantum communication. Devices based on semiconductor quantum dots hold great potential for the practical realisation of many of the components required in the proposed schemes.

This thesis describes the development of several quantum dot devices. By integrating a quantum dot into a *p-i-n* diode, it was possible to control the dominant emission lines in its photoluminescence spectrum and to maximise the degree of polarisation correlation between the two photons emitted in the biexciton decay. With the same device under a magnetic field, a digital memory was demonstrated. The polarisation information of a single photon was stored as the spin of an electron inside the quantum dot, and was deterministically recovered some time later by the application of an electrical trigger.

A fabrication process was developed in order to produce high quality two dimensional slab photonic crystals operating with a photonic band gap at ~ 900 nm. By placing a quantum dot into an appropriately designed H1 photonic crystal cavity, strong coupling was achieved between the dot and the monopole mode of the cavity. The vacuum Rabi splitting was found to be constant for all linear polarisations due to the unpolarised nature of the far-field of the mode.

Finally, a new kind of cavity based on photonic crystal waveguides was developed. A Purcell enhancement of the in-plane spontaneous emission from a quantum dot coupled to a unidirectional photonic crystal waveguide was demonstrated.

Contents

Declaration	i
Publications	ii
Acknowledgements	iv
Summary	v
1 Introduction	1
2 Background and Theory	3
2.1 Overview	3
2.2 Semiconductor quantum dots	3
2.2.1 Optical properties of single semiconductor quantum dots	5
2.2.2 Quantum dots as single photon sources	7
2.2.3 Fine structure	7
2.2.4 Quantum dots as sources of entangled photon pairs	8
2.2.5 Applied magnetic field	10
2.3 Quantum dots in cavities	10
2.3.1 Quantum dot-cavity coupling	11
2.3.2 Weak coupling	12
2.3.3 Strong coupling	14
2.3.4 Types of cavities	15
2.4 Photonic crystals	18
2.4.1 Photonic band gap	19
2.4.2 Photonic crystal cavities	19

2.4.3	Two-dimensional photonic crystals	20
2.4.4	Practical considerations	23
3	Experimental techniques	25
3.1	Overview	25
3.2	Sample growth and basic preparation	25
3.2.1	Quantum dot growth	25
3.2.2	Isolating single quantum dots	26
3.3	Optical techniques	27
3.3.1	Micro-photoluminescence spectroscopy	27
3.3.2	Time-resolved photoluminescence	29
3.3.3	Auto-correlations	30
3.3.4	Cross-correlations	32
3.3.5	Application of a magnetic field	32
3.4	Spectroscopy of quantum dots	34
3.4.1	Power dependence	34
3.4.2	Polarization of excitons	36
4	<i>p-i-n</i> diode quantum dot devices	37
4.1	Overview	37
4.2	Sample design and operation	37
4.3	Controlling the polarisation correlation of photon pairs	40
4.3.1	Degree of polarisation correlation	41
4.3.2	Lifetime measurements	44
4.3.3	Polarisation correlation control	44
4.4	Single quantum dot memory	45
4.4.1	Quantum information processing	45
4.4.2	Device operation	46
4.4.3	Experimental set-up	48
4.4.4	Quantum dot electron-spin memory	49
4.4.5	Summary and outlook	53

5	Designing and fabricating photonic crystals	55
5.1	Overview	55
5.2	Finite-difference time-domain simulation	55
5.3	FDTD for photonic crystals	57
5.3.1	Boundary conditions	57
5.3.2	Calculating the spectrum	57
5.3.3	Q -factor	59
5.3.4	Mode profile	60
5.3.5	Mode volume	60
5.3.6	Purcell factor	61
5.3.7	Simulation convergence studies	61
5.4	Fabrication of photonic crystals	63
5.4.1	Initial process	64
5.4.2	Electron beam resist	65
5.4.3	AlGaAs sacrificial layer	68
5.4.4	Dry etching	71
5.5	Summary and outlook	75
 6	 H1 photonic crystal cavities for strong coupling	 76
6.1	Overview	76
6.2	H1 mode structure	77
6.3	Design and optimisation	79
6.3.1	Bulk hole radii	79
6.3.2	Nearest neighbour hole radius	80
6.3.3	Slab height	81
6.3.4	Optimised cavity	82
6.4	Fabrication	83
6.5	Optical characterisation	83
6.5.1	Mode structure	83
6.6	Weak coupling	86
6.7	Strong coupling	88
6.8	Polarisation dependence	92
6.9	Summary and outlook	93

7	Unidirectional photonic crystal waveguides	94
7.1	Overview	94
7.2	Photonic crystal waveguide mode structure	95
7.3	Design and optimisation	98
7.3.1	Basic parameters	98
7.3.2	Hole radius	99
7.3.3	Slab height	100
7.3.4	Optimised waveguide	103
7.4	Fabrication	103
7.5	Optical characterisation	105
7.6	Purcell effect	107
7.7	Further work	109
7.8	Summary and outlook	111
8	Conclusions	112
A	Photonic band gap	115
	References	138

Chapter 1

Introduction

The term ‘quantum information’ refers to physical information which is encoded in a quantum system. Encoding information in this way opens up new methods of transferring and manipulating data based on the laws of quantum mechanics. Using light as the quantum system has allowed advances in quantum key distribution and photonic quantum computing [119].

Quantum key distribution involves sharing a cryptographic key between two parties in perfect secrecy [47]. By using single photons to transmit the key in schemes such as the BB84 protocol [16, 139], it is possible to detect the presence of any eavesdroppers. Through quantum teleportation [23], future quantum networks could distribute keys over longer distances or through more complex topologies [25].

Quantum computing takes advantage of quantum mechanical phenomena to perform operations on data that would not be possible with classical systems. Certain classes of problems, such as factorising large numbers [122], could be performed far more efficiently with a quantum computer. Future practical implementations may rely on quantum states of light, as for example in the linear-optics quantum computing scheme [69, 70].

These applications will require efficient sources of single photons and entangled photon pairs [85, 119]. The probabilistic process of parametric down conversion in nonlinear crystals can be used to produce heralded single photons [53] and entangled photon pairs [24, 104, 120], although these are not on-demand sources. Furthermore, there is a finite probability of producing more than one photon/pair

at a time, so that the pump power must be very low which degrades the source efficiency. Several systems have been proposed to create efficient on-demand true single photon sources, including ensembles of atoms [67], single ions [32], fluorescent molecules [11, 27], nitrogen vacancies in diamond [76], quantum wells [64] and nanocrystals [86].

Semiconductor quantum dots have proved to be an excellent source of single photons [15, 94, 116, 151], and it has recently been shown that they can produce single pairs of polarisation entangled photons on-demand [130]. They offer compact and robust solid state sources which can be readily integrated with other semiconductor technology. For example, they can be grown in *p-i-n* diode structures to achieve electrically driven sources [151]. Furthermore, it is relatively straight forward to integrate quantum dots into optical cavity structures which are essential to improve source efficiencies.

Other quantum dot-based devices may find uses as other components in quantum information schemes [96, 153], such as quantum memories [22], quantum gates [35, 58] and single photon detectors [13, 21].

In this thesis, a number of quantum dot devices are investigated. In chapter 2, the relevant theory concerning quantum dots and optical cavities is set out. Chapter 3 contains descriptions of the experimental techniques used throughout this work. The operation of a device based on a quantum dot embedded in a *p-i-n* diode is discussed in chapter 4. Chapter 5 concentrates on the development of a process to fabricate two-dimensional slab photonic crystals to enhance the performance of quantum dot devices. In chapter 6, strong coupling between a quantum dot and a H1 photonic crystal cavity is demonstrated. Chapter 7 focuses on experiments with unidirectional photonic crystal waveguides. Finally, some concluding remarks are made in chapter 8.

Chapter 2

Background and Theory

2.1 Overview

In this chapter, the relevant background to the rest of the thesis will be set out. Firstly the properties of semiconductor quantum dots will be discussed. This will be followed by the details of their integration into optical cavities. Finally a discussion about photonic crystals and the use of them to create cavities will be presented.

2.2 Semiconductor quantum dots

A semiconductor quantum dot (QD) is a nanometre sized island of a semiconductor material embedded in another material which has a larger band gap [19]. It effectively forms a potential well in which electrons and holes can be trapped in three dimensions (see figure 2.1). The dimensions of a quantum dot are smaller than the de Broglie wavelength of trapped electrons and holes, so the carriers are quantum confined and the energy levels available to them are quantized.

The focus of this work is on InAs QDs embedded in GaAs grown by molecular beam epitaxy (see section 3.2.1). When InAs is epitaxially grown on GaAs, it initially experiences a strain due to the lattice mismatch between the two crystals. After a certain critical thickness of InAs is deposited, this strain cause the InAs

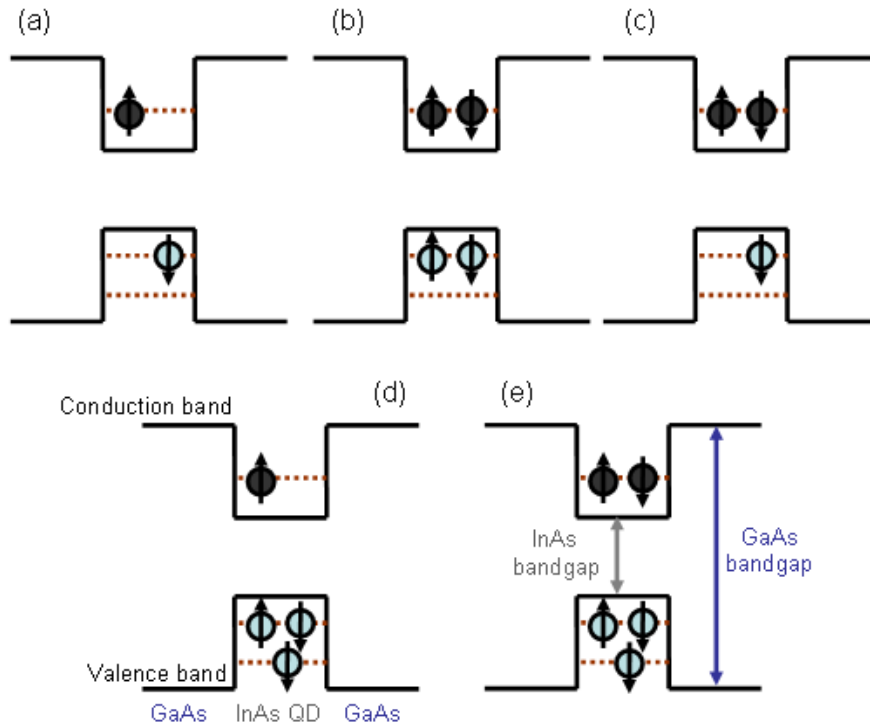


Figure 2.1: Simplified band diagrams of a single quantum dot exciton states; (a) exciton (X), (b) biexciton ($2X$), (c) negatively charge exciton (X^-), (d) doubly positively charged exciton(X^{2+}), (e) positively charged biexciton($2X^+$). The dashed red lines represent the available energy levels for carriers confined in the dot. Dark gray circles represent electrons and light blue circles represent holes. The arrows associated with each of the carriers indicate the possible spin states of the carriers.

to break up into small nano-scale islands. Overgrowth with more GaAs completes the formation of quantum dots.

A QD can be populated with carriers by electrical injection or by the optical excitation of an electron into the conduction band leaving a hole in the valence band. This latter method can be achieved by exciting an electron resonantly inside the dot, or by exciting carriers in the surrounding material and relying on the fact that some of them will relax into the lower potential energy dot levels via phonon interactions [92].

Previous studies have shown that the InAs dots studied here can hold one or two quantized energy levels for each carrier [133] (e.g. the QDs in Figure 2.1 contain one electron energy level and two hole energy levels), although larger dots may have more. Since electrons and holes are fermions, the Pauli exclusion principle requires that each energy level can only be occupied by two carriers with opposite spins. There are therefore only a small number of possible configurations of carriers that the dot can accommodate. These configurations are known as the excitonic states of the QD. Figure 2.1 shows a number of possible excitonic states including the neutral exciton (Figure 2.1(a)), the biexciton (Figure 2.1(b)) and the negatively charged exciton (Figure 2.1(c)).

2.2.1 Optical properties of single semiconductor quantum dots

The recombination of an electron and a hole inside a dot leads to the emission of a single photon with an energy equal to the difference between the energies of the initial and final excitonic states [93]. The energy of each excitonic state is, in turn, determined by the complex Coulomb and exchange interactions between its constituent carriers [92]. Therefore, the emission from a single QD consists of a number of separate spectral lines, each corresponding to the decay of a different excitonic state.

For example the biexciton can decay - by the recombination of an electron and a hole and the emission of a photon - to the exciton. The energy of the biexciton photon will differ from the energy of the subsequently emitted exciton photon as the exciton decays to the ground state (see Figure 2.2).

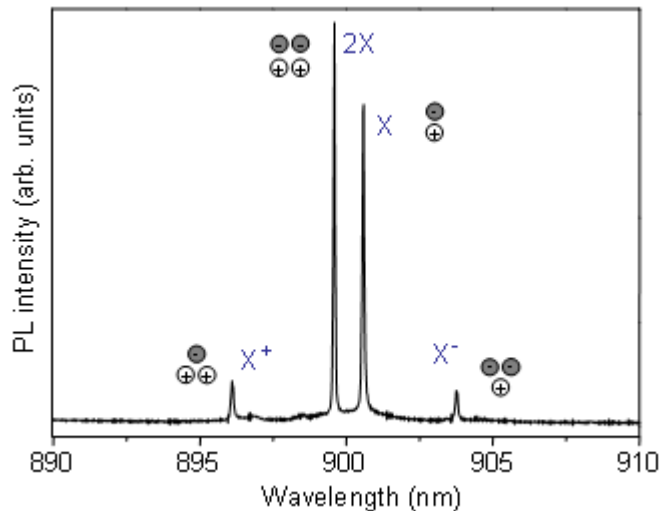


Figure 2.2: Typical spectrum of the emission from a single quantum dot. Each spectral line corresponds to the decay of a different exciton state in the QD by the radiative recombination of an electron and a hole, as indicated.

The optical properties of QDs are in fact very similar to atoms. However, QDs are much larger and can be integrated into solid state structures to allow a range of photonic semiconductor devices.

The typical decay rate for e.g. the neutral exciton from the QDs studied in this work is $\gamma_X \sim 1$ GHz, which is equivalent to a radiative lifetime of $\tau_{r,X} = 1/\gamma_X = 1$ ns. This finite lifetime leads to radiative broadening of the resulting spectral line as compared to the monochromatic ideal. This can be approximately understood by considering the energy-time uncertainty principle, $\Delta U \tau_r \gtrsim \hbar$, which implies that

$$\Delta\omega = \frac{\Delta U}{\hbar} \gtrsim \frac{1}{\tau_r}. \quad (2.1)$$

Here, ΔU is the uncertainty in the emission energy and $\Delta\omega$ is the spectral line width. The emission lines from individual QDs take the form of Lorentzian line shapes. The radiative line width is the minimum possible width; the emission

may be further broadened by e.g. non-radiative relaxation processes due to interactions with phonons or charges in the vicinity of the QD.

2.2.2 Quantum dots as single photon sources

QDs are ideally suited to being used as single photon sources [93, 133, 152]. When an electron and a hole radiatively recombine, some finite period of time is needed before the QD can be repopulated with carriers to reform the initial excitonic state and then decay again. Therefore only one photon can be emitted at a time.

The single photon properties can be further improved, and deterministic control can be gained by implementing a pulsed excitation scheme. Since the lifetimes of the excitonic states in QDs are much longer than the lifetimes of the photo-excited carriers in the surrounding semiconductor, and given an excitation pulse that is much shorter than the lifetime of the excitonic state (easily achievable with both optical [94] and electrical [151] excitation schemes), only one photon can be emitted per excitation pulse.

2.2.3 Fine structure

Exciton fine structure

The character of the holes confined by QDs is typically heavy [12]. The angular momentum of a heavy hole is $j_{hh} = 3/2$ and the spin of an electron is $s_e = 1/2$. Therefore the exciton's total angular momentum projection in the z direction is $m_{ex} = s_e^z + j_{hh}^z = \pm 1$ or ± 2 . The angular momentum of a single (circularly polarized) photon is $j_{ph} = \pm 1$. Thus due to the conservation of angular momentum, only the exciton states with $m_{ex} = \pm 1$ can decay radiatively, emitting a single photon. These exciton states are known as bright excitons, whereas the other states with $m_{ex} = \pm 2$ cannot normally couple to single photons and are known as dark excitons. These two doublets are split in energy by the electron-hole exchange interaction; the dark exciton doublet has lower energy since the angular momentum of the hole and the spin of the electron are aligned in this case (see left side of figure 2.3).

An InAs QD is generally elongated along one of the in-plane crystal axes (i.e. lens shaped) and there is an asymmetry in the inbuilt strain of the dot which remains after the strain relaxing QD formation. Furthermore GaAs exhibits piezoelectricity, and differing electric fields are experienced along the different crystal axes due to its structure. These asymmetries give rise to anisotropic exchange interactions between the carriers in the dot. This causes each of the exciton doublets, $m_{ex} = \pm 1$ and $m_{ex} = \pm 2$, to hybridize, so that the emission from each of them becomes linearly polarised with distinct polarisations parallel to the [110] and [1-10] axes of the crystal [43, 74] (labeled π_x and π_y respectively in figure 2.3). The two polarisations are furthermore split in energy, known as the fine structure splitting and denoted by S_0 .

Biexciton

The biexciton consists of two anti-aligned electrons and two anti-aligned holes which have zero total spin and angular momentum respectively. Therefore there is no electron-hole exchange interaction and the state is non-degenerate. The biexciton can decay by the emission of a single photon to either one of the bright $m_{ex} = \pm 1$ exciton states. Thus the biexciton line also exhibits a splitting in an equal and opposite sense to the exciton line.

2.2.4 Quantum dots as sources of entangled photon pairs

The decay of the biexciton to the ground state via the emission of a biexciton photon and an exciton photon can be used to create an entangled photon pair source [130]. If the fine structure splitting of the exciton level is zero (as in the left side of figure 2.3), the two possible biexciton decay paths are indistinguishable and they are entangled. The wavefunction describing the two photons emitted during the biexciton decay is a superposition of the two decay paths and the polarisations of the pair are not well defined until they are measured.

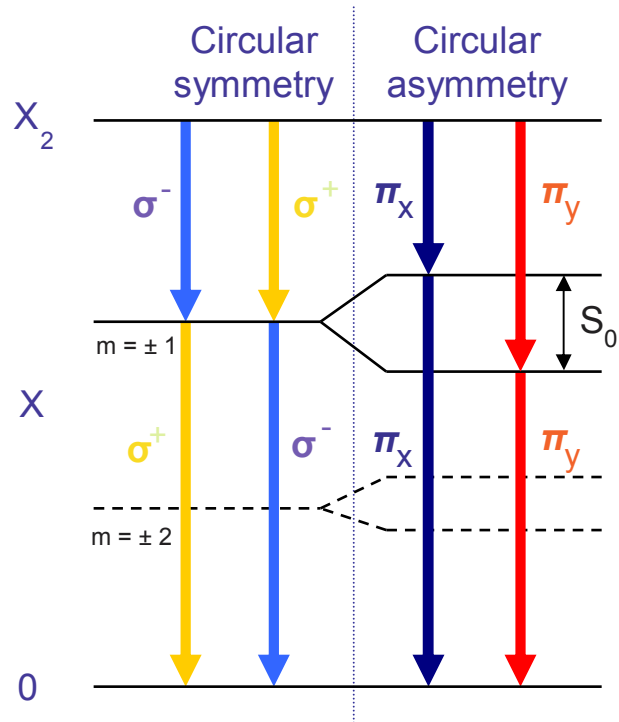


Figure 2.3: Energy level diagram showing the energies of the biexciton and exciton states for symmetric and asymmetric quantum dots. The solid lines indicate bright exciton states, and the dashed lines indicate dark exciton levels. Allowed transitions are indicated by coloured arrows. Asymmetry in the shape of the QD leads to anisotropic exchange interactions between the carriers in the dot, which cause the exciton levels to split. The photons emitted during decay become linearly polarised.

2.2.5 Applied magnetic field

A magnetic field applied to a QD introduces Zeeman interactions between the spins of the electrons and holes, and the field [12]. The effects are highly dependent on the orientation of the field due to the asymmetry of the dot. There are two special cases: the Faraday geometry in which the field is applied parallel to the growth direction of the dots, and the Voigt geometry where the field is applied in the plane of the dots.

Faraday geometry

In this case, the Zeeman interaction simply increases the fine structure splitting. If this increase is large enough, the hybridization of the bright $m_{ex} = \pm 1$ states becomes negligible and the two pure eigenstates of the exciton total angular momentum are recovered.

Voigt geometry

When a large enough magnetic field is applied in the plane of the dots, the dark and bright states become mixed. This causes the dark excitons to become optically active [12, 18].

2.3 Quantum dots in cavities

One of the advantages of working with semiconductor QDs is the relative ease in which they are integrated into optical cavities. Typically only $\sim 2\%$ of the light from a QD is emitted out of the top of a bare wafer because of the large refractive index contrast between the semiconductor and air [153]. This fraction can be substantially increased by directing the emission by coupling it to a mode of a cavity [14, 135]. Furthermore, the spontaneous emission rate of the QD can be enhanced by the Purcell effect [111]. If it is made to be much larger than the dephasing rate of the QD transition, the emitted photons will become indistinguishable - a property which is essential for many quantum information processing applications.

2.3.1 Quantum dot-cavity coupling

The properties of a cavity mode are defined by its resonant frequency, ω_{cav} , and its photon decay rate, κ . The decay rate is a measure of how quickly light stored in the mode is lost. The total optical energy, U , in a mode will decay with time, t , like

$$U = U_0 e^{-t/\tau_{cav}}, \quad (2.2)$$

where $\tau_{cav} = 1/\kappa$ is the cavity mode photon lifetime and U_0 is the energy in the mode at $t = 0$. The spectral width of the mode is controlled by the photon decay rate, $\Delta\omega_{cav} = 1/\tau_{cav} \equiv \kappa$. The quality factor, or Q -factor, of the mode is defined by

$$Q = \omega_{cav}/\Delta\omega_{cav}. \quad (2.3)$$

Higher Q -factors indicate a lower rate of energy loss relative to the energy stored in the mode.

If a QD is surrounded by a cavity with a resonant frequency equal to a transition frequency of the dot, the QD and the cavity will be able to exchange photons in a resonant way. The strength of the interaction between the QD transition and the electric field in the cavity, \mathbf{E} , is quantified by the QD-cavity coupling parameter, g , and is given by the electric dipole interaction,

$$\hbar g = |\langle \mathbf{d} \cdot \mathbf{E} \rangle|, \quad (2.4)$$

where \mathbf{d} is the electric dipole moment of the transition. $\langle \mathbf{d} \cdot \mathbf{E} \rangle$ is the matrix element of the transition between the initial and final states. Assuming that the QD is placed at the maximum of the electric field in the cavity, the QD-cavity coupling parameter can be expressed in terms of the oscillator strength, f , as

$$g = \left(\frac{e^2 f}{4\epsilon_0 \epsilon_r m_0 V_0} \right)^{1/2}, \quad (2.5)$$

where ϵ_r and ϵ_0 are the relative and vacuum permittivity respectively, m_0 is the free electron mass and V_0 is the volume of the cavity mode [112]. Since the oscillator strength is a fixed property of the QDs, for a well positioned QD the coupling parameter is controlled by the volume of the mode. By designing cavities with very small mode volumes, the strength of the coupling can be enhanced.

2.3.2 Weak coupling

When the strength of this interaction is smaller than the losses from the system,

$$g < (\kappa, \gamma_{nr}), \quad (2.6)$$

the QD/cavity is said to be weakly coupled. Here, γ_{nr} is the non-resonant decay rate, which takes account of photons which do not couple to the cavity and non-radiative decay processes in the QD. In this case, the spontaneous emission rate of the transition can be strongly modified. The SE rate from a QD transition, γ , is governed by Fermi's Golden Rule [40]:

$$\gamma = \frac{1}{\tau_r} = \frac{2\pi}{\hbar} |\langle \mathbf{d} \cdot \mathbf{E} \rangle|^2 \rho(\omega), \quad (2.7)$$

where $\rho(\omega)$ is the optical density of states experienced by the QD. $|\langle \mathbf{d} \cdot \mathbf{E} \rangle|^2$ is proportional to the probability that there will be a transition. In free space, the optical density of states is given by

$$\rho(\omega) = \frac{\omega^2 V_0}{\pi^2 c^3}. \quad (2.8)$$

The presence of a cavity increases the density of states at frequencies close to the cavity resonance and restricts it far from resonance. The density of states then takes the form of a normalised Lorentzian function:

$$\rho(\omega) = \frac{2}{\pi \Delta\omega_{cav}} \frac{\Delta\omega_{cav}^2}{4(\omega - \omega_{cav})^2 + \Delta\omega_{cav}^2} \quad (2.9)$$

2.3 Quantum dots in cavities

This equation in conjunction with equation 2.7 implies that the spontaneous emission rate of a weakly coupled QD transition is enhanced for $\omega \approx \omega_{cav}$, and is suppressed for ω far away from ω_{cav} , a phenomenon known as the Purcell effect [111].

The factor by which the spontaneous emission rate is enhanced/suppressed is quantified by the Purcell factor, F_P , which is equal to the ratio between the spontaneous emission rate of the QD transition with and without a cavity. This gives

$$F_P = \frac{\gamma^{cav}}{\gamma^{free}} \equiv \frac{\tau_r^{free}}{\tau_r^{cav}} = \frac{3Q(\lambda/n)^3}{4\pi^2 V_0} \xi^2 \frac{\Delta\omega_{cav}^2}{4(\omega - \omega_{cav})^2 + \Delta\omega_{cav}^2}, \quad (2.10)$$

where λ is the free-space wavelength of the QD emission and n is the refractive index of the material within the cavity. ξ , the normalised dipole orientation factor, is given by

$$\xi = \frac{|\mathbf{E}(\mathbf{r})|}{|\mathbf{E}_{max}|} \cdot \frac{|\mathbf{d} \cdot \mathbf{E}(\mathbf{r})|}{|\mathbf{d}| |\mathbf{E}(\mathbf{r})|}, \quad (2.11)$$

where $\mathbf{E}(\mathbf{r})$ is the electric field experienced by the QD at position \mathbf{r} in the cavity and \mathbf{E}_{max} is the maximum of the electric field in the cavity. ξ quantifies how well the electric dipole of the transition is positioned and orientated with respect to the electric field of the cavity mode. At exact resonance, with the QD positioned at the maximum of the cavity electric field and with its dipole orientated in the same direction as the field, this formula reduces to

$$F_P = \frac{3Q(\lambda/n)^3}{4\pi^2 V_0}. \quad (2.12)$$

For $F_P > 1$, the spontaneous emission rate is enhanced by the cavity and for $F_P < 1$, it is suppressed. The ratio of Q/V_0 for the cavity must be maximised to achieve large Purcell factors.

The fraction of the total emission from a QD that is emitted into the mode of a cavity is called the β -factor. The total emission rate will be the sum of the resonant and non-resonant emission rates. Assuming that the non-resonant

emission rate is not affected by the cavity, then the total emission rate will be $\gamma^{free} + \gamma^{cav}$, and it is easy to see that

$$\beta = \frac{\gamma^{cav}}{\gamma^{free} + \gamma^{cav}} = \frac{F_P}{1 + F_P}. \quad (2.13)$$

For large Purcell factors, the emission into the cavity dominates the non-resonant emission and the beta factor approaches unity.

2.3.3 Strong coupling

When the strength of the QD-cavity coupling dominates over the losses, the cavity and the QD transition are strongly coupled. In this regime, when a photon is emitted it is trapped in the cavity for long enough so that it can be reabsorbed by the QD. This reversible process, known as Rabi flopping, may occur many times before the photon is lost from the cavity irreversibly.

The Jaynes-Cummings model describes the QD-cavity interaction [5]. For an uncoupled system one would expect the two distinct states of one photon plus the unexcited QD, $|g, 1\rangle$, and the excited QD with no photon in the cavity, $|e, 0\rangle$, to be degenerate. However, for a strongly coupled system these states are mixed by the electric dipole interaction between the QD exciton and the photon, and the degeneracy is lifted. The new states look like $\frac{1}{\sqrt{2}}(|g, 1\rangle \pm |e, 0\rangle)$, and are split in energy by the vacuum Rabi splitting, given by

$$\Delta U^{\text{vac}} = 2\hbar \sqrt{g^2 - \frac{(\kappa - \gamma)^2}{16}}. \quad (2.14)$$

These states can be considered as quasi-particles resulting from mixing of the photon and the QD exciton and are known as the cavity polaritons [112, 142].

Transition from weak to strong coupling

For weak coupling, the second term in equation 2.14 dominates the square root, so that ΔU^{vac} is imaginary and there is no splitting. The linewidth of the exciton is broadened by the Purcell effect like $\gamma = F_P \gamma^{free}$. Close to strong coupling, the

linewidth of the exciton is broadened beyond this, and the linewidth of the cavity mode is reduced substantially below the uncoupled value.

In practice, the decay rate of the cavity is typically much bigger than that of the QD transition, $\kappa \gg \gamma$. For strong coupling, the first term in equation 2.14 is larger than the second term, i.e.

$$g > \kappa/4. \quad (2.15)$$

At this point the splitting becomes real and the linewidths of the two states collapse to become equal at roughly $(\kappa + \gamma)/2$. To resolve the vacuum Rabi splitting experimentally, these linewidths have to be narrower than the splitting.

By examining equations 2.3, 2.5 and 2.15, it is apparent that the ratio $Q/\sqrt{V_0}$ must be maximised to achieve strong coupling [112].

2.3.4 Types of cavities

A number of designs of cavities have been conceived of for integrating with semiconductor QDs. Each of them has its own advantages and disadvantages as will be discussed below.

Planar microcavities

A planar microcavity is formed by surrounding a cavity region by two distributed Bragg reflector (DBR) mirrors (see figure 2.4 (a)). Q -factors of up to 10000 have been achieved [118], however since the optical confinement exists only in one dimension, the mode volume is very large.

Micropillars

Micropillars are made by epitaxially growing a DBR cavity before etching the chip to form pillars (see figure 2.4 (b)). Light is confined in one direction by the DBR mirrors and in the other two directions by total internal reflection at the semiconductor-air interface.

The Q -factors of micropillars are limited by the smoothness of the side walls, which is limited by etching technologies. Furthermore, there is a trade-off between

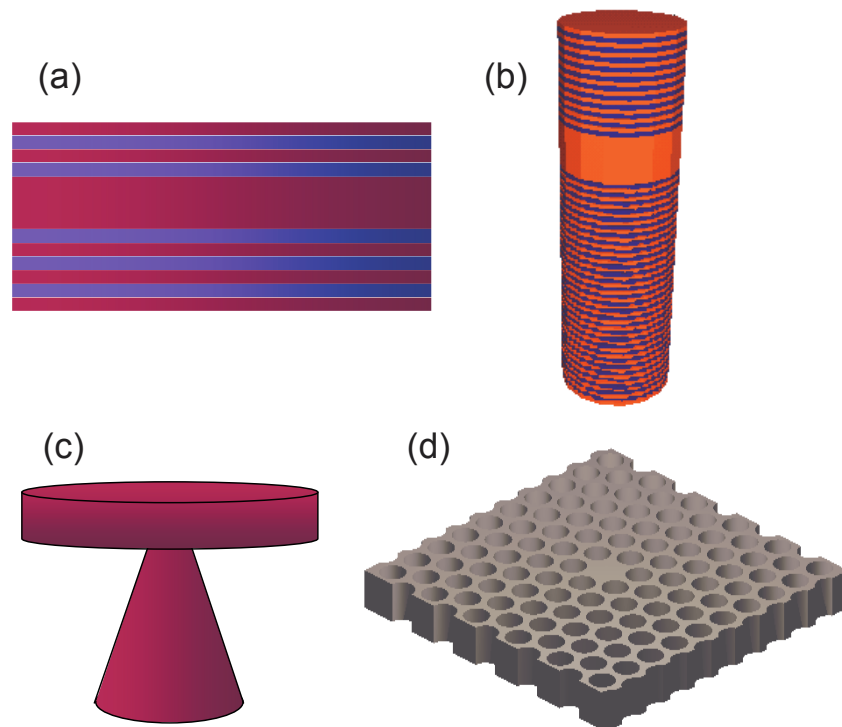


Figure 2.4: Schematic diagrams of (a) planar microcavity, (b) micropillar, (c) microdisk, (d) two-dimensional photonic crystal slab cavity.

Q -factor and the proportion of light emitted out-of-plane depending on the number of DBR periods in the top mirror [14]. Nevertheless, Q -factors of > 20000 [33, 118] have been demonstrated, with typical modal volumes of $\sim 5(\lambda/n)^3$ [135].

Microdisks

Another type of cavity is the microdisk. This consists of a flat, disk-shaped piece of high refractive index semiconductor suspended from the bulk crystal by a small tip (see figure 2.4 (c)). Whispering-gallery type modes can be confined by total internal reflection in the edges of the disk. These can have very high Q -factors over 100000 [126], with mode volumes of the order $\sim 6(\lambda/n)^3$ [135]. However, the emission is not as strongly directed as in the case of micropillars and complicated excitation/collection schemes are often required.

Photonic crystal cavities

Finally, photonic crystals can be used to make cavities as discussed in the following section (see figure 2.4 (d)). Three-dimensional photonic crystals offer the ideal prospect of strong confinement in all three dimensions, however they are limited by the difficulties of fabricating such complicated structures [101]. Two-dimensional photonic crystal slab cavities - in which light is confined in two-dimensions by a photonic band gap and in the third by total internal reflection at a semiconductor-air interface - have therefore received a lot of attention. They offer very high Q -factors along with tiny mode volumes ($\sim (\lambda/n)^3$), and are the cavity of choice for observing strong coupling [112].

Furthermore, the small mode volume of photonic crystal cavities make them preferable for applications in which a low Q -factor is required alongside a strong QD-cavity interaction. For example, by coupling both the exciton and biexciton to a cavity, the efficiency of entangled photon pair sources could be enhanced via the Purcell effect. Since the lines are typically a few meV apart, a low Q cavity is required. This leaves the mode volume as the only parameter available to increase the strength of the interaction. Alternatively, it may be possible to couple each transition to a separate mode of the same cavity since photonic crystal cavities usually support a number of modes [121] (see section 6.2).

2.4 Photonic crystals

This section will begin by discussing the origins of photonic band gaps. It will then go on to describe photonic crystal cavities and waveguides.

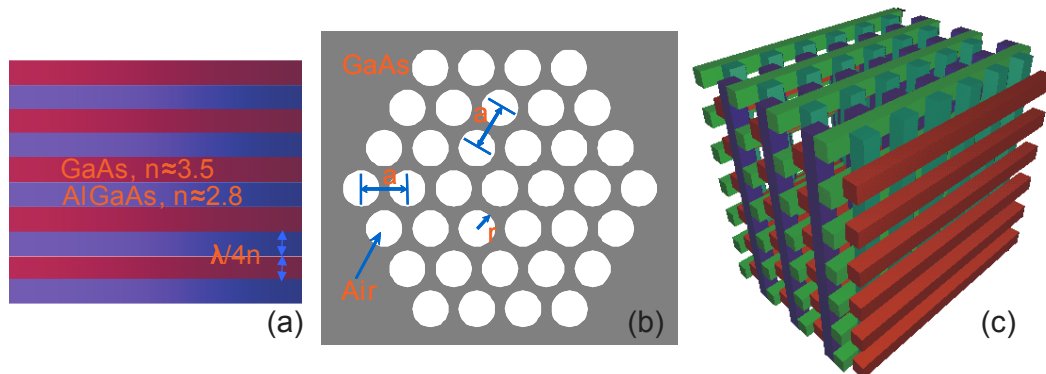


Figure 2.5: Schematic diagrams of examples of photonic crystals. (a) A distributed Bragg reflector (one-dimensional photonic crystal) is formed by alternate $\lambda/4n$ layers of two materials with a high refractive index contrast. (b) A two-dimensional photonic crystal consisting of a periodic array of air holes in a high-refractive index material. (c) A three-dimensional photonic crystal formed by a woodpile arrangement of high-refractive index bars.

A photonic crystal is a material with a periodic variation in its refractive index [60, 146]. For example, the well known Bragg mirror is a one-dimensional photonic crystal (see figure 2.5 (a)). Alternate $\lambda/4n$ thick layers of two materials with a large refractive index contrast give rise to Bragg reflection at the material interfaces which constructively interfere, so that any light with a wavelength close to λ is reflected.

A two-dimensional photonic crystal has a refractive index which varies periodically in two dimensions. An example of this is shown in figure 2.5 (b), in which a periodic array of holes is formed in a high refractive index material. In this case, Bragg reflection can occur along the two in-plane dimensions.

Finally, an example of a three-dimensional photonic crystal is illustrated in figure 2.5 (c). In this case, a three-dimensional periodic variation in the refractive

index is achieved by a so-called woodpile arrangement of high refractive index bars.

2.4.1 Photonic band gap

The periodicity in the refractive index of a photonic crystal causes Bragg reflections of photons which gives rise to forbidden energy bands at which photons cannot propagate through the crystal. This is analogous to the periodic potential in solid state physics which causes Bragg reflection of electrons and gives rise to electronic band gaps. Light with a frequency inside the band gap which is incident on a photonic crystal will decay exponentially inside the crystal and will be reflected. Appendix A examines the phenomena in more detail.

2.4.2 Photonic crystal cavities

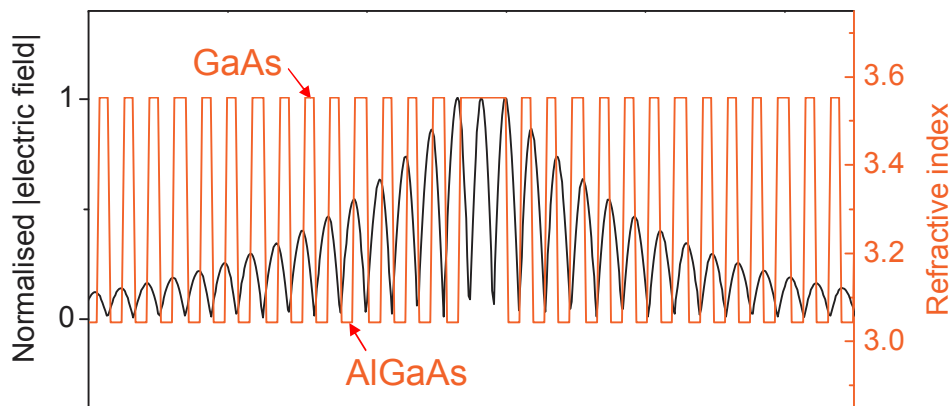


Figure 2.6: The electric field profile (black line) of a mode confined in a DBR cavity formed by a λ/n -thick layer of GaAs surrounded by DBR mirrors consisting of alternate $\lambda/4n$ -thick layers of GaAs and AlGaAs. The refractive index of the cavity is shown by the red line.

By introducing a defect into a photonic crystal, it is possible to create an optical cavity. For example, in the case of a DBR the thickness of one of the layers could be increased. The DBR surrounding the defect will act like a pair of

frequency selective mirrors. If the defect is thick enough, it will be possible for it to support a localised mode with a frequency inside the band gap. The mode will be confined in the direction parallel to the periodicity and will exponentially decay when it enters the photonic crystal. Figure 2.6 compares the normalised electric field of a mode confined in a DBR cavity to its refractive index distribution.

Because of the finite size of the confinement, defect modes are quantized into discrete frequencies. By increasing the thickness of the defect, more and more higher order modes can be supported.

2.4.3 Two-dimensional photonic crystals

A two-dimensional photonic crystal could be made, for example, by a triangular array of holes in a high refractive index material. In this case there is a periodic variation in the dielectric function in two dimensions, so a photonic band gap can exist in those two dimensions.

Because of the mirror symmetries, all the modes can be classified into one of two polarisations: transverse electric (TE) or transverse magnetic (TM) [59]. The former has non-zero field components (E_x, E_y, H_z) and the latter has (H_x, H_y, E_z) , where x and y are the two in-plane directions, and z is perpendicular to the periodic plane. The band structures for these two polarisations can be completely different. For example, a square lattice of rods only supports a band gap for the TM polarisation, whereas a triangular lattice of holes in a dielectric can support a complete band gap for both polarisations, as shown in figure 2.7.

A two-dimensional photonic crystal can be approximated in practice by a two-dimensional photonic crystal slab [36, 41]. This consists of a slab of high refractive index material perforated by an array of air holes. A cavity can be realised in this system by removing one (or more) of the holes [100, 105, 106]. For example, figure 2.8 shows a cavity formed by removing one of the air holes in a triangular lattice photonic crystal slab, the so-called H1 cavity. Light is confined by the photonic band gap in the two in-plane directions, and by total internal reflection (TIR) at the material/air interfaces in the out-of-plane direction. Other methods of producing a cavity include the double heterostructure concept [52, 75, 124, 131, 141].

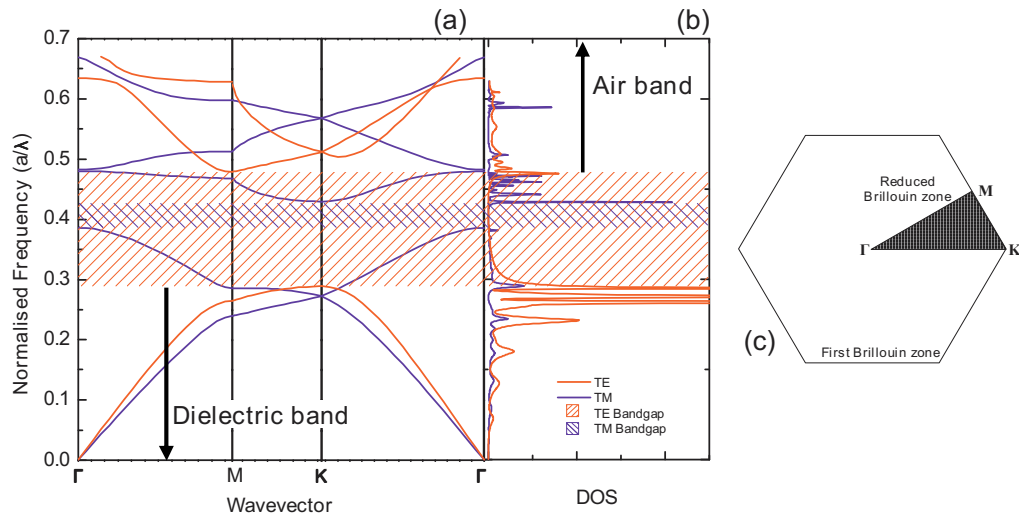


Figure 2.7: (a) Band structure of a two-dimensional photonic crystal with a triangular lattice of holes in a dielectric with normalised radius $r/a = 0.45$, calculated by a scattering matrix method. (b) Finite-difference time-domain calculation of the density of states for the same structure. Courtesy of D. Gevaux.

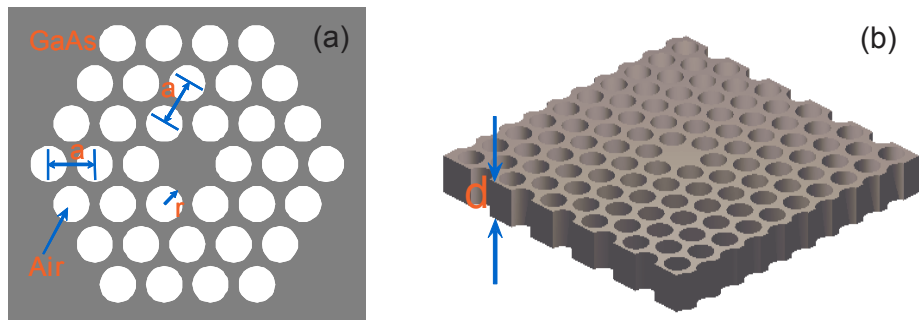


Figure 2.8: (a) Schematic diagram of a 2D photonic crystal nanocavity formed by removing one of the air holes in a triangular lattice of holes in a dielectric. (b) Three-dimensional view of an equivalent cavity formed in a 2D photonic crystal slab.

Figure 2.9 shows the calculated spectrum for an unmodified H1 cavity with normalised radius of holes $r/a = 0.3$ and normalised slab height $d/a = 0.7$. There is a photonic band gap stretching from $\lambda/a \sim 3.2$ to $\lambda/a \sim 4.2$, with a single resonant mode confined inside it. The field distributions of the TE-like mode are shown, which is known as the dipole mode because of the two anti-nodes in its magnetic field distribution.

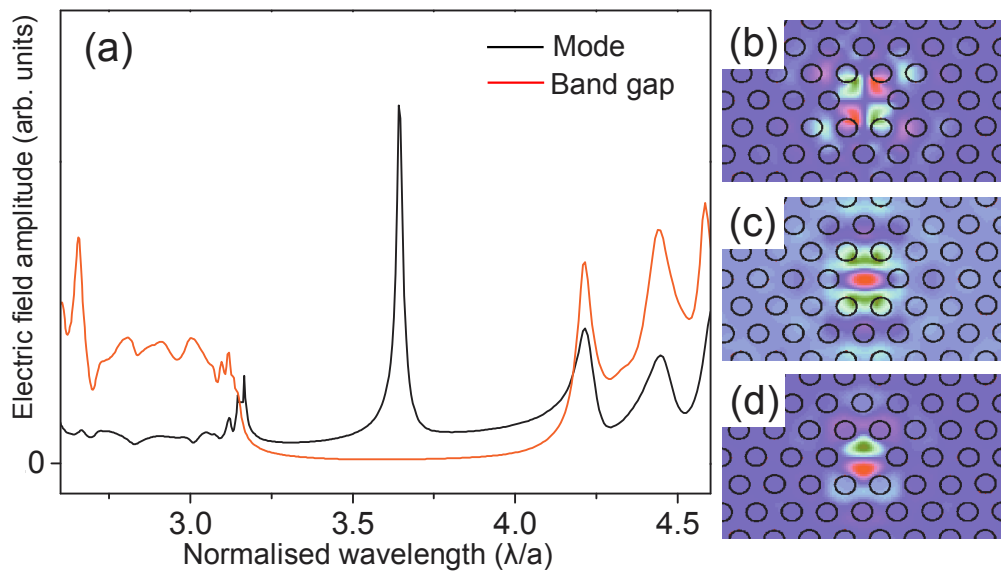


Figure 2.9: (a) Spectrum for an unmodified H1 cavity with $r = 0.3a$, $d = 0.7a$ and $n = 3.53$, calculated by finite-difference time-domain simulation. The black line shows the spectrum inside the defect. The red line shows a similar calculation with no defect, so that the extent of the photonic band gap is made clear. A mode is present near the centre of the band gap, which is called the dipole mode because of the two anti-nodes in its magnetic field distribution. (b)-(d) E_x , E_y and H_z field distributions of the dipole mode.

Not all of the components of a mode confined inside the cavity will be totally internally reflected, and there will be losses in the vertical direction [59]. In the air, far away from the structure, light obeys

$$\omega = c|\mathbf{k}| = c\sqrt{|\mathbf{k}_{//}|^2 + k_z^2}, \quad (2.16)$$

where $\mathbf{k}_{//}$ is the wave vector in the direction of the photonic crystal plane, and k_z is the wave vector in the out-of-plane direction. Close to the structure, a continuum of extended states propagating in the air exists for $\omega > c|\mathbf{k}_{//}|$, since k_z is not restricted by the photonic crystal. Therefore, components of the mode with in-plane wave vector inside the so called light line, $|\mathbf{k}_{//}| < \omega_{cav}/c$, are not confined to the photonic crystal slab and can be easily lost from the cavity. The photonic crystal slab can support components with larger wave vectors than the air since its dispersion relation approximately looks like $|\mathbf{k}| = n\omega/c$. Any components of the mode outside the light line, $|\mathbf{k}_{//}| > \omega_{cav}/c$, cannot couple to air modes and are strongly confined.

There is an intrinsic vertical radiative loss associated with any confined mode, since some of its components can couple to light line modes at the same frequency. Figure 2.10 illustrates this point. These losses can be minimised and the Q -factor maximised by carefully designing the cavity so that the coupling to the light line is minimised [2, 3, 124, 127, 137].

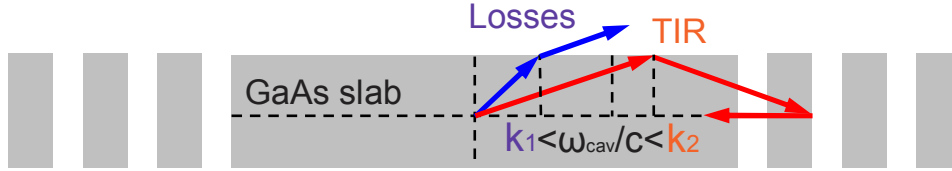


Figure 2.10: Schematic diagram of losses inside the light line. Momentum components of the mode with $|\mathbf{k}_{//}| < \omega_{cav}/c$ are lost from the GaAs slab (k_1), whereas components with $|\mathbf{k}_{//}| > \omega_{cav}/c$ are totally internally reflected (k_2).

2.4.4 Practical considerations

As described in section 2.3, coupling a QD transition to a high- Q , low volume mode of an optical cavity enhances the spontaneous emission rate of the transition. By carefully designing the properties of a defect and the surrounding photonic crystal, it is possible to reduce intrinsic losses and to make very high- Q cavities. Furthermore, the mode volumes of photonic crystal cavities are tiny,

typically of order $(\lambda/n)^3$. In real life cavities, there are also losses due to fabrication imperfections and light scattering in the crystal [44]. The structures must therefore be well fabricated so that there is little unwanted scattering at the surfaces.

The equation for the Purcell factor (equation 2.10) includes a spectral overlap term. This can be maximised by carefully designing the cavity so that the mode appears at the correct frequency. Appendix A sets out the similarities between electrodynamics and quantum mechanics with respect to the formation of band gaps and defect modes, etc. However one major difference between these two theories is the scaling properties. The quantum mechanical Hamiltonian includes the constant $\hbar^2/2m$, which is related to a fundamental length, the Bohr radius $\hbar/mc\alpha$. Hence, quantum mechanical systems do not scale in size. However, the Maxwell equations do not contain any reference to a fundamental length scale, so they do scale. The solutions to a system which differs from another system only by an overall scaling factor are simply related by the same scaling factor. Hence it is straight forward to scale the size of a cavity so that a mode appears at a particular desired frequency.

Equation 2.10 also includes a spatial overlap term, ξ^2 . This says that there must be a strong overlap of the QD's dipole and the electric field of the mode for a strong interaction, i.e. the QD should ideally be located at the maximum of the electric field of the mode. This requirement is currently very challenging since the self-assembled InAs QDs used in this work form in random positions when they are grown.

Chapter 3

Experimental techniques

3.1 Overview

This chapter will begin by explaining the growth of the wafers used in this work. It will then go on to discuss the optical techniques used to study the samples.

3.2 Sample growth and basic preparation

3.2.1 Quantum dot growth

All of the samples used in this work were grown by solid source molecular beam epitaxy (MBE) at the Cavendish Laboratory. MBE is a mature technique which allows precise growth of high purity material with monolayer precision [51]. In this work, InAs quantum dots were grown by the Stranski-Krastanov growth method. Since InAs and GaAs have slightly different lattice constants ($\sim 7.5\%$ different), when InAs is grown on GaAs, there is a strain in the structure. Initially, a strained layer of InAs is formed; as more material is deposited, a critical thickness (between 1.6 and 2.0 monolayers, depending on the exact growth conditions) is reached, at which the strain is relaxed by the formation of small islands of InAs - quantum dots. A thin layer of InAs remains below the QDs, as depicted in figure 3.1 (a), called the wetting layer. As even more material is deposited, the QDs grow larger until they begin to coalesce together. The samples used in this work consist of a thin layer of InAs, close to the critical thickness, such that

3.2 Sample growth and basic preparation

a low density of QDs are formed. The QDs are completed by growing over with more GaAs. Figure 3.1 (b) shows an AFM image of an uncapped low density layer of QDs.

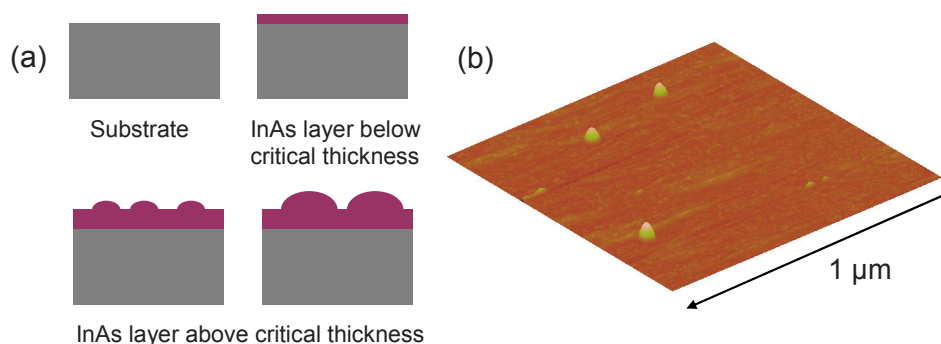


Figure 3.1: (a) Schematic diagram of QD growth by the Stranski-Krastanov growth method. (b) AFM image of uncapped QDs.

Due to the self-assembled nature of Stranski-Krastanov grown dots, their size and shape vary widely and their positions are random. It is, however, possible to reproducibly grow wafers with similar distributions of sizes and shapes. A feature of the MBE system used in this work is that a combination of the indium cell shape and position causes the deposition to be nonuniform across the wafer. A larger amount of indium is deposited at the centre of the wafer as compared to the edge. The growth is typically tailored so that the dot density varies from a high density in the centre to zero at the edge, so that the ideal low density of dots forms somewhere in the middle.

3.2.2 Isolating single quantum dots

The density of the randomly positioned QDs typically varies between zero and a few hundred per square micron, whilst the spot of the exciting laser typically has an area of around $2 \mu\text{m}^2$. Therefore, a method to isolate and relocate single quantum dots is required. A common technique used in parts of this work is simply to evaporate a shadow mask (e.g. of aluminium) perforated with an array of small holes. The holes allow optical access to a small portion of the wafer.

When a QD happens to lie beneath one of these holes, it is easy to relocate it. Holes with area of the order $1 \mu\text{m}^2$ were typically used. In other aspects of this work, the fabrication of small optical cavities was sufficient to isolate single dots.

3.3 Optical techniques

This section will detail the experimental techniques used to study the samples.

3.3.1 Micro-photoluminescence spectroscopy

Normal incidence setup

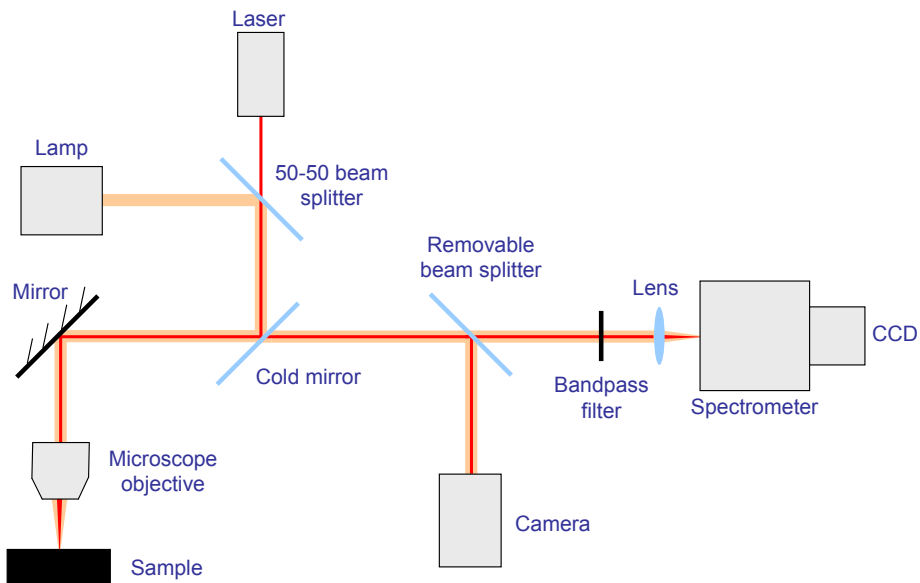


Figure 3.2: Schematic diagram of the experimental setup for micro-photoluminescence spectroscopy

Normal incidence micro-photoluminescence (μPL) spectroscopy was the main tool used to study the samples. The basic setup is shown in figure 3.2. A laser is focused to a spot with area $\sim 2 \mu\text{m}^2$ by an infinity corrected $\times 100$ microscope objective lens with a numerical aperture of 0.5, and is used to excite the sample.

The laser used for the bulk of this work was a mode-locked Spectra-Physics pulsed picosecond Ti-Sapphire laser, pumped with a 532 nm continuous wave (CW) diode-pumped Nd:YVO₄ laser. This system operates with a repetition rate of 80 MHz, with pulse widths of around 3 ps. The emission wavelength was tuneable between ~ 750 nm and ~ 1000 nm, and was set at ~ 780 nm for all measurements except where otherwise stated. At this wavelength, corresponding to an energy above the GaAs band gap, carriers are excited in the GaAs before some of them relax into the InAs QDs. The power of the laser excitation was controlled with a set of variable neutral density (ND) filters.

Photoluminescence (PL) emitted by the sample was collected by the same objective before being dispersed by a Jobin Yvon HR460 grating spectrometer (resolution ~ 50 μ eV) and detected by a nitrogen-cooled charge-coupled-device (CCD) camera. The objective was mounted on an XYZ translation stage which allowed positioning and focusing of the laser spot. A white light lamp could be turned on and a removable beam-splitter inserted into the setup to enable imaging of the sample and alignment using a video camera.

A cold mirror was used which reflects/transmits shorter/longer wavelength light such that most of the laser (~ 780 nm) and white light was reflected and the majority of the sample PL (~ 900 nm) was transmitted towards the spectrometer. This ensured that as much as possible of the PL and as little as possible of the laser light was detected. A bandpass filter was placed in front of the spectrometer to eliminate any remaining laser light reflected from the sample.

The sample itself was mounted inside a continuous flow helium cryostat which could be cooled down to around the boiling point of helium (4.2 K). An electrical heater inside the cryostat allowed the temperature of the sample to be set anywhere between this and room temperature.

A removable half-wave plate (HWP) and a polariser could be placed between the cold mirror and the spectrometer to allow polarisation resolved PL.

Lateral setup

A micro-photoluminescence was designed and implemented to allow PL collection lateral to the sample growth direction, specifically for samples studied in this

work. The setup is shown schematically in figure 3.3. The sample was placed inside a specially modified cryostat with a window allowing both normal incidence and lateral optical access. A laser was focused to a spot on the sample surface by a $\times 100$ microscope objective lens as before. The PL emitted from the side of the sample was collected by a second $\times 50$ objective lens before being detected in the same way as above. A second removable beam-splitter and video camera were used to align the second objective.

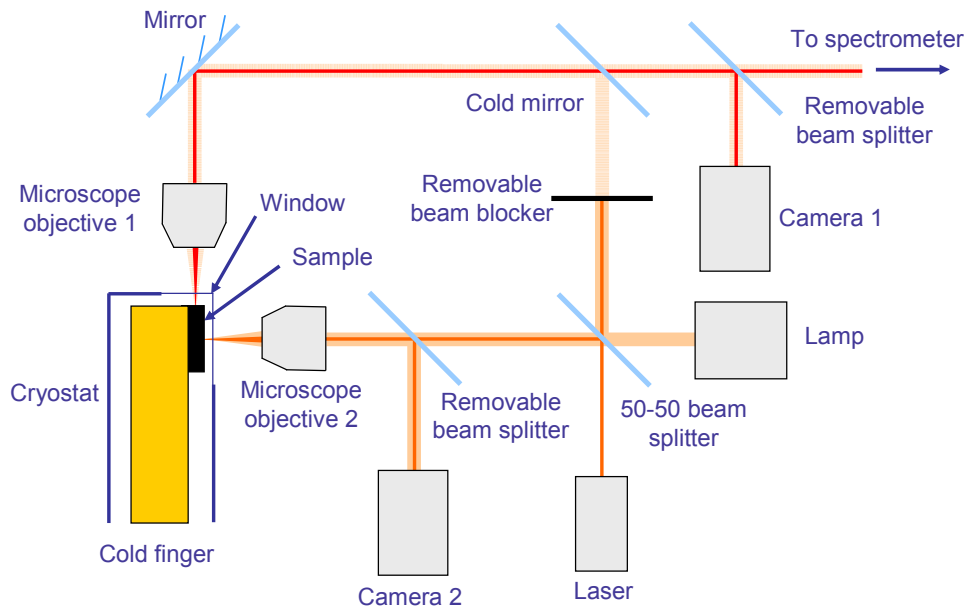


Figure 3.3: Schematic diagram of the experimental setup for lateral micro-photoluminescence spectroscopy

3.3.2 Time-resolved photoluminescence

Figure 3.4 shows the setup for time-resolved PL (TRPL). The emission from the sample was focused into the spectrometer in the same way as in figure 3.2. However, the dispersed light was then directed to a second output port of the spectrometer via a slit which acted as a spectral filter. This light was then focused

onto a silicon avalanche photodiode (APD) which generates electrical pulses when single photons are detected. The APD was 40% efficient at 900 nm. The pulses from the APD and a reference signal from the laser's clock were sent to a Becker & Hickl GmbH SPC-630 single photon counting module (SPCM). The SPCM measures the time difference between the two pulses and builds up a histogram of the photon arrival times with respect to the laser pulse. The decay time of emission lines can be calculated from this histogram.

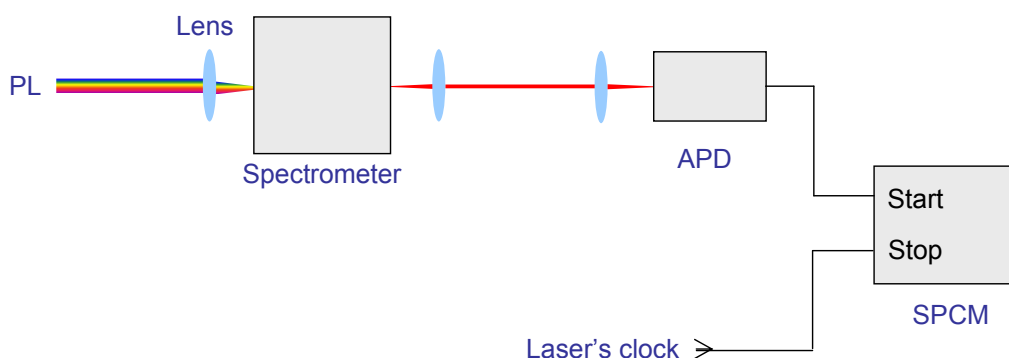


Figure 3.4: Schematic diagram of the experimental setup for time-resolved photoluminescence spectroscopy

3.3.3 Auto-correlations

Auto-correlation measurements were performed using a Hanbury-Brown and Twiss set-up as illustrated in figure 3.5. An emission line was spectrally selected by the spectrometer and was directed towards a non-polarising 50:50 beam splitter. Two separate APDs detect the photons from each of the beam splitter's outputs. One of the APDs provides the 'start' pulse to the SPCM and the other provides the 'stop' pulse and a histogram of the time difference, τ , between the events is built up over time. This histogram approximates to the second order correlation function, $g^2(\tau)$, when τ is much smaller than the mean time between detection events.

The second-order correlation function of the emission can be used to quantify the quality of a single photon source:

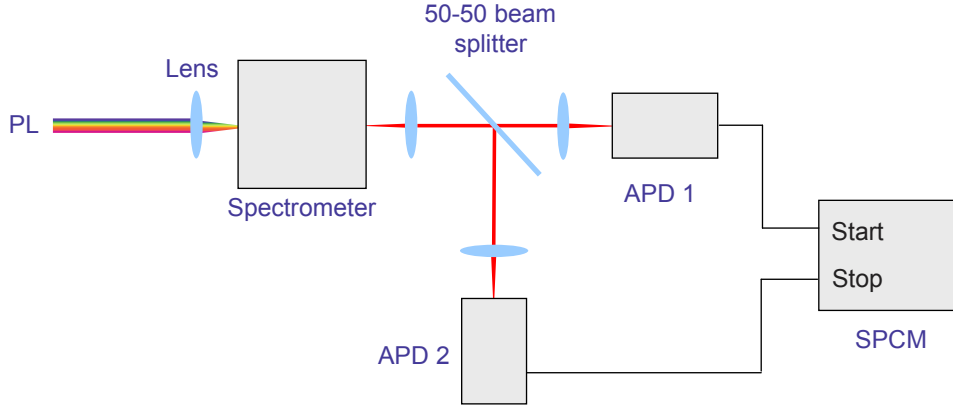


Figure 3.5: Schematic diagram of the experimental setup for auto-correlation measurements

$$g^{(2)}(\tau) = \frac{\langle I(t)I(t + \tau) \rangle}{\langle I(t) \rangle \langle I(t + \tau) \rangle}, \quad (3.1)$$

where $I(t)$ is the intensity of the light at time t , and $\langle I(t) \rangle$ is the time-averaged intensity over a long period of time. It is a measure of the correlations between the intensities of the light beam at different times, t and $t + \tau$.

For a coherent continuous wave (CW) source obeying Poissonian statistics, the probability of a photon being emitted at time τ after a first photon is equally likely for all times, so $g^{(2)}(\tau) \approx 1$ for all τ . In the case that the source is operated in pulsed mode, $g^{(2)}(\tau)$ will be modulated by the pulses into a series of peaks whose areas have a Poissonian variation about unity.

In the case of a thermal source, the characteristic intensity fluctuations or bunches of photons give rise to correlations at small values of τ , so that $g^{(2)}(\tau = 0) > 1$.

For the opposite case of an anti-bunched photon source, $g^{(2)}(0) < 1$. For a true single photon source, only one photon is emitted at a time, so the intensity correlations at $\tau = 0$ fall to zero, i.e. $g^{(2)}(0) = 0$. In the pulsed scenario, this is manifest as the absence of a peak at $\tau = 0$. In practice, the measured $g^{(2)}(0)$ will

not be exactly zero even for a perfect single photon source due to dark counts in the APDs and the finite time response of the system.

3.3.4 Cross-correlations

Correlations between different excitonic lines were measured using the setup in figure 3.6. A non-polarising 50-50 beam splitter was placed directly after the cold mirror and the outputs were focused onto two separate spectrometers. Each spectrometer spectrally selected a different emission line in the PL. The light selected by the first spectrometer (S1) was resolved into its two rectilinear polarized components (H and V) by a polarising beam-splitter before being detected by two APDs, APD1 and APD2. The light selected by the second spectrometer (S2) was detected by APD3. The signals from the APDs were used as the start and stop pulses for two SPCMs.

In this way, the correlation function between the light selected by spectrometer S2 and the H or V component of the light selected by spectrometer S1 could be measured. A histogram of the time delay between photons arriving at APD1/2 and APD 3 was built up. The form of the histogram is approximately equivalent to the correlation function between the two lines.

3.3.5 Application of a magnetic field

A magnetic field was used in some aspects of this work. To apply the field to a sample, a cryostat with a cold finger extending into the bore of a superconducting magnet was used. The magnet had a range of up to 5 T. At the centre of the bore, the magnetic field was parallel to the axis of the bore. The samples could be mounted on top of the cold finger with the field parallel to the growth direction of the QDs - the Faraday geometry (figure 3.7 (a)) - or a copper mount and a prism could be used to achieve the Voigt geometry (figure 3.7 (b)), with the field in the plane of the dots.

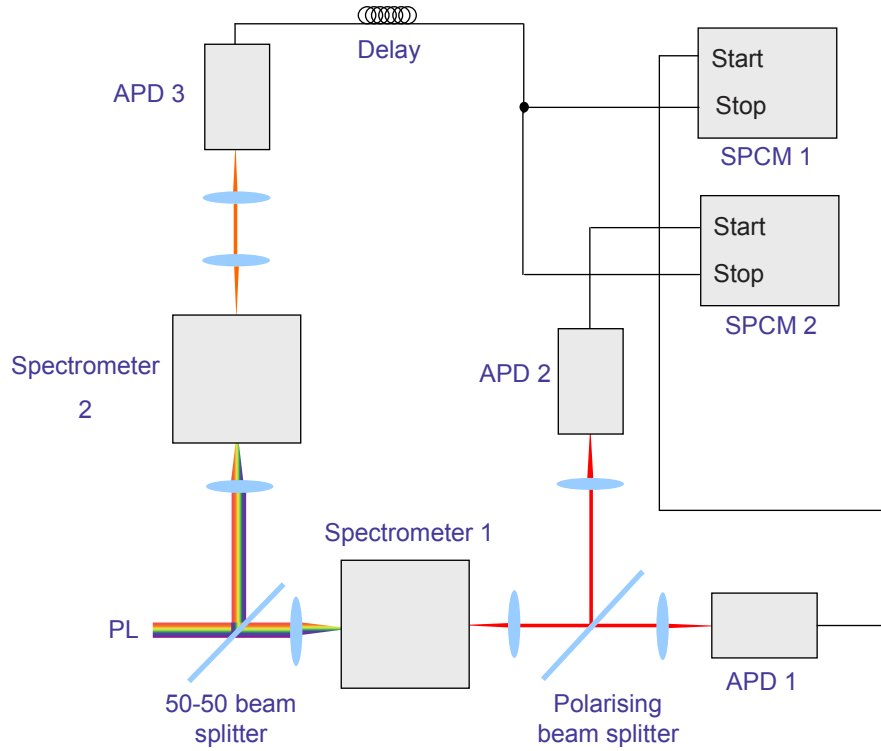


Figure 3.6: Schematic diagram of the experimental setup for cross-correlation measurements

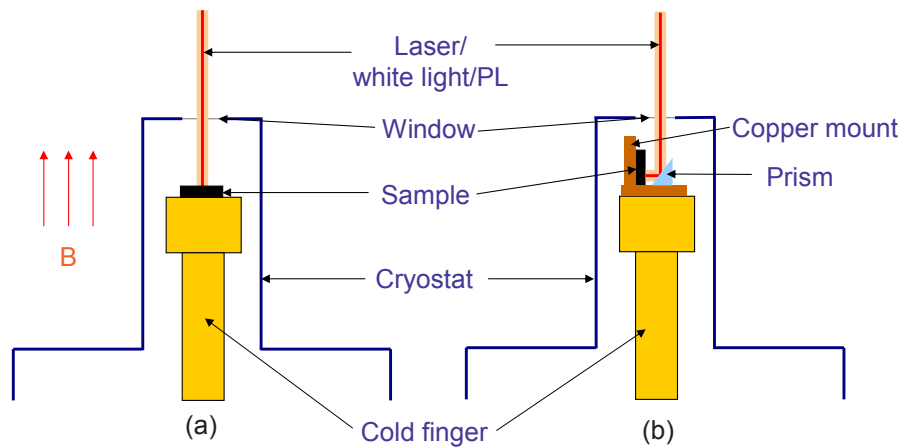


Figure 3.7: Schematic diagram of the experimental setup used for applying a magnetic field in (a) the Faraday geometry, and (b) the Voigt geometry.

3.4 Spectroscopy of quantum dots

A typical spectrum of the emission from a large number of quantum dots is shown in figure 3.8. An emission peak at around 830 nm is associated with excitons bound to impurities in GaAs [1]. Another peak at around 870 nm is due to emission from the wetting layer, which behaves like a quantum well [19]. Finally, the sharp features at longer wavelengths are a result of emission from quantum dots. Figure 2.2 shows PL from a single QD isolated underneath a hole in an aluminium mask. Four lines from different excitonic states are present, as labeled. There are a number of spectroscopic methods used to give information about individual excitonic lines, which will be detailed in the following subsections.

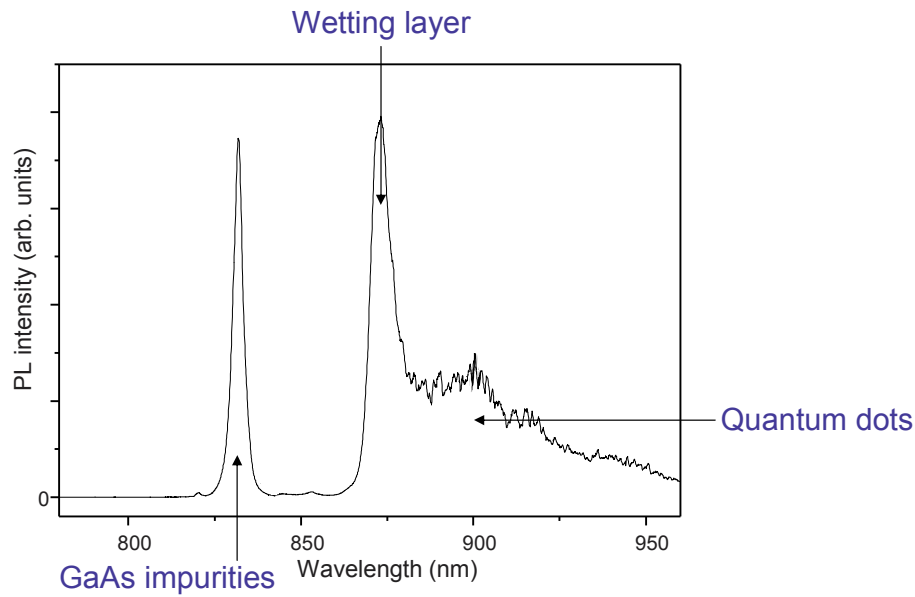


Figure 3.8: Typical spectrum of the emission from a large number of InAs quantum dots.

3.4.1 Power dependence

Measuring the relationship between laser pump power and the integrated intensity of a QD emission line can give information about which excitonic state the

line originates from. Each photon absorbed by the semiconductor will excite one electron from the valence band into the conduction band, leaving a hole behind. Therefore, one would expect the intensity of the exciton line, which results from the recombination of one electron and one hole, to vary linearly with laser power. The biexciton line, resulting from two electrons and two holes, should vary quadratically.

When exciting with a CW laser at high enough power, repopulation of the biexciton state from the exciton state will become favourable over the decay of the exciton to the ground state. Therefore the biexciton will dominate the spectrum at high powers. When exciting with a pulsed laser whose pulses are much shorter than the lifetime of the excitonic states, and whose repetition period is much longer than the state lifetimes, it is likely that the exciton will always decay following the biexciton decay. In this case, the exciton and biexciton lines will saturate at high laser powers at roughly the same intensity (as in figure 3.9).

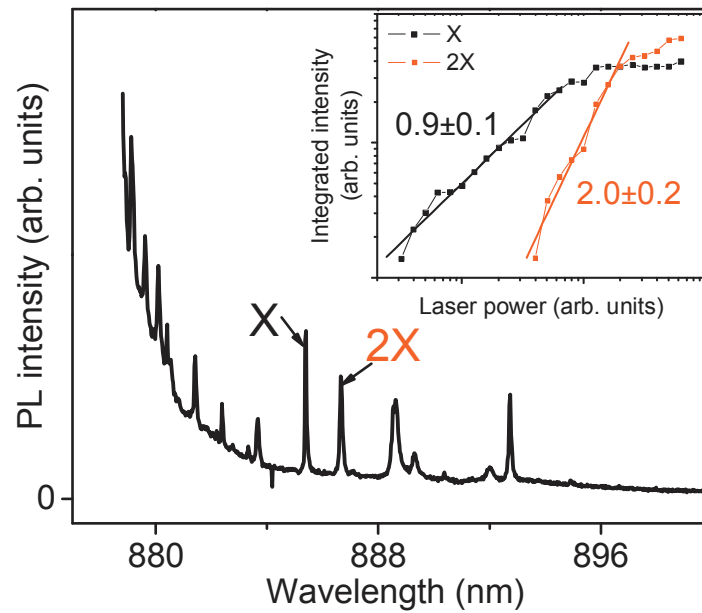


Figure 3.9: Identification of an exciton and a biexciton by power dependence under pulsed excitation.

3.4.2 Polarization of excitons

As described in section 2.2.3, the exciton state is usually split in energy, resulting in a polarisation splitting in the PL from the exciton and the biexciton. This splitting can be observed experimentally and can be used to distinguish between the neutral excitons and the singly charged excitons, which exhibit no polarisation splitting.

Chapter 4

p-i-n diode quantum dot devices

4.1 Overview

To date, a variety of devices using quantum dots have been developed. These include single photon sources [15, 29, 34, 80, 93, 117, 151] and detectors [13, 21], sources of polarisation-entangled photon pairs [4, 17, 130, 150] and quantum dot lasers [20, 105, 148]. This chapter details experiments carried out with a single quantum dot embedded in the intrinsic region of a *p-i-n* diode. The chapter begins with a description of the device and goes on to describe experiments showing its use to maximise the polarisation correlation of the biexciton decay, and as a memory device.

4.2 Sample design and operation

The samples used in this study were grown by MBE, consisting of a GaAs λ/n -thick planar optical cavity [14], centred at ~ 900 nm, containing a layer of InAs QDs at the centre and 5 nm above an AlAs/GaAs superlattice. The cavity was produced by growing twelve repeats of GaAs/AlAs DBR mirrors below the cavity and two repeats above it. The top mirror was *p*-doped with carbon and the top two repeats of the bottom mirror were *n*-doped with silicon, to create a *p-i-n* diode. The superlattice, which prohibits electrons from tunneling out of the QDs, was formed by seven repeats of 2 nm-thick layers of $\text{Al}_{0.98}\text{Ga}_{0.02}\text{As}$ and

4.2 Sample design and operation

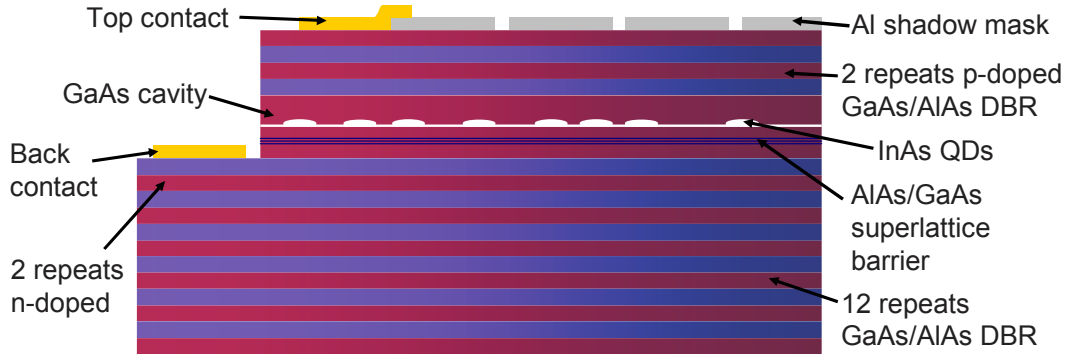


Figure 4.1: Schematic diagram of the *p-i-n* diode quantum dot device structure in profile.

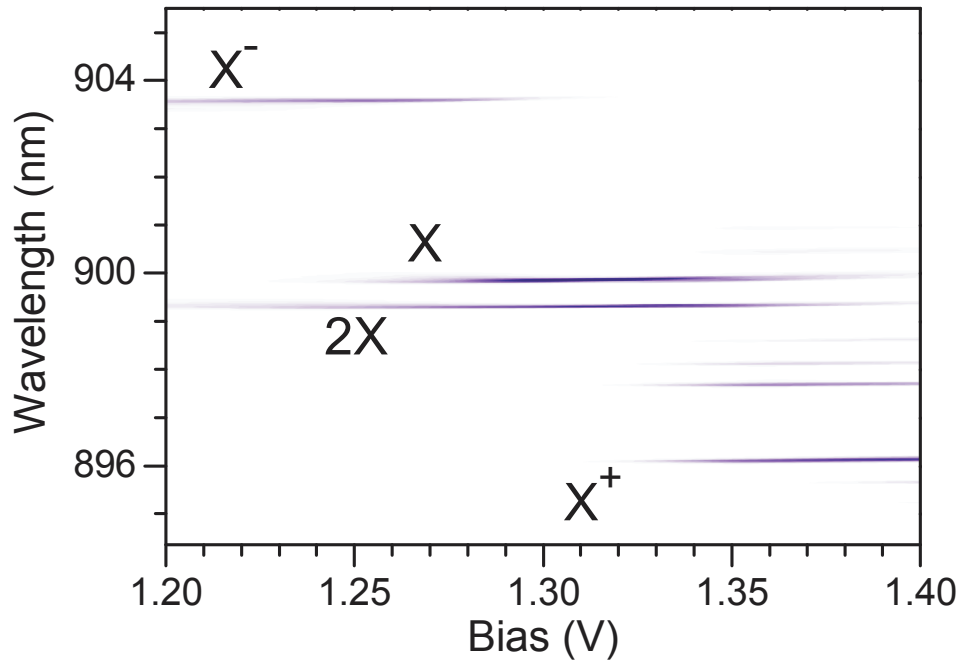


Figure 4.2: Plot showing the evolution of the spectrum from a QD in the device as the forward bias applied across the diode is swept. Blue indicates high PL intensity, white indicates low intensity. The neutral exciton (X), biexciton ($2X$) and charged excitons (X^+ , X^-), identified by power dependence and observations of the fine structure, are labeled. The other weak lines in the spectra are most likely from more highly positively charged states.

4.2 Sample design and operation

$\text{Al}_{0.5}\text{Ga}_{0.5}\text{As}$. Figure 4.1 shows a schematic diagram of the sample design.

An aluminium shadow mask of $\sim 2 \mu\text{m}$ diameter circular apertures was evaporated onto the surface of the device to allow optical access to individual QDs. Pits were etched down to the n -doped region so that titanium and gold could be evaporated to electrically contact the region. More titanium and gold was evaporated to contact the p -doped region via the shadow mask. The contacts allowed an electric field to be applied across the QDs in the cavity.

Figure 4.2 shows PL from a single QD in the device as a function of the bias applied across the diode. The device was operated in forward bias and no electroluminescence was observed in the range of biases used in this study. A number of lines are present in the spectra, originating from different excitonic states [48, 77], as labeled. The existence of emission from different states is a result of the random trapping of electrons and holes by the QD before radiative decay. By changing the bias across the device, the dominant excitonic states present in the spectrum can be changed. This is due to the changing hole tunneling rate from the dot, as the bias is varied, illustrated in figure 4.3.

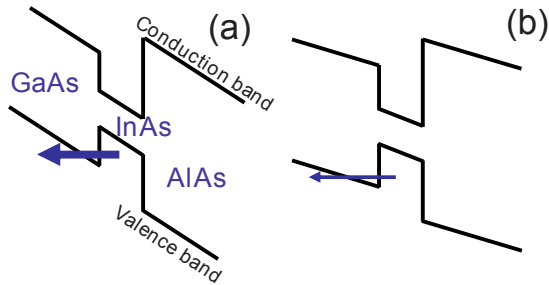


Figure 4.3: Simplified diagrams of the band structure of the device with a low applied forward bias (a) and a higher applied bias (b). The electron tunneling barrier, grown 5 nm underneath the QD layer, is shown by a higher potential barrier to the right of the InAs QD. The blue arrows represent the hole tunneling rates.

4.3 Controlling the polarisation correlation of photon pairs

The intensities of the emission lines in figure 4.2 were integrated and plotted as a function of bias in figure 4.4. Below ~ 1 V, no PL was measured from the QD, indicating that the rate at which the holes tunnel from the dot is much greater than the radiative decay rate of any of the QD optical transitions. For a bias of 1-1.25 V, emission from the neutral exciton (X) is very dim since the hole tunneling rate is faster than its radiative decay rate. The biexciton (2X) is brighter since its radiative decay rate is faster than that of X. The negatively charged exciton (X^-) is dominant in the spectrum since the most likely decay path from 2X is for a hole to tunnel out, forming X^- . If the second hole tunnels out before the radiative decay of X^- , no emission will be seen.

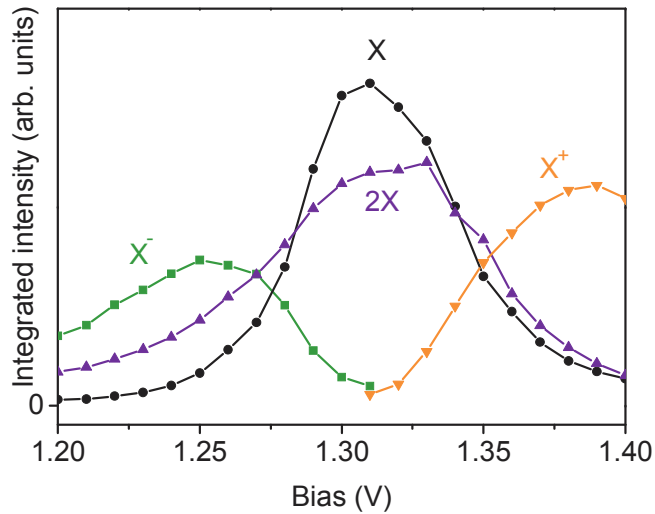


Figure 4.4: Integrated intensities of the emission lines in figure 4.2 as a function of bias applied across the diode.

As the bias is increased, the hole tunneling rate is decreased below the radiative decay rates of X and 2X, so that they become dominant in the spectrum. At higher biases, the positively charged exciton (X^+) is dominant since holes may drift into the dot from the p region, while electrons may not drift in from the n

4.3 Controlling the polarisation correlation of photon pairs

region due to the tunneling barrier. There are also some other weak lines present, most likely resulting from more highly positively charged states.

Figure 4.2 shows that it is possible to control the particular excitonic states which are present in the emission from a QD with this device [39, 140]. This property could be exploited, for example, by tuning out the unwanted lines from the QD emission for a given application. The associated increase in the intensity of the desired line(s) and reduction in background light would benefit many QD applications such as the generation of triggered photon pairs by the biexciton decay [130].

4.3.1 Degree of polarisation correlation

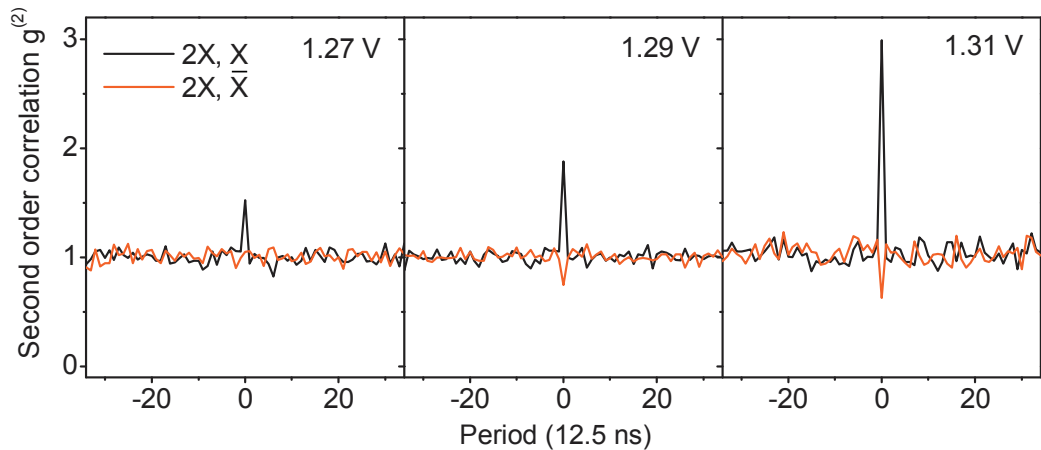


Figure 4.5: Second order correlation of the H polarised biexciton photon with the H exciton photon (black) and the V exciton photon (red) at different biases. The period of the laser is 12.5 ns.

This particular QD has a considerable fine structure splitting [43] ($S_0 > 20\mu\text{eV}$). Hence the exciton and biexciton photons are expected to have identical rectilinear polarisation of H or V [115, 129, 134] (see figure 2.3). Cross-correlation measurements were carried out to study the degree of rectilinear polarisation correlation, C , between the biexciton and exciton photons as the bias was varied.

4.3 Controlling the polarisation correlation of photon pairs

The second order correlation of the H polarised biexciton photon with H exciton photons and with V exciton photons were simultaneously measured using the setup described in section 3.3.4. Figure 4.5 shows results for three different biases. It is clear that the co-polarised photons are correlated and the oppositely polarised photons are anti-correlated at zero delay, to varying degrees. This implies that the emission of a H polarised exciton photon is much more likely than the emission of a V polarised photon following the emission of a H polarised biexciton photon, as expected.

The results were used to calculate the degree of rectilinear polarisation correlation, C , using

$$C = \frac{g_{2X,X}^{(2)} - g_{2X,\bar{X}}^{(2)}}{g_{2X,X}^{(2)} + g_{2X,\bar{X}}^{(2)}}, \quad (4.1)$$

where $g_{2X,X}^{(2)}$ is the second order correlation function at zero delay between the H biexciton photons and the H component of the exciton emission, and $g_{2X,\bar{X}}^{(2)}$ is the correlation between the H -polarised biexciton photons and the V -polarised exciton photons. The second order correlation function is given by equation 3.1. C is therefore expected to be 100% for an ideal QD emitting polarisation correlated photons in the rectilinear basis, and 0% for an uncorrelated source.

The red data in figure 4.6 shows the measured C as a function of applied bias. The error is the smallest when the exciton and biexciton emission are at their strongest, and increases as they fade away. This is as expected because when the count rate is small there is a large error. It can be seen that for high biases, C is high as predicted, e.g. $68 \pm 6\%$ at 1.33 V. However at low biases, it tails off unexpectedly, to $13 \pm 5\%$ at 1.25 V.

Previous studies of nominally uncharged QDs have shown that the degree of correlation can be limited by background light due to emission from other layers of the device, and by exciton spin scattering effects [150]. The former is clearly not the dominant effect since it would be minimal when the emission is at its maximum at ~ 1.31 V. However C increases from $56 \pm 4\%$ at 1.31 V to $68 \pm 6\%$ at 1.33 V. This suggests that the sharp drop in C at low biases is due to exciton spin scattering.

4.3 Controlling the polarisation correlation of photon pairs

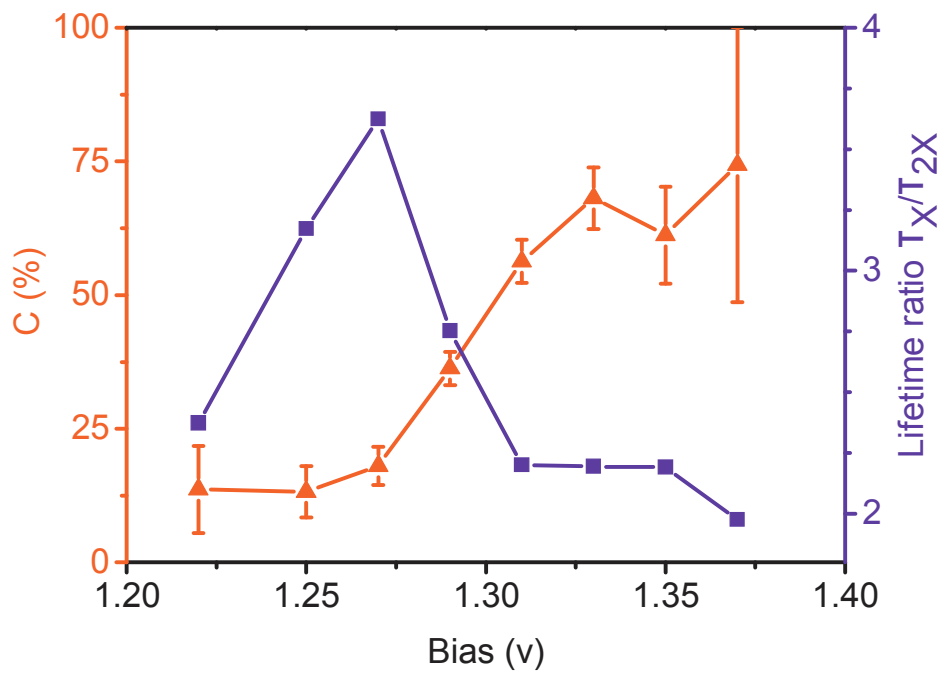


Figure 4.6: The ratio of the biexciton and exciton states' lifetimes (blue) and the degree of rectilinear polarisation correlation, C , between the biexciton and exciton photons (red). Error bars span two standard deviations of the random error. Where not shown, the random error is smaller than the symbol size.

4.3.2 Lifetime measurements

Further evidence that spin scattering is responsible for the drop in C is provided by lifetime measurements of the exciton and biexciton which were taken at the same time as the correlation measurements. The ratio between the exciton and biexciton lifetimes was calculated for each bias and is plotted as the blue line in figure 4.6.

The ratio between the lifetimes is expected to be ~ 2 for slow exciton dephasing [99, 143] which is the typical result for InAs QDs. This result can be approximately understood by considering the fact that the biexciton has two different decay paths (the $m = \pm 1$ excitons), whereas the exciton only has one. It is therefore expected that the radiative lifetime of the biexciton will be around half that of the exciton. The measured value is close to 2 at high biases. However at lower biases, as the degree of correlation drops off, the ratio increases and peaks at 3.62 ± 0.02 . The increase is due mainly to an increase in the lifetime of the exciton. The spectral lines shift in energy by a very small amount over this range of biases and therefore changes in the lifetimes due to the quantum confined Stark effect are expected to be insignificant.

In the case of a fast spin flip rate, theoretical studies have predicted a value of ~ 4 for the lifetime ratio [99]. If the spin of a carrier in an exciton is flipped, a dark exciton is formed which has a very long lifetime. For a fast spin flip rate, the exciton spends half of its time in the dark state. This would have the effect of doubling the exciton lifetime and would also explain the drop in C . The lifetime ratio drops off at lower biases as the hole tunneling time becomes comparable to the exciton's radiative lifetime.

4.3.3 Polarisation correlation control

This device allows control over which excitonic state is dominant in the spectrum from a QD. When light from the charged states is minimised, the emission from the neutral states is maximised as expected. For low biases the degree of polarisation correlation between the biexciton and exciton photons is limited by spin scattering.

At low biases, there will be an excess of electrons in the vicinity of the dot which can cause the exciton's electron spin to be flipped. Excess electrons may be confined at the heterojunction at the tunneling barrier. The polarisation correlation does not drop off at biases where an excess of holes would be expected, since there is no hole tunneling barrier to trap holes.

It is also possible that a hole spin flip is responsible for the exciton dephasing, for example due to interactions with other holes from the acceptor level of the p region.

Choosing a bias to maximise the emission from the biexciton decay and the degree of polarisation correlation would benefit QD devices based on the biexciton decay, such as an entangled photon pair source.

4.4 Single quantum dot memory

The experiments in this section detail the operation of the same device as in the previous section, acting as a single electron-spin memory.

4.4.1 Quantum information processing

The basic unit of quantum information is a qubit, which is the quantum analogue of the classical bit [40]. Various physical systems have been proposed to encode a qubit, including the polarisation of a single photon [69, 70], the spin of an electron or an atomic nucleus [26, 31], and the charge state of a quantum dot or superconducting island [84, 98]. The use of the polarisation of a photon makes single qubit operations straight forward, i.e. using appropriate wave plates. Furthermore photons have the advantage that they are easy to transmit between two distant points, as required for the 'flying qubit' in, for example, quantum cryptography [16] and photonic quantum computing [69]. However photons are hard to store for a long time and do not interact strongly with one another, hindering simple multiple qubit operations. On the other hand, electron spins are easy to store and manipulate in a suitable solid-state environment but are difficult to transmit over long distances.

The experiments described in this section show that the QD in a $p-i-n$ diode device can act as an interface between these two systems, so that the advantages of both can be accessed. The polarisation information of a single photon is stored as the spin of a single electron trapped in a QD and is deterministically recovered some time later.

4.4.2 Device operation

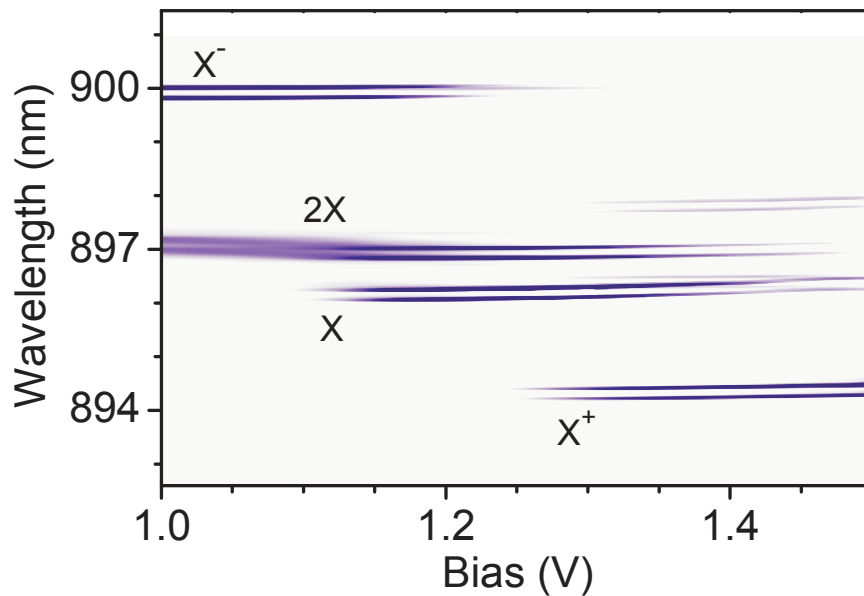


Figure 4.7: PL from a single QD in the device with a magnetic field of 2 T in the Faraday geometry, as a function of applied bias.

Figure 4.1 shows the structure of the device, as before. Figure 4.3 show a simplified versions of the band structure of the device around a single QD. In the diagram, the electron tunneling barrier, grown 5 nm underneath the QD layer, is represented by a higher potential barrier to the right of the QD.

The operation of the device shares many similarities with the device presented in reference [73], in which an ensemble of InAs QDs are embedded in the intrinsic region of a p -type GaAs Schottky diode. The use of a $p-i-n$ diode in this work allows the integration of an optical cavity into the design (see figure 4.1), to

4.4 Single quantum dot memory

enhance the intensity of the emission. Furthermore, by addressing a single QD, a significant step has been made towards the quantum information processing goal of storing the polarisation information of a single photon.

The device is operated with an applied magnetic field of 2 T in the Faraday geometry. This field is big enough so that the Zeeman interaction is much larger than the fine structure splitting (i.e. $g\mu_B B \gg S_0$) so that the two $m = \pm 1$ exciton pure spin states are recovered (see section 2.2.5). The photons emitted in the decay of these states are therefore circularly polarised. Figure 4.7 shows PL from a single QD in the device with the field turned on, as a function of bias applied across the diode. As before, in figure 4.2, the bias controls which excitonic state is dominant in the spectrum. However, the magnetic field introduces a Zeeman interaction and splits the lines in energy into well resolved doublets.

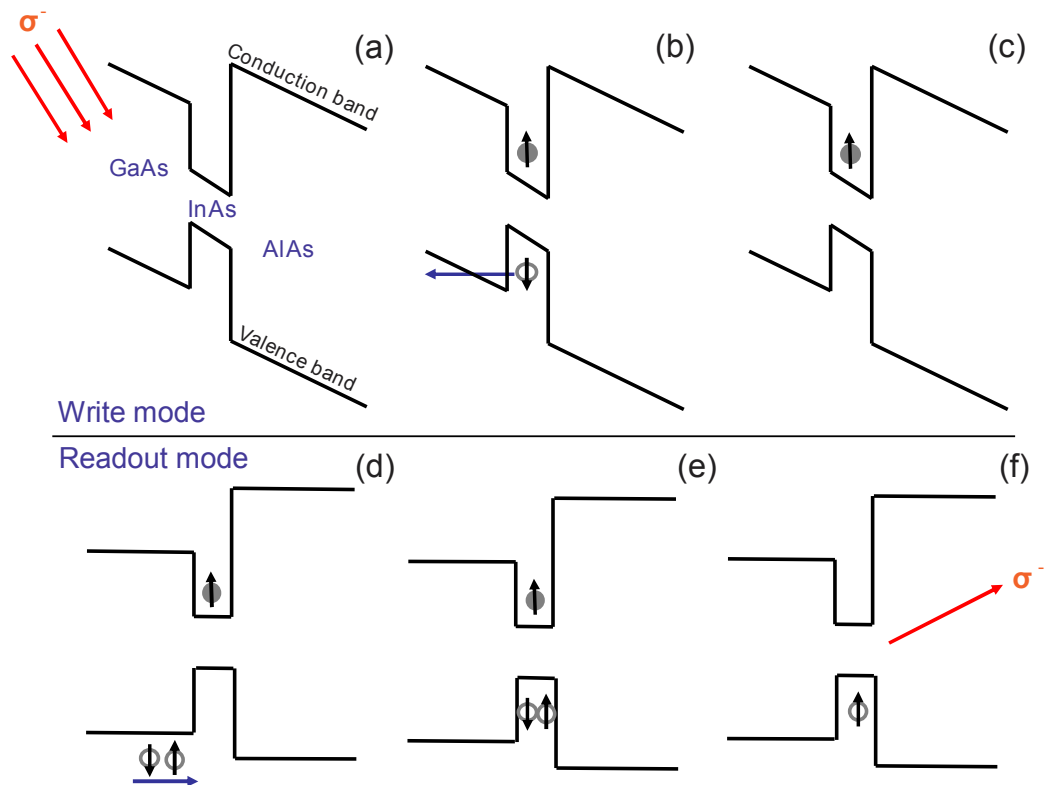


Figure 4.8: Simplified band diagrams illustrating the operation of the device.

When a circularly polarised photon is absorbed by the device, an electron is promoted to the conduction band whose spin (up or down) is deterministically determined by the polarisation of the initial photon (left or right), according to the conservation of angular momentum selection rules (see section 2.2.3). In the write mode of the device (figure 4.8 (a)-(c)), it is biased so that the hole tunneling rate is much faster than the radiative lifetime of any of the optical transitions. Carriers are excited into the wetting layer by a circularly polarised laser pulse. The pulse is weak so that on average only one electron and one hole will relax into the QD. The hole will tunnel out from the dot and drift towards the p region, whereas the tunneling barrier prohibits the electron from leaving the dot. A single electron is left in the quantum dot whose spin state is determined by the polarisation of the initial photon.

In readout mode (figure 4.8 (d)-(e)), a higher positive bias is applied to the device to return two holes to the dot. Radiative recombination of the stored electron with a hole results in the emission of an X^+ photon with identical polarisation to the initial one. It can be ensured that two holes are returned to the dot by using the correct positive bias so that emission from X^+ is dominant. The use of two holes ensures that there is always a hole with the correct angular momentum to annihilate with the electron. This means that long lived dark excitons are not formed which would slow down the operation of the device and reduce its efficiency.

4.4.3 Experimental set-up

The simplified experimental arrangement used to test the device's memory operation is shown in figure 4.9. Section 3.3 contains more details. A multimode diode laser emitting at 869 ± 5 nm which had pulse lengths of ~ 100 ps and a variable repetition rate was used to excite carriers in the wetting layer of the device. The laser was linearly polarised before passing through a quarter wave plate (QWP) with its fast axis orientated at $\pm 45^\circ$ to the angle of polarisation. Thus the beam was left or right circularly polarised when it excited the device. PL from the device was passed through the same QWP which rotated circularly polarised components back to the linear basis. Finally a combination of a half

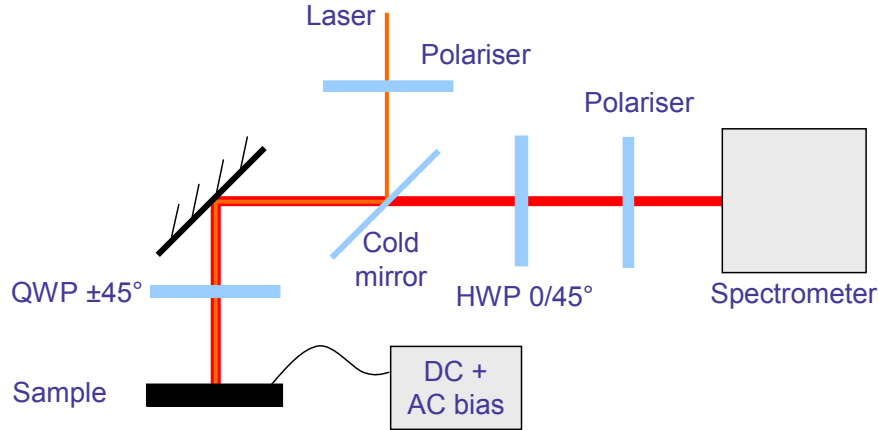


Figure 4.9: Simplified schematic diagram of experimental set-up for the memory experiment (see figure 3.2 for more detail).

wave plate (HWP) and a linear polariser selected one of the linear polarisations (H or V) to be transmitted to the spectrometer. It was therefore possible to excite with and detect either of the circular polarisations.

An AC pulse generator was synchronised with the laser's clock and applied an AC pulse to the device some time (shorter than the period of the laser) after the laser pulse. The circularly polarised laser light populated the quantum dot with an electron. During the delay time, it was anticipated that the electron's spin would be preserved. The application of the AC pulse switched the device to readout mode, and light of the original polarisation was expected to be emitted from the device at the wavelength of the positively charged exciton. A small DC bias was also applied which was used to optimise the emission.

4.4.4 Quantum dot electron-spin memory

Figure 4.10 (a) shows time resolved PL from the X^+ state of a single QD in the device. A DC bias of 1.4 V was applied so that emission from the state was triggered by the laser pulse. Figure 4.10 (b) shows time-resolved PL from the same QD, with the laser pulsed at 1 MHz and with an AC pulse applied to the device on top of a small negative DC bias. The delay between the laser pulse and

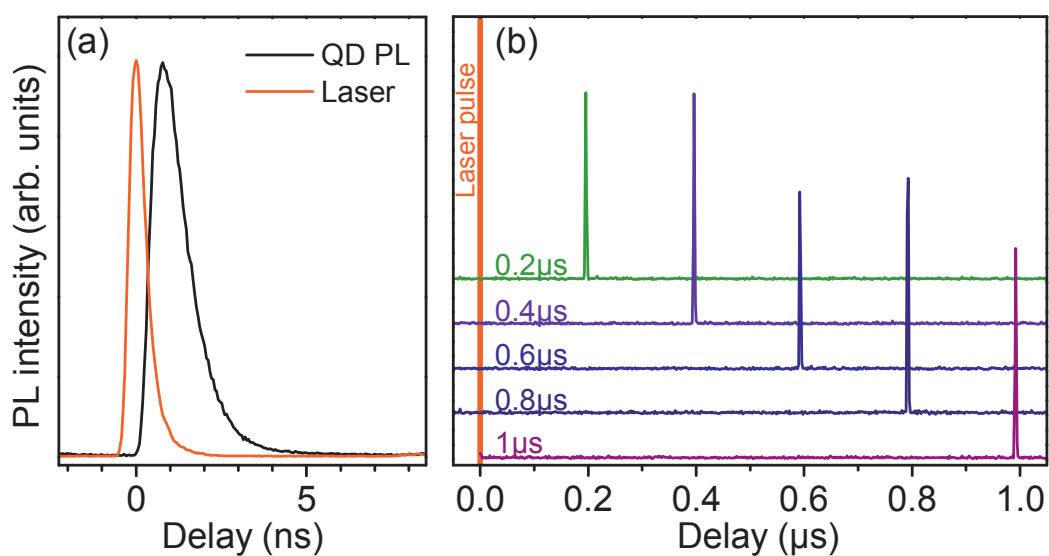


Figure 4.10: (a) Time-resolved PL of the laser (red) and the positively charged exciton of a single QD (black) with an applied DC bias of 1.4 V. (b) Time-resolved PL from the same dot with a DC bias of -0.05 V to remove the holes from the dot. 0.2 to 1.0 μs (as labeled) after the laser pulse, an AC pulse of 2.7 V was applied to return two holes to the dot. Emission from the X^+ state is delayed and correlated with the AC pulse.

the AC pulse is varied from 0.2 to 1 μs . The emission is clearly triggered by the AC pulse and not the laser pulse.

When the laser light was removed, no luminescence was measured. This demonstrates that the emission is due to an electron being stored in the QD and is not due to electroluminescence induced by the AC pulse. The variation in the area of the peaks in figure 4.10 (b) is due to fluctuations in the laser pulse intensity, caused by small lateral movements of the device in the cryostat. Impedance mismatches between the circuitry used to deliver the AC pulses and the device meant that the pulses were somewhat attenuated before they reached the device. Therefore a higher voltage AC pulse was required to put the device into a given state as compared to the DC bias equivalent. An electron storage of up to 1 μs was measured with no observable decay in the intensity, indicating that longer storage times should be possible.

Figure 4.11 shows the polarised PL emitted from the delayed X^+ state with a magnetic field of 2 T in the Faraday geometry, when exciting the sample with differing polarisations. The AC pulse was delayed by $\sim 1\mu\text{s}$ with respect to the laser pulse. With unpolarised excitation, each pair of lines shown in figure 4.7 were polarised in opposite circular polarisations, as expected. When the laser light was horizontally linearly polarised (top panel), two equal peaks corresponding to the two pure spin states of X^+ were measured. This occurs because the linearly polarised laser light excites equal numbers of up and down spin electrons in the device so that the spin of the electron confined in the dot is random.

The bottom two panels of figure 4.11 show that when the laser light was circularly polarised, the vast majority of the delayed emission had the same polarisation. This demonstrates that the spin of the electron is preserved during the process of non-resonant excitation, relaxation into the dot, removal of the hole from the dot and the re-injection of two holes.

The fidelity of the polarisation memory, defined as

$$F = I_{L,R}/(I_L + I_R), \quad (4.2)$$

was measured to be $90 \pm 5\%$ for both laser polarisations and constant over the measured delay range of 0.2-1 μs . I_L is the integrated intensity of the left-hand

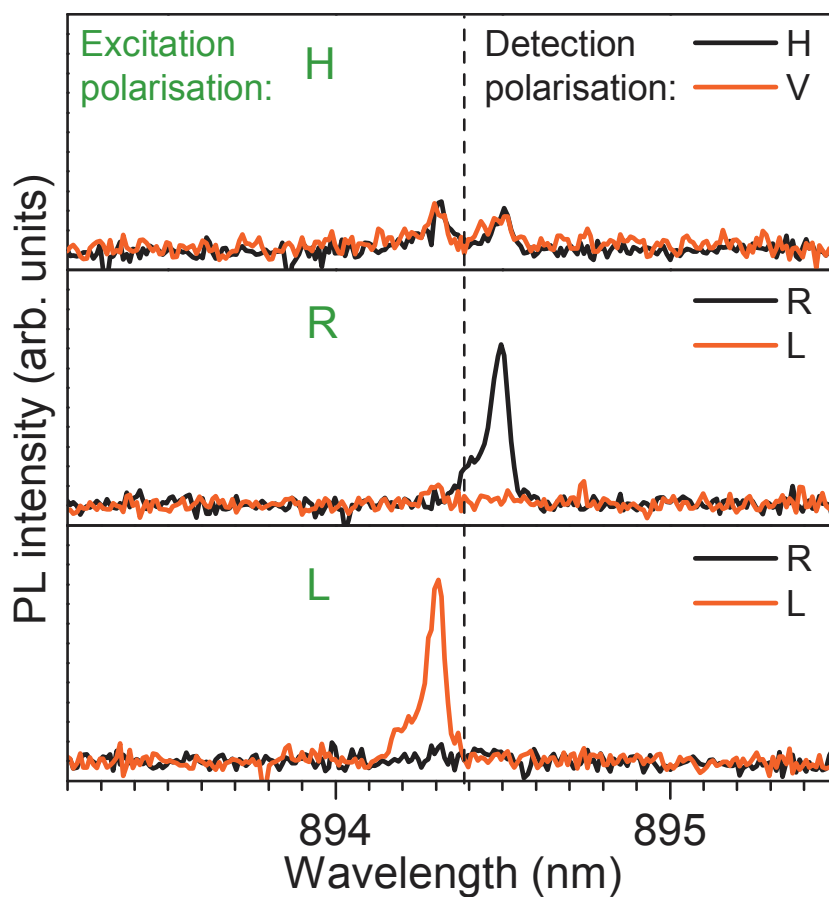


Figure 4.11: PL from X^+ delayed by $\sim 1\mu\text{s}$ in a single QD with a magnetic field of 2 T applied in the Faraday geometry. The pump polarisation and detection polarisation are different in each of the panels - horizontal (H), vertical (V), right hand circular (R) or left hand circular (L) - as labeled. The black dotted line is shown as a guide to the eye.

circularly polarised X^+ emission peak and I_R is that of the right-hand circularly polarised peak. The value is not 100% due to polarisation errors in the experimental set-up and a degree of spin-scattering during the relaxation of the electron into the dot after the non-resonant excitation, i.e. a non-unity fidelity of the write operation.

The asymmetric line shapes of the emission in figure 4.11 are a result of a variable Stark-shift due to the varying electric field from the AC pulse. The turn on time of the AC pulse, which was limited by the equipment used, was of the same order as the radiative lifetime of the X^+ . Therefore, the energy shift induced by the Stark effect varied throughout the readout cycle. The slow turn on time also allowed some light to be emitted from the neutral exciton line which was not collected in the experiment. This caused a factor of 2 difference in the intensity of the electrically triggered and laser triggered X^+ emission.

4.4.5 Summary and outlook

Storage of the polarisation information of a photon as the spin state of an electron in a QD and its electronically triggered readout has been demonstrated. The difference in energy between the input and output photons could allow the transfer of information between systems operating at different wavelengths.

A storage time of up to 1 μs was demonstrated, although this was limited by the repetition rate of the device, which was in turn limited by the intensity of the measured emission. It is expected that the spin memory will persist longer than this. Similar experiments using multiple QDs have shown storage times of over 1 ms [73].

The readout time was limited by the radiative lifetime of the X^+ transition. Coupling the transition to a high- Q mode of an optical cavity (for example a photonic crystal cavity - see chapters 6 and 7) would decrease the lifetime of the state and therefore increase the possible speed of operation.

The non-resonant excitation in the wetting layer limited the degree of polarisation memory. The use of larger QDs with more confined energy levels could allow quasi-resonant excitation through a fast relaxing excited state. This would

4.4 Single quantum dot memory

improve the transfer of polarisation information from the input laser to the stored electron's spin.

For a true quantum memory, resonant excitation would be required to enable writing of superposition states, and storage of the hole would be necessary. This could be done, for example, with a quantum dot molecule.

Chapter 5

Designing and fabricating photonic crystals

5.1 Overview

Quantum dot based devices, like the one discussed in the previous chapter, can benefit from an optical cavity. In section 2.3, it was shown that cavity effects can enhance the spontaneous emission rate from a QD and can drastically increase the collection efficiency of the emission from the device. In the same section, it was shown that photonic crystal cavities are the best choice for many applications because of the high Q -factors achievable, along with their tiny mode volumes.

This chapter details efforts made in designing and fabricating photonic crystal structures with the goal of enhancing the properties of quantum dot devices. It begins with a discussion on the simulation technique used to design the structures and goes on to discuss the problems encountered when trying to fabricate them.

5.2 Finite-difference time-domain simulation

Finite-difference time-domain (FDTD) simulation was used to design the photonic crystal structures studied in this work. FDTD is a simulation technique which provides a numerical solution to Maxwell's equations for the electromagnetic fields in a material with arbitrary $\epsilon(\mathbf{r}, \omega)$ and $\mu(\mathbf{r}, \omega)$. It relies on the fact that in

5.2 Finite-difference time-domain simulation

Maxwell's equations, a change in the electric field in time is dependent on the change in the magnetic field in space, and vice versa (see equation A.1).

The simulation domain is split into a grid with grid points spaced Δx , Δy and Δz apart. At each grid point (i, j, k) the electric and magnetic field components are calculated at the points on a Yee cell, as shown in figure 5.1. Time is also discretised into steps of Δt . The calculation is carried out in an iterative manner: the electric field at each grid point is calculated at time $t = n\Delta t$, followed by the magnetic field at time $t = (n + 1/2)\Delta t$, followed by the electric field at time $t = (n + 1)\Delta t$, where n is an integer, and so on. The electric field at time $t = n\Delta t$ is equal to the electric field at $t = (n - 1)\Delta t$ plus an additional term computed from the spatial variation of the magnetic field at time $t = (n - 1/2)\Delta t$.

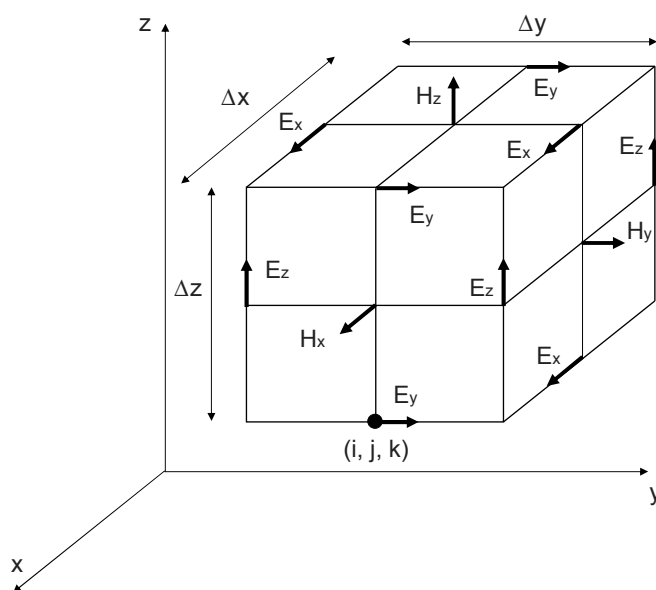


Figure 5.1: Yee cell used in FDTD simulation. The electric and magnetic field components are computed at points shifted half the grid spacing from one another.

In practice the material parameters, the computational domain, and details of the electromagnetic field excitation are input into a simulation. The spatial grid is defined, which should be small enough to resolve the smallest feature of the simulated field, and the time step is chosen, which must obey the Courant condition,

$$c\Delta t < \frac{1}{\sqrt{1/\Delta x^2 + 1/\Delta y^2 + 1/\Delta z^2}}, \quad (5.1)$$

to obtain a stable simulation. The boundary conditions at the edges of the computational domain must also be specified. The most common choice in this work is the perfectly matched layer (PML), which absorbs the incident radiation without producing back reflections.

5.3 FDTD for photonic crystals

A commercial FDTD package, RSoft FullWAVE, was used for simulations in this work. This section will describe the particular techniques used to calculate the spectrum of a given photonic crystal structure and to find the Q -factor, profile and volume of its confined modes.

5.3.1 Boundary conditions

PML boundary conditions were used for most of the boundaries as shown in figure 5.2. However, a symmetric mirror boundary condition was used to cut the simulation domain in half through the centre of the slab. This was possible since all the TE-like modes of interest in this work are symmetric about the centre of the slab, with only one anti-node in the field profile.

5.3.2 Calculating the spectrum

To calculate the spectrum, the structure of interest is first drawn out in a CAD environment, with the relevant refractive index assigned to each component. A number of electric dipole-like sources are then positioned throughout the cavity. Electric field monitors are placed inside the cavity and just outside the cavity. Figure 5.3 shows a typical FDTD layout for a spectrum calculation.

The sources are made to emit a TE-polarised broadband impulse field at time zero. As the simulation progresses in time, this field is allowed to dissipate throughout the simulation domain. Most frequencies of the impulse field will pass

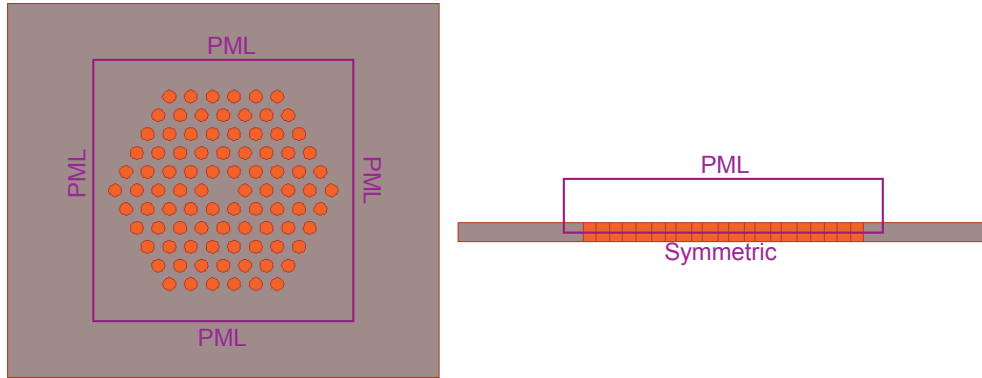


Figure 5.2: Planar view (left) and cross-sectional view (right) of the typical boundary conditions used for photonic crystal simulations. The purple lines represent the simulation domain edges with the boundary conditions, perfectly matched layers (PML) or symmetric mirrors, labeled.

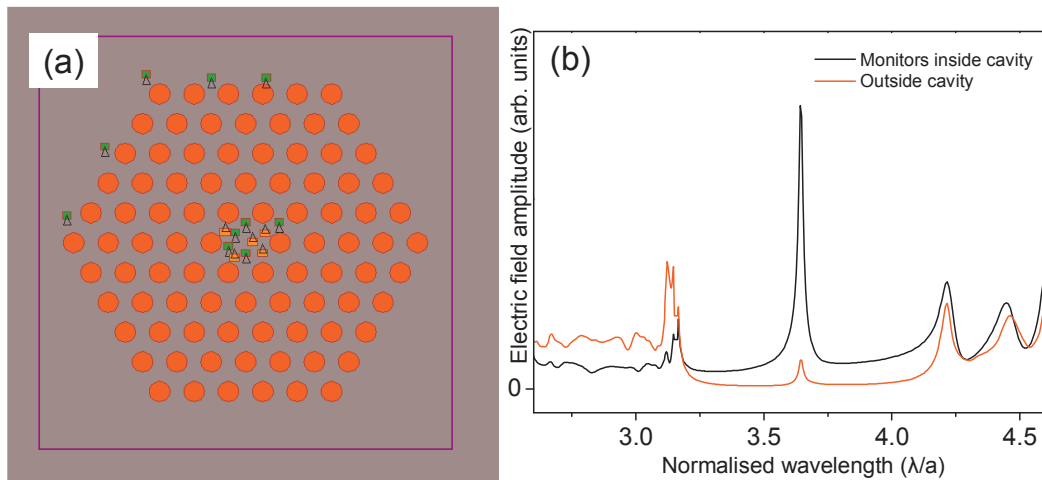


Figure 5.3: (a) Typical layout for an FDTD calculation of the spectrum of a photonic crystal cavity. Grey represent GaAs regions and red represents air regions. The purple line is the simulation boundary. The small yellow boxes are electric dipole-like sources and the small green boxes are electric field monitors. (b) Typical result from a spectrum calculation of an unmodified H1 cavity with $r/a = 0.3$, $d/a = 0.7$, $n = 3.53$ and 5 photonic crystal periods surrounding the defect. The black and red lines are the sums of the spectra from the monitors inside and outside the cavity respectively.

relatively undisturbed throughout the structure and will be picked up by all the monitors, inside and outside the cavity. Those frequencies within the photonic band gap will be inhibited from passing through the photonic crystal and will not be picked up by the monitors outside the cavity. The resonant frequencies of the TE cavity modes will be confined in the cavity and will be picked up mainly by the monitors inside the cavity.

The monitors are set to monitor the electric field as a function of time. After the simulation period has ended, a Fourier transform of the data is calculated to provide the frequency response at each monitor point, in which cavity modes are manifested as narrow peaks. A number of monitors are used and their spectra are summed together to give an approximate total spatially averaged cavity response. Care must be taken to avoid the situation in which one monitor is positioned at a point of high field intensity for a particular resonant mode. In this case, the spectrum may be dominated by the frequency of that mode, and other features may be swamped.

Figure 5.3 (b) shows a typical result for a H1 cavity. The black line is the summed spectra from five monitors placed inside the cavity, clearly showing a mode at $\lambda/a \sim 3.6$. The red line is from five monitors placed outside the cavity, which makes the extent of the photonic band gap clear. A small peak at the wavelength of the mode appears in this spectrum, showing that the use of five photonic crystal periods is insufficient to strongly confine the mode (see section 5.3.7).

5.3.3 Q -factor

An intuitive way to calculate the Q -factor of a mode would be to monitor the decay of the field energy stored in the mode as a function of time. By fitting the result to an exponential decay, Q can be extracted. However, this method can require prohibitively long simulation times to achieve accurate results.

Instead, a method based on Fourier analysis is implemented in RSoft Full-WAVE. In this method, the field picked up by a monitor is approximated as a sum of complex exponentials:

$$f(t) = \sum_j c_j e^{-i\tilde{\omega}_j t}, \quad (5.2)$$

where the complex frequency $\tilde{\omega}_j = \omega_j + i\gamma_j$ contains the oscillatory frequency ω_j and the loss rate γ_j , which is simply related to Q . The entire field is represented by a number of terms in this sum; even the parts of the field which radiate away quickly can be considered to behave like this but with a very high loss rate. This changes the problem to a fit of the parameters c_j and $\tilde{\omega}_j$ and allows accurate values of $\tilde{\omega}_j$ to be extracted from relatively short simulation times.

5.3.4 Mode profile

Mode profiles were calculated using two steps. Firstly, randomly positioned sources inside the cavity were set to emit a spectrally narrow CW field for the duration of the simulation, with a frequency identical to that of the mode of interest. A large area spatial field monitor was positioned at the centre of the slab and was set to return the values of E_x , E_y and H_z at the end of the simulation. The simulation time was set to be long enough so that a steady state situation was reached by its end. Stopping the simulation part way through an optical cycle ensured that energy was contained in both the electric and magnetic fields, so that both their profiles could be obtained from one simulation.

Following this, a second similar calculation was carried out with a single source positioned at a maximum in the electric field of the mode, to obtain a more precise profile, without any source induced distortions.

5.3.5 Mode volume

The mode volume is defined as

$$V_0 = \int_V \frac{U_E(\mathbf{r})}{\max[U_E(\mathbf{r})]} dV, \quad (5.3)$$

where

$$U_E(\mathbf{r}) = \frac{1}{2}\epsilon(\mathbf{r})|\mathbf{E}(\mathbf{r})|^2, \quad (5.4)$$

is the electric energy density of a mode and V is the whole simulation domain. It can be calculated directly from the mode profile. Since the electric energy density varies in time, for consistency the mode volume is evaluated at the point in the optical cycle where the electric energy is maximum.

5.3.6 Purcell factor

The maximum possible Purcell factor for a well positioned QD can be calculated by inputting the calculated values into equation 2.12.

5.3.7 Simulation convergence studies

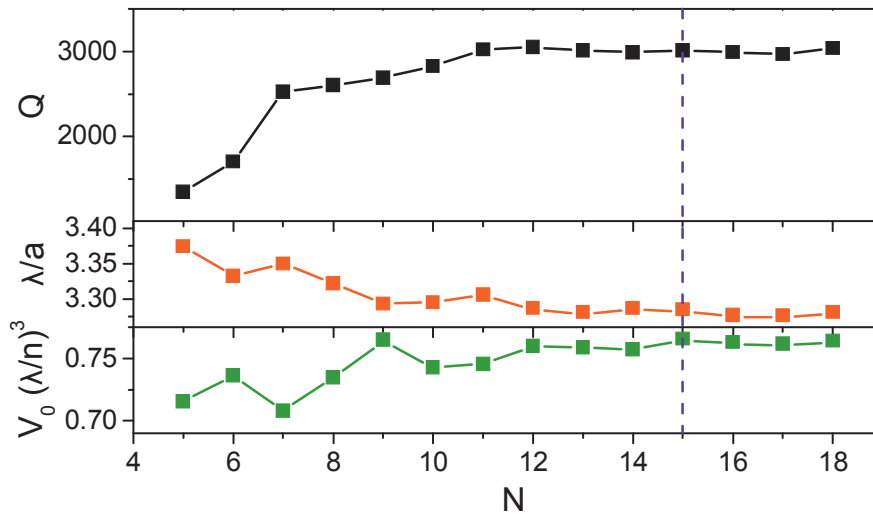


Figure 5.4: Results of simulations for the monopole mode of a H1 photonic crystal cavity as the size of the grid, $\Delta x = \Delta y = \Delta z = a/N$, is decreased. The cavity parameters are $r = 0.36a$, $r' = 0.2a$, $d = 0.7a$ with 5 photonic crystal periods surrounding the defect. The dashed blue line indicates the value used in the rest of this work.

5.3 FDTD for photonic crystals

Before any useful calculations could be performed, it was necessary to find suitable simulation conditions. Figure 5.4 shows the results of calculations in which the grid size of the simulation was progressively made smaller. For each grid size, the wavelength, Q -factor and mode volume were calculated for the monopole mode in a modified H1 cavity with $r/a = 0.36$, $r'/a = 0.2$, $d/a = 0.7$ with 5 photonic crystal periods surrounding the defect. r' is the radius of the six nearest neighbour holes which are modified to increase the Q -factor of the mode, as discussed in section 6.3.

For large grid dimensions, the features of the photonic crystal are not resolved properly and the resulting Q s are artificially low. As the grid size is made smaller, the structure is better resolved in the simulation, and the calculated Q converges towards the real value. The wavelength and mode volume follow similar patterns. This result motivated the choice of $\Delta x = \Delta y = \Delta z = a/15$ as the grid size used in the rest of this work.

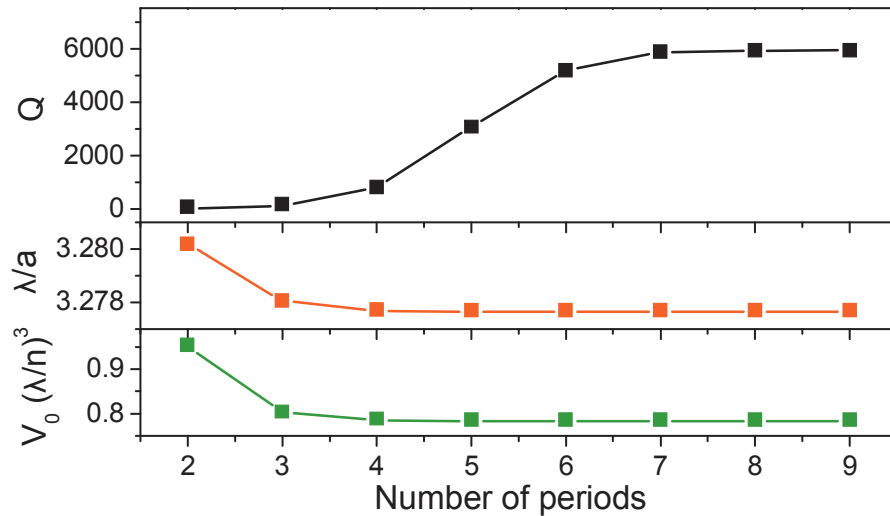


Figure 5.5: Results of simulations of the monopole mode of a H1 photonic crystal cavity as the number of periods is increased. The cavity parameters are $r = 0.36a$, $r' = 0.2a$ and $d = 0.7a$. The grid size is $\Delta x = \Delta y = \Delta z = a/15$.

Figure 5.5 shows a similar set of calculations as the number of photonic crystal periods surrounding the defect is increased. For small numbers of periods,

the mode is not well confined in-plane, and the calculated Q is low. At around 8 periods, Q saturates as the out-of-plane losses become the dominant loss mechanism. The wavelength and mode volume on the other hand reach stable values at around 5 periods. The rest of this work uses at least 5 periods surrounding the defect. The number is chosen for each simulation with the trade off between precision and long simulation times in mind.

5.4 Fabrication of photonic crystals

The task of fabricating photonic crystal structures is a considerable one. To produce a photonic band gap at a wavelength of around 900 nm, where the QDs emit, air holes with radii around 100 nm are required. Any small errors in the fabrication of the structure can lead to a dramatic loss in the quality factor of the cavity modes [6, 44]. For example, the walls of the holes must be both straight and smooth. Roughness can lead to optical scattering at the surfaces, and non-straight side walls leads to a non-optimum photonic band gap.

In this work, great effort was put into finding processing conditions to produce high quality structures. Several improvements were made to an initial processing method [46]. The quality of the processing was evaluated by examining the structures with a scanning electron microscope (SEM) and by comparing their measured Q -factors to the simulated values. In the following sections, the quoted Q -factors are for the monopole mode of an optimal modified H1 cavity (see section 6.3). The cavity is formed by shifting outwards and reducing the size of the six nearest neighbour holes surrounding a single defect, and has a simulated Q -factor of ~ 30000 .

A number of the changes made in the processing had knock-on effects on other areas. In particular, many of the changes required that the etching processes be re-optimised. For the sake of brevity and clarity, the details of these re-optimisation steps are not included.

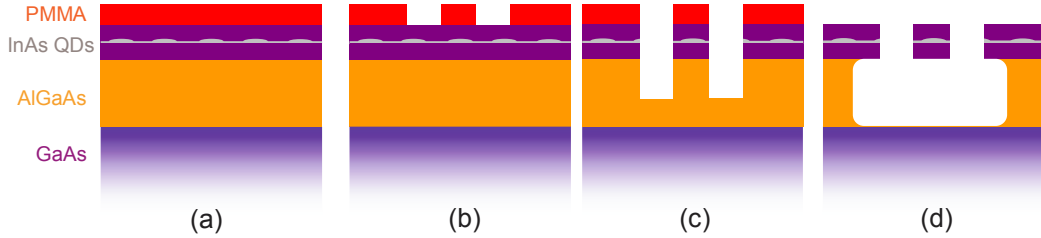


Figure 5.6: Schematic diagram of the initial method to produce photonic crystals. A layer of electron-beam patterned PMMA (b) is used as an etch mask for a SiCl_4/Ar based RIE etch of the GaAs slab (c). HCl is used to selectively etch the underlying AlGaAs layer (d).

5.4.1 Initial process

Figure 5.6 shows the initial scheme to fabricate two-dimensional slab photonic crystals. A wafer is grown comprising a 100 nm GaAs buffer layer on a GaAs substrate followed by a 500 nm AlGaAs sacrificial layer and a 150 nm GaAs slab with a layer of InAs QDs at its centre. An 80 nm thick layer of polymethyl methacrylate (PMMA) resist is spun onto the wafer and is patterned using electron-beam lithography with a current dose of $\sim 450 \mu\text{C}/\text{cm}^2$. The resist is developed and holes are etched into the chip using a reactive ion etching (RIE) process with SiCl_4 and Ar. Finally, the remaining resist is removed and the AlGaAs layer beneath the etched regions is removed by a selective wet etch with dilute HCl. This results in a suspended photonic crystal slab with air regions above and below.

After optimisation, the best Q -factors achieved with this method were around 2000. SEM images showed that the hole walls had a tapered profile (see figure 5.7). In the best case the size of the large holes was increased by around 16% at the top and were around 10% too small at the bottom, giving a taper angle of $\sim 12^\circ$. The small holes typically were increased by around 10% at the top and were $\sim 5\%$ too small at the bottom, giving a taper angle of $\sim 6^\circ$. The tapering was caused by the PMMA eroding very quickly at the edges of the holes during the etch.

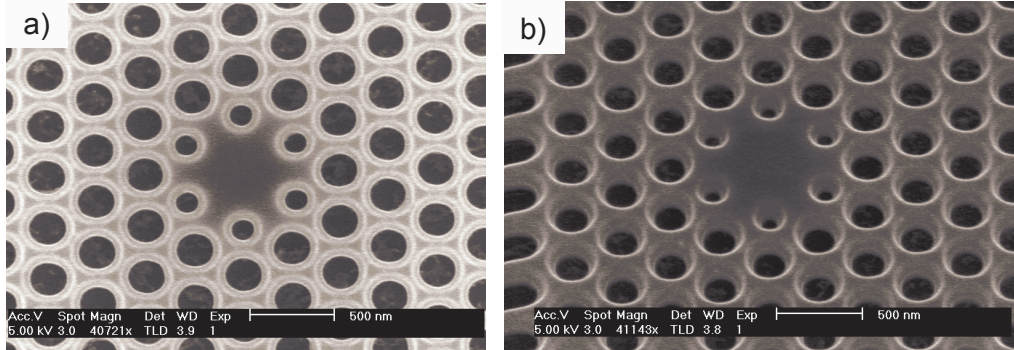


Figure 5.7: SEM images showing a photonic crystal cavity produced using the initial process. (a) Planar view, the tapered walls appear as bright rings around the holes. (b) Oblique angle view of the same cavity.

5.4.2 Electron beam resist

Silicon nitride approach

In an attempt to remove the tapering, a harder etch mask of silicon nitride (Si_3N_4) was used. Figure 5.8 shows a schematic diagram of the process. A ~ 150 nm thick layer of Si_3N_4 is deposited onto the wafer by plasma-enhanced chemical vapour deposition (PECVD). A layer of PMMA is spun on top of this and is exposed by electron beam lithography and developed. A trifluoromethane (CHF_3) based RIE process transfers the pattern into the Si_3N_4 layer, followed by a SiCl_4 based RIE etch into the GaAs using the Si_3N_4 layer as an etch mask. The remaining PMMA is removed before the Si_3N_4 is etched away by a combination of a second CHF_3 based RIE etch and a HF wet etch. Finally, the AlGaAs sacrificial layer is removed with dilute HCl.

After optimisation of the CHF_3 RIE process, SEM images revealed that the pattern transfer into the Si_3N_4 layer was very good, with smooth and straight side walls (see figure 5.9). The subsequent GaAs etch was much improved over the original process, with smoother and straighter side walls, indicating that a harder etch mask was beneficial to the RIE process (see figure 5.10). Furthermore, the size distribution of the holes was generally much narrower and more reproducible than for samples produced using PMMA. However, some undercutting

5.4 Fabrication of photonic crystals

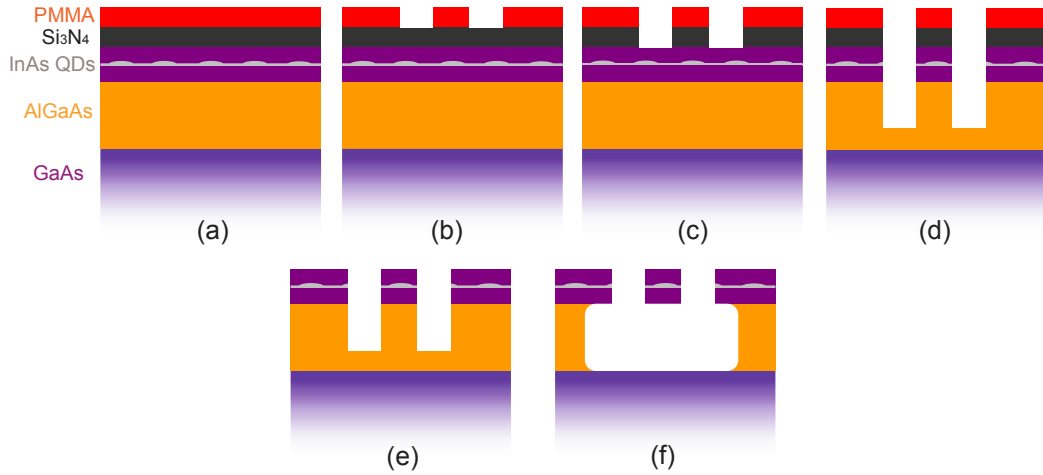


Figure 5.8: Schematic diagram of the photonic crystal fabrication method employing a layer of silicon nitride. A CHF_3 based RIE process transfers the photonic crystal pattern from a layer of PMMA (b) into a Si_3N_4 layer (c). A SiCl_4/Ar RIE process then transfers the pattern into the GaAs slab using the Si_3N_4 layer as an etch mask (d). The remaining Si_3N_4 is removed with a second CHF_3 etch (e), before etching away the AlGaAs layer with HCl (f).

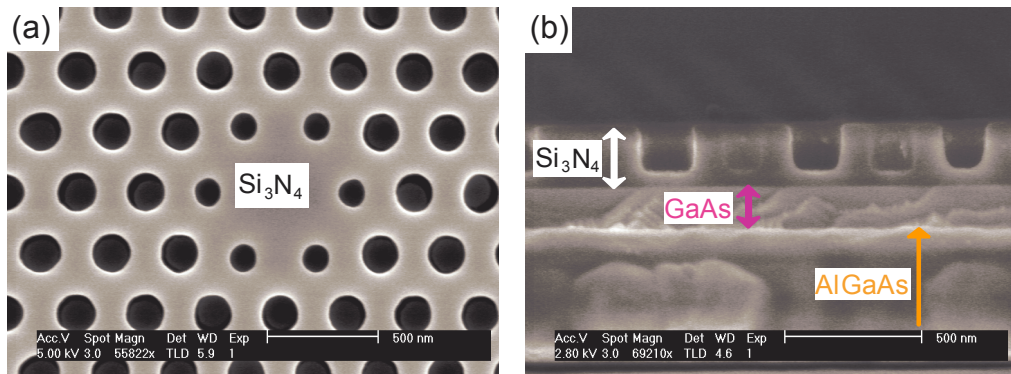


Figure 5.9: (a) SEM image of the Si_3N_4 surface after the CHF_3 RIE etch and removal of the PMMA. (b) Cross-sectional SEM image of the air holes etched into the Si_3N_4 layer showing straight and smooth side walls.

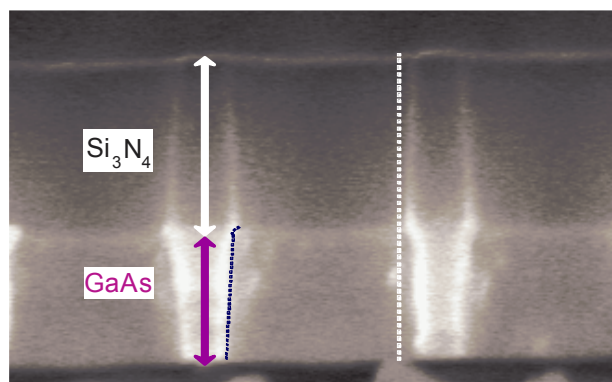


Figure 5.10: Cross-sectional SEM image of a photonic crystal cavity after etching the pattern from the Si_3N_4 layer into the GaAs. Slight undercutting and roughness are observed. The dashed blue and white lines are guides to the eye to emphasize the profile of the etched hole in GaAs and to show a straight reference, respectively.

and roughness were still present.

These improvements did not translate into a significant increase in the Q -factors, the maximum achieved was around 3000. It was found that this was due to the imperfect removal of the Si_3N_4 layer at the end of the process, which degraded the device Q .

ZEP520A

ZEP520A is an electron beam resist which has a heavier molecular weight than PMMA and is therefore more resistant to etching. It also has a higher sensitivity than PMMA but with an equivalent resolution, so that a lower electron beam dose is required to expose it. This resist was used in place of PMMA in the hope of achieving better photonic crystals.

A process was developed in which a 250 nm layer of ZEP was spun onto the wafer, which was then baked at 180°C for one hour. A thin layer of E300 anti-charge coating was spun on top of this layer, to reduce the build up of charge in the ZEP during the exposure. The optimum electron beam dose was found to be $120 \mu\text{C}/\text{cm}^2$ for the photonic crystal pattern and $200 \mu\text{C}/\text{cm}^2$ for the large

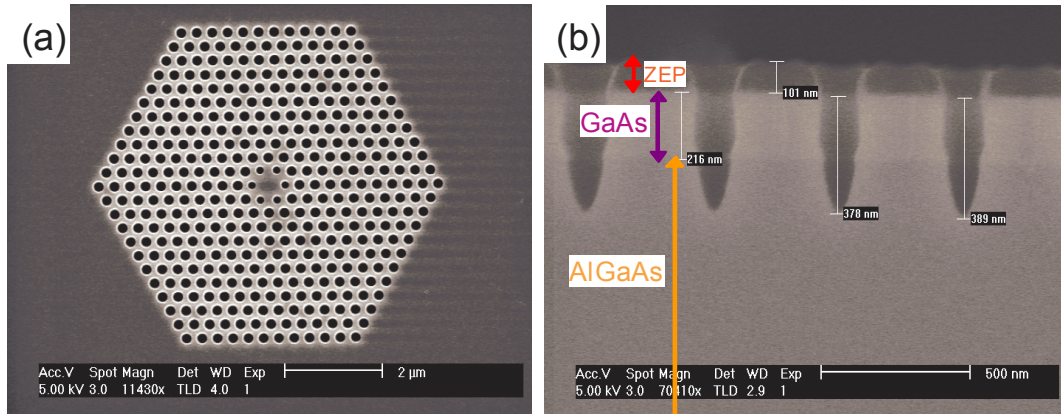


Figure 5.11: (a) SEM image of a completed photonic crystal cavity produced using ZEP520A resist. (b) Cross-sectional SEM image of a photonic crystal structure before removing the ZEP from the surface and under-etching the AlGaAs layer. The air holes are somewhat rough and barreling is present.

aligning features. After the exposure, the anti-charge coating was removed by spinning with a droplet of de-ionised water and the ZEP was developed with xylene. Following the RIE etch, the remaining ZEP was removed by exposing it to ultra-violet light for 5 minutes and immersing it for 10 minutes in hot ($\sim 80^\circ\text{C}$) N-methyl-2-pyrrolidone (NMP).

The use of this resist, after re-optimisation of the processing, led to much straighter and smoother side walls as compared to PMMA because of the greater resistance to dry etching. Furthermore, there were no problems with its removal since exposure to ultra-violet light decomposes the polymer. Figure 5.11 shows SEM images of the photonic crystals produced using ZEP520A resist.

5.4.3 AlGaAs sacrificial layer

The AlGaAs layer beneath the GaAs slab greatly affects the quality of the photonic crystals. A number of changes to its composition were made, which will be detailed in this section.

Layer thickness

Firstly, the thickness of the layer was increased from 500 nm to 900 nm. After the removal of the AlGaAs layer, the GaAs surface beneath it acts as a mirror. It has been shown that the position of this bottom mirror can affect the Q -factors of the cavity modes [66]. According to the literature, the choice of 900 nm (i.e. λ) is close to optimum and will decrease the possibility of light confined in a mode evanescently coupling to the GaAs layer below.

AlGaAs aluminium content

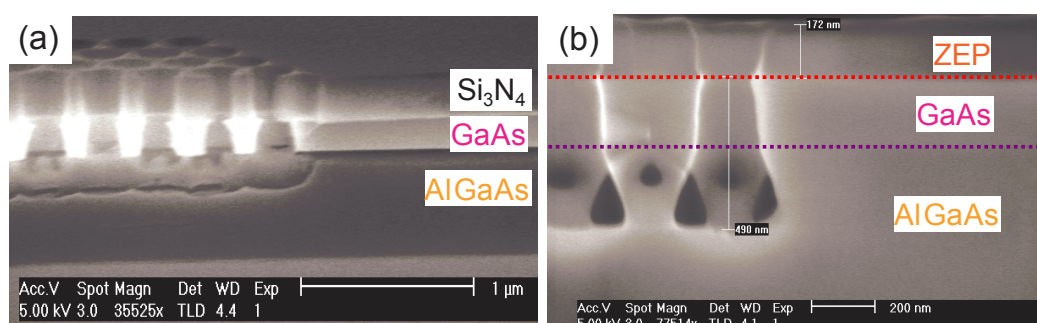


Figure 5.12: (a) Cross-sectional SEM image of a photonic crystal with a high Al content (98%) AlGaAs layer after the RIE etch. Hollow regions have opened up in the AlGaAs layer beneath the GaAs slab, due to the high reactivity of the AlGaAs. The profiles of the GaAs air holes are undercut as a result. Note that the sample shown has been processed using a Si₃N₄ mask. (b) Cross-sectional SEM image of a photonic crystal after etching with a 70% AlGaAs layer. The dashed lines indicate the locations of the material boundaries.

The aluminium content of Al_{*x*}Ga_{1-*x*}As is easily controllable during the MBE growth. AlGaAs with higher Al content is more reactive and will therefore etch faster during both the dry and wet etches. Initially, the Al content of the AlGaAs was high at 98% (i.e. Al_{0.98}Ga_{0.02}As), which caused problems during the dry etching stage. When the etch reached the AlGaAs layer, the etching rate increased and the AlGaAs was etched sideways. This caused hollow regions to open up beneath the GaAs slab through which the reactive ions could flow. These ions

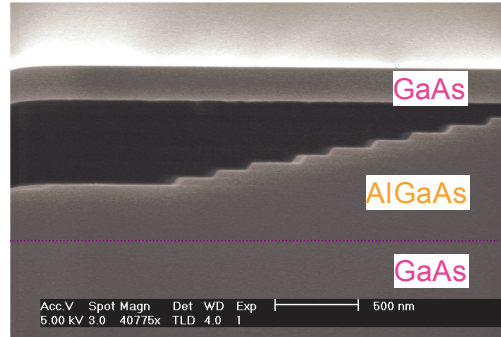


Figure 5.13: Cross-sectional SEM images of a photonic crystal after under-etching showing a step-like profile in the digital alloy AlGaAs layer. The AlGaAs has not been fully etched to the GaAs beneath. The dashed line indicates the location of the lower AlGaAs/GaAs boundary.

could then etch the bottom of the GaAs air holes, leading to undercut hole profiles, as shown in figure 5.12 (a).

This problem was reduced by lowering the Al content of the AlGaAs to 70%, which lessened the tendency of the AlGaAs to etch sideways (see 5.12 (b)). Furthermore, by aiming to etch only a short way into the AlGaAs layer the formation of the hollow regions was prohibited, and the best hole profiles were obtained.

AlGaAs can be grown in a number of ways. It was found that AlGaAs grown as a digital alloy, or with GaAs smoothing layers could not be removed in a reproducible way during the selective under-etch. The high Ga regions etched at a slower rate than the high Al regions, behaving as etch stops. The AlGaAs was therefore etched at a faster rate sideways than it was downwards, so that the resulting layer had a step-like profile (see figure 5.13). Hence it was necessary to use non-digitally grown AlGaAs.

Etchant

Initially, dilute HCl was used to selectively etch the AlGaAs layer. However, it was found that small islands of AlGaAs were left over, both on the bottom of the GaAs slab, and on the top of the lower GaAs layer, as shown in figure 5.14. The remains on the bottom of the slab decreased the refractive index contrast

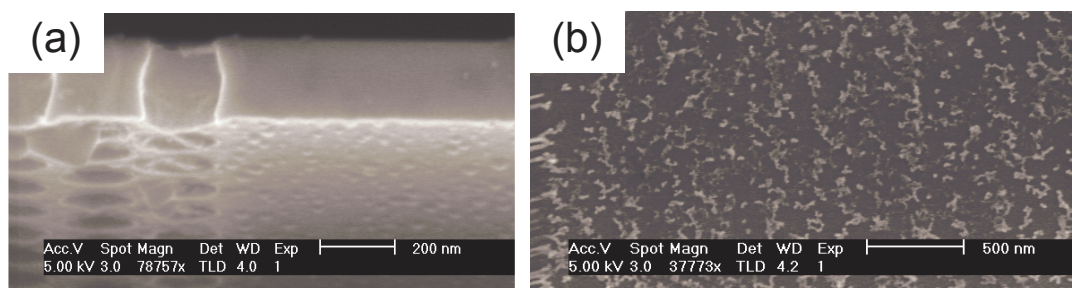


Figure 5.14: SEM images of the AlGaAs remains after selective etching with dilute HCl (a) underneath the GaAs slab, and (b) on the lower GaAs layer.

and introduced optical scattering at the GaAs/air interface, thus reducing the Q-factor. The remains on the lower GaAs layer had a detrimental effect on its properties as a mirror.

By switching to using HF for the under-etch, which is more aggressive, these islands were not produced. Using HF had another beneficial effect of removing any organic and oxide contaminants from the surface of the samples. This provided another motivation to use 70% Al content AlGaAs since higher Al contents were under-etched very aggressively by HF, so that many of the crystals collapsed.

A process was developed in which the RIE etched samples were immersed in a 48 % HF solution for 10 s followed by 100 s in a 7:1 buffered HF mixture. The use of buffered HF is preferable over concentrated HF since the etch rate is much more controllable. However, it was found that a short dip in concentrated HF was necessary to etch through the thin oxidised layer of AlGaAs which forms when the samples are exposed to air.

5.4.4 Dry etching

Reactive ion etching

SEM images of the entire process are shown in figure 5.15. The patterning of the resist was typically excellent, so the accuracy of the pattern transfer into the GaAs slab had the greatest effect on the final crystals. The use of ZEP520A resist, along with the necessary re-optimisation of the RIE process, dramatically improved the

5.4 Fabrication of photonic crystals

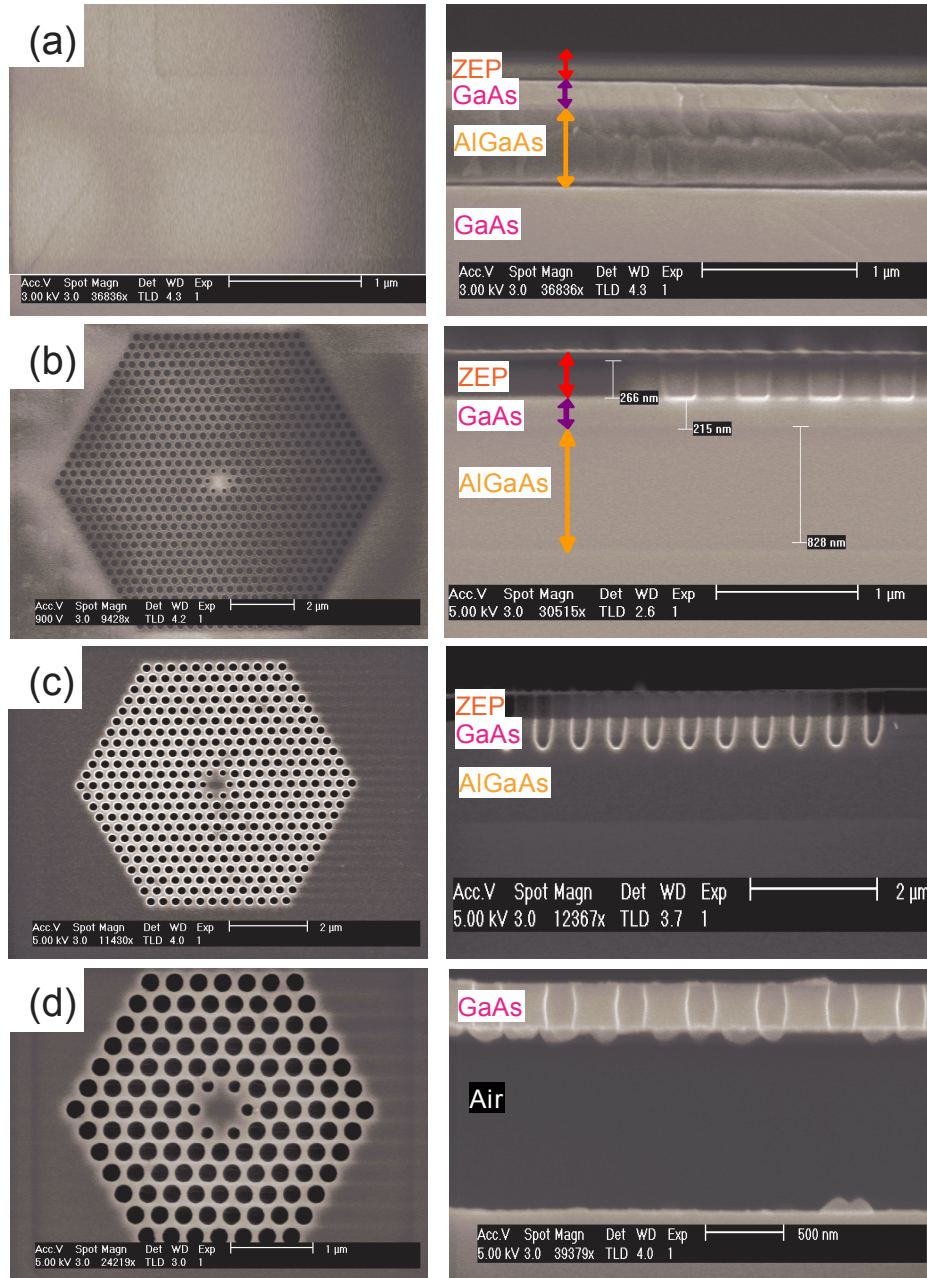


Figure 5.15: SEM images showing the steps involved in fabricating photonic crystals. (a) A layer of ZEP is spun onto the wafer. (b) The photonic crystal pattern is written by electron beam lithography, and the resist is developed. (c) The pattern is transferred into the GaAs slab by SiCl_4/Ar based RIE. (d) The AlGaAs layer is removed by a wet etch with HF.

quality of the crystals produced. This change, along with the others discussed in this section, brought the maximum Q -factor measured for the monopole mode of an optimal modified H1 cavity up to ~ 7500 .

This value, however, was still far from the ideal calculated value of 30000, and was not high enough for the intended applications (see chapter 6). Typically, the radii of the large holes were slightly increased by $\sim 3\%$ and the nearest neighbour holes were increased by $\sim 6\%$. The holes were very circular with a typical average circularity, defined as the ratio of the long and short axes of an ellipse, of $93\pm 4\%$. The air hole side walls were smooth but tended to exhibit barreling in their profile, as shown in figure 5.15 (d).

After extensive optimisation of the RIE process, it became apparent that this barreling was caused by inherent limitations of the RIE etching technology. It was therefore decided to change to an inductively coupled plasma RIE (ICP) process, as is discussed in the following section.

Inductively coupled plasma reactive ion etching

ICP is a similar technique to RIE which can achieve much higher plasma densities. In RIE, a strong radio frequency (RF) field is applied to an electrode in a vacuum chamber on which the sample to be etched sits, as shown in figure 5.16 (a). Controlled amounts of gas continually flow through the chamber and the pressure can be precisely controlled by a butterfly valve in front of the pump. The RF field ionises the gas molecules, creating a plasma. The free electrons in the plasma are strongly affected by the field and are accelerated up and down in the chamber. The electrons which are absorbed by the chamber wall, which is earthed, simply flow to ground. However, the electrons which are absorbed by the electrode cannot flow anywhere because it is DC isolated, so that a charge builds up.

The more massive positively charged ions are not as strongly affected by the RF field. When a negative charge builds up on the electrode, they are accelerated towards it where they collide with the sample. Etching occurs by the ions chemically reacting with the sample as well as sputtering it by transferring some of their kinetic energy. Since the ions generally collide with the sample traveling in the vertical direction, the etch is highly directional.

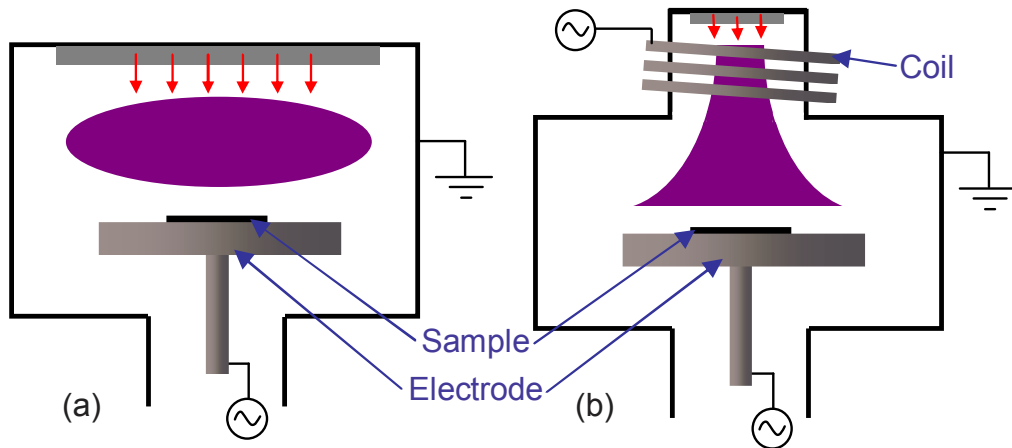


Figure 5.16: Schematic diagrams of the operation of RIE (a) and ICP (b). The purple shapes represent the confinement of the plasma. The red arrows show the input of the gases.

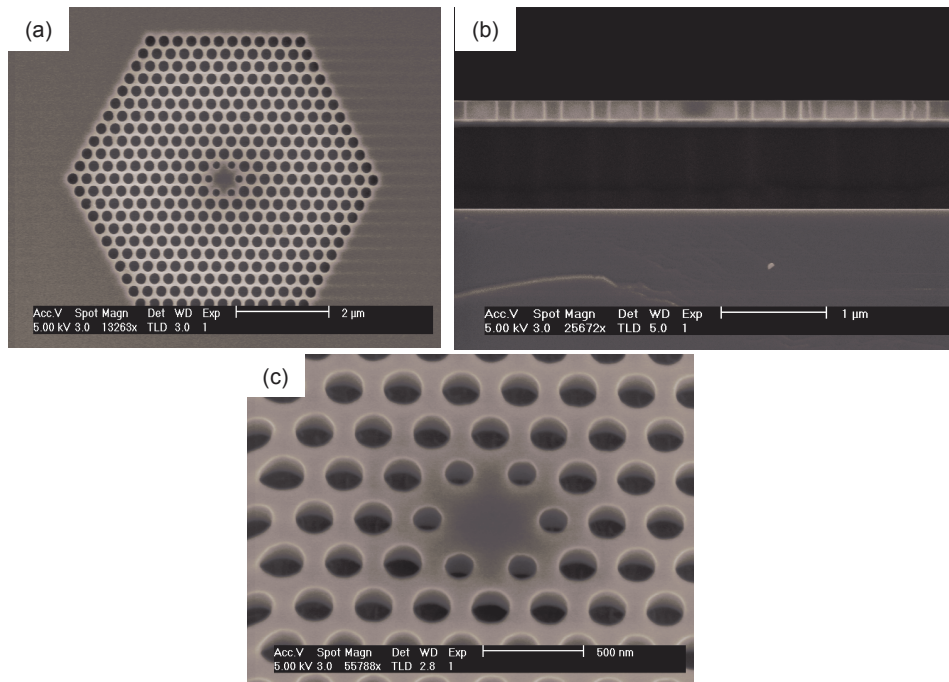


Figure 5.17: (a) SEM image of a photonic crystal cavity produced using ICP. (b) Cross-sectional image showing smooth and straight air hole side walls. (c) Oblique angle view of a cavity.

The main disadvantage of using RIE to fabricate photonic crystals is the fact that both the plasma density and the ion energy are controlled by the same parameter - the RF power. To achieve higher etching rates, both of these are increased, leading to a higher sputtering rate which can cause surface damage and roughness. ICP solves this problem by introducing a separate coil to produce the plasma, as shown in figure 5.16 (b). In this case the plasma density is controlled by the RF power applied to the coil and the ion energy is controlled by the RF power applied to the electrode. It is therefore possible to increase the etching rate by increasing the plasma density only, and not the ion energy.

A new ICP system was installed and configured as part of this work. After extensive optimisation of the process, it was possible to achieve very smooth and straight air hole side walls, as shown in figure 5.17. The inclusion of a laser interferometer system gave precise control over the depth of the etch, so that problems associated with the higher etching rate of AlGaAs could be avoided. These changes led to Q -factors of up to 9900, high enough to see strong coupling as detailed in chapter 6.

5.5 Summary and outlook

By implementing a number of changes to the processing method, it was possible to produce high quality photonic crystal structures. The most significant changes were the use of ZEP520A resist, the use of HF as the selective etchant and the installation and optimisation of a new ICP system. The fabrication process developed here is suitable to produce a wide variety of photonic crystal structures.

Chapter 6

H1 photonic crystal cavities for strong coupling

6.1 Overview

This chapter will detail experiments carried out with modified H1 photonic crystal cavities, with the goal of achieving strong coupling between an excitonic transition of a QD and the monopole mode of the cavity. The strong coupling regime offers a route for the practical realisation of future quantum information devices, such as quantum gates [35, 38, 42, 58], quantum memories [22] or sources of entangled photon pairs [61], and for the exploration of the physics of cavity quantum electrodynamics [63, 88].

Strong coupling with quantum dots has been observed in microdisks [108], micropillars [33, 113] and photonic crystal cavities [149]. 2D slab photonic crystal cavities are particularly suitable for the observation of the strong coupling regime due to their high Q -factor modes with tiny volumes [112, 138].

A H1 cavity consists of just one missing hole in a triangular lattice photonic crystal. Strong coupling between a single InAs QD and a mode of an L3 cavity (a line of 3 missing holes) has recently been achieved by several groups [35, 37, 50, 79, 95, 110, 144, 149]. However, only one group has reported strong coupling with a H1 cavity, using a nondegenerate polarised dipole mode and operating at ~ 970 nm [103].

The mode volume of H1 modes is typically smaller than L3 modes, so that the QD-cavity coupling parameter, g , is larger, which is beneficial for achieving strong coupling. Furthermore, the locally polarised nature of the L3 modes prohibit their use with QD entangled photon pair sources [28, 121]. If the two neutral exciton dipoles experience a different LDOS, the indistinguishability of the two decay paths in the biexciton decay will be broken, and the emitted photons will not be entangled [128]. In principle, it should be possible to overcome this limitation using the doubly degenerate dipole modes of a H1 cavity, since the local electric field in the centre of the cavity has no preferred direction [49, 78, 121].

6.2 H1 mode structure

As described in section 2.4.3, the H1 cavity can support a number of modes depending on its design [59]. The name of each of the modes is based on the shape of the field profile, for example the cavity may support monopole, dipole, quadrupole or hexapole modes. The mode wavelengths, Q -factors and mode volumes can be controlled by modifying the cavity parameters: the periodicity, a , hole radius r , and slab thickness, d . Figure 2.9 shows the calculated spectrum for a H1 cavity, with normalised hole radius $r/a = 0.3$ and slab height of $d/a = 0.7$ which supports a single dipole mode.

Furthermore, the positions and sizes of the holes surrounding the defect may be modified in order to increase the Q -factor of the modes [2, 106]. In the scheme used in this work, the radius of the six nearest neighbour holes is reduced to a value of r' and the positions of their centres are shifted radially outwards by an amount $s = r - r'$ as shown in figure 6.1 [46, 56, 107, 114]. Figure 6.2 shows the effect of this on the mode structure of the cavity: as the size of the cavity is increased, a series of other modes are pulled down from the air band into the band gap [46, 121].

The work presented here focuses on the monopole mode of the H1 cavity (M1 in figure 6.2). Although the far-field emission pattern is unpolarised, this mode is not suitable for use with entangled photon pair sources since the local field at the antinode has a preferred direction. However, it is ideally suited for observing strong coupling since the position of the QD should not be as critical as in other

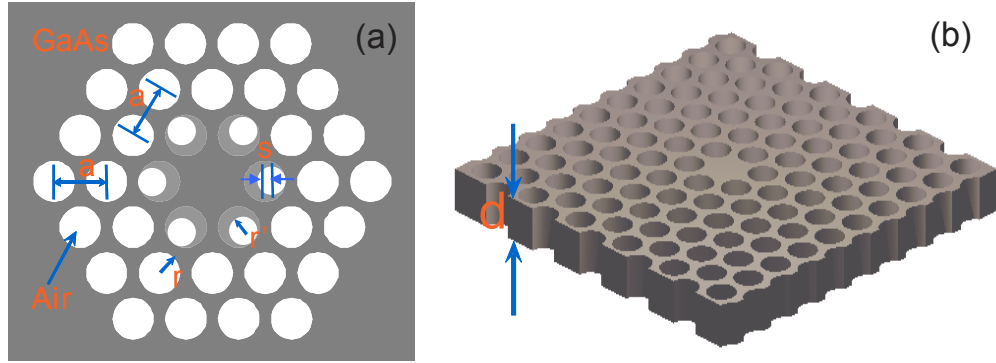


Figure 6.1: Schematic diagram of the scheme to modify the H1 cavity.

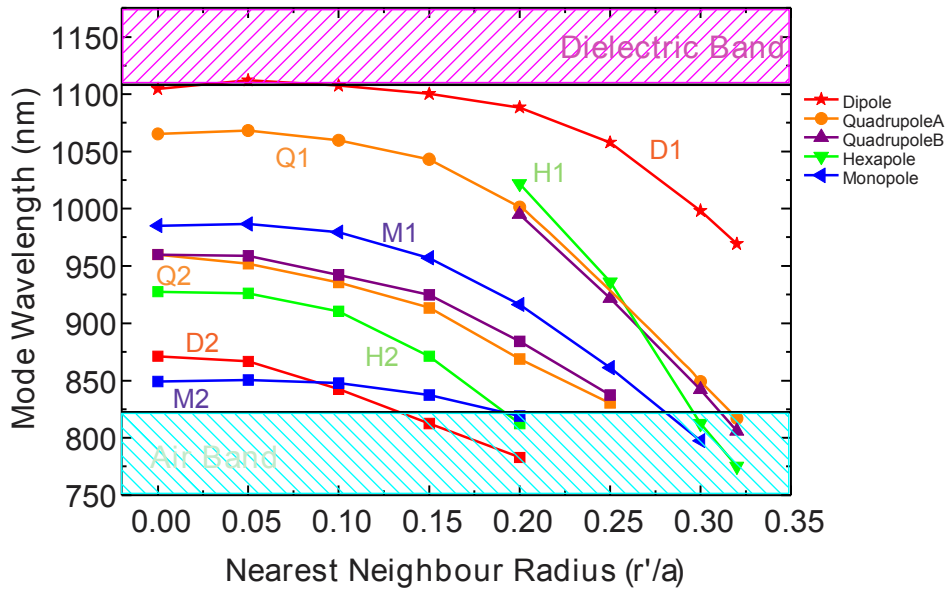


Figure 6.2: Simulated position of the modes in a H1 cavity as the radius of the nearest neighbour holes surrounding the defect, r' , is modified and their centres are shifted radially outward by $s = r - r'$. The cavity parameters are $r/a = 0.36$, $d/a = 0.411$ and $n = 3.53$. Courtesy of D. Gevaux.

modes due to the small number of nodes in its field profile. Furthermore, the light in the mode is confined away from the air holes, which due to fabrication imperfections can cause optical losses in practice.

6.3 Design and optimisation

This section describes FDTD simulations which were used to find the optimal parameters to maximise the Q -factor of the monopole mode.

6.3.1 Bulk hole radii

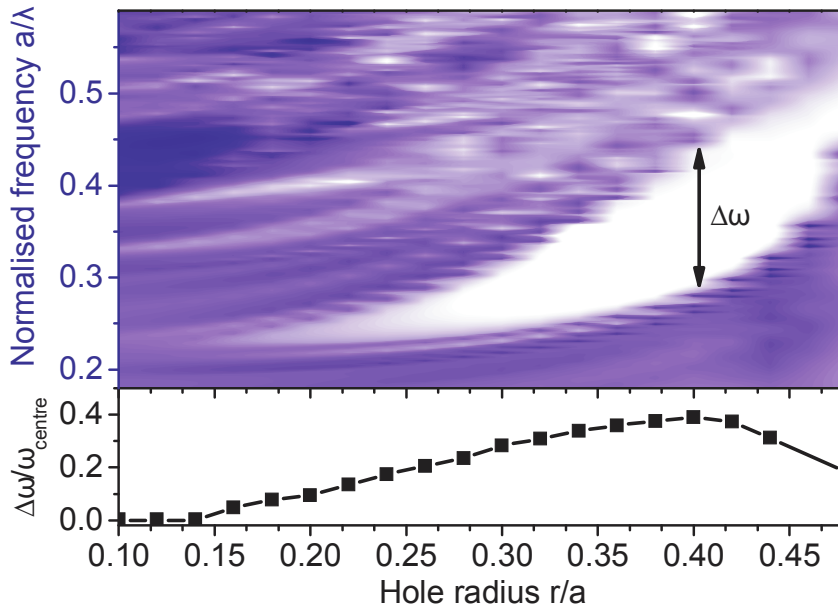


Figure 6.3: (a) Contour plot showing the simulated width of the band gap as the radius of the holes, r , in a hexagonal lattice photonic crystal is changed, with $d/a = 0.7$. White/blue regions indicate a low/high density of states. (b) Gap-midgap ratio of the photonic band gap ($\Delta\omega/\omega_{centre}$).

Figure 6.3 shows FDTD simulations of the width of the photonic band gap as the radius of the holes in a hexagonal lattice photonic crystal with $d/a = 0.7$ is changed. The widest band gap occurs for a value of $r/a = 0.4$. Since a wide

band gap leads to strong confinement [59], it is expected that the optimum value for the bulk hole radius will be close to this value.

6.3.2 Nearest neighbour hole radius

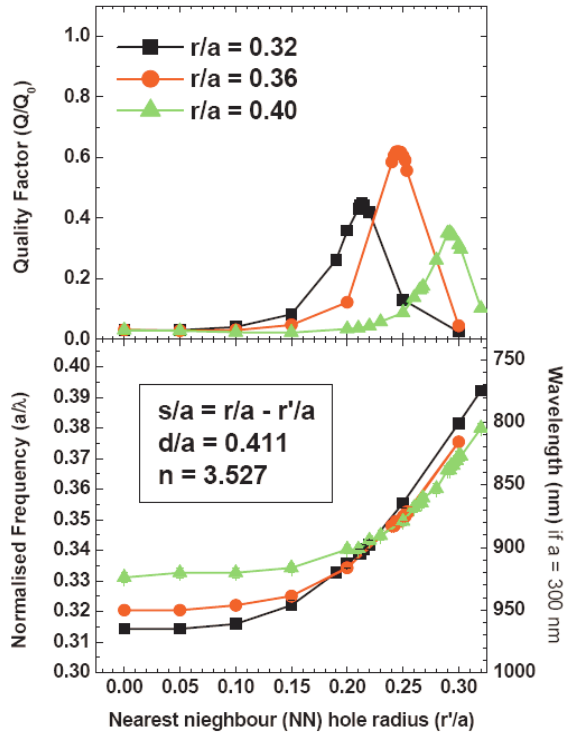


Figure 6.4: Simulated Q -factor (top) and mode frequency (bottom) of the monopole mode in a H1 cavity with $d/a = 0.411$ as the radius of the nearest neighbour holes, r' , is changed. The trends are shown for three different values of r/a . $Q_0 = 12500$ is the Q factor of the optimised cavity with $d = 0.65a$ calculated with 5 periods surrounding the defect. Courtesy of D. Gevaux.

The electric field profile of a mode in an unmodified H1 cavity is terminated abruptly by the photonic crystal, which gives rise to Fourier components of the mode which can couple to the light cone (see section 2.4.3). By reducing the radius of the six nearest neighbour holes and/or shifting their centres outwards,

the severity of the boundary is reduced so that fewer of the mode's Fourier components couple to the light cone, and higher Q -factors are achievable [2].

Figure 6.4 shows the simulated Q -factor of the H1 mode as the radius of the nearest neighbour holes is changed following the scheme shown in figure 6.1. The radius of the holes must be reduced by some degree for the monopole mode to be pulled down from the air band, as shown in figure 6.2. By further reducing the radius, the Q -factor of the mode is increased. The highest Q -factor is achieved for a value of $r'/a = 0.25$ and $r/a = 0.36$.

6.3.3 Slab height

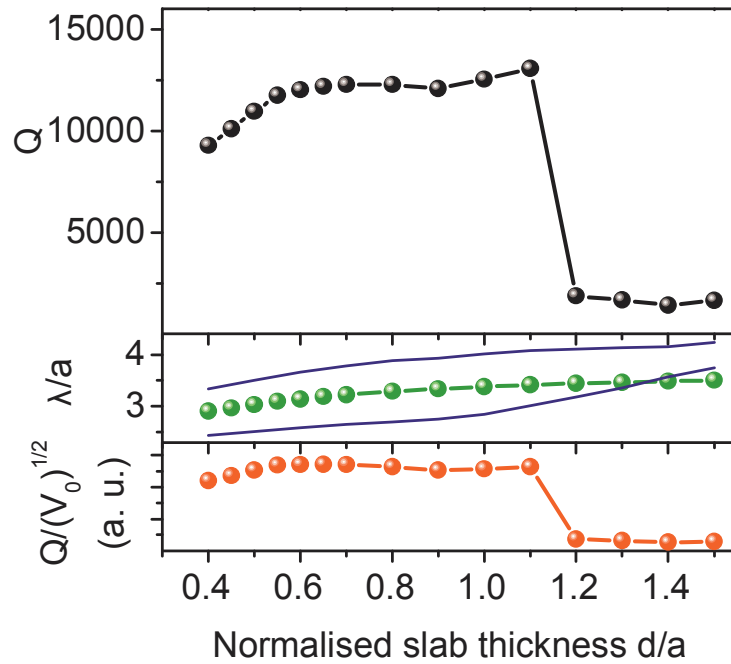


Figure 6.5: Simulated Q -factor (top) and mode wavelength (middle) of the monopole mode in a H1 cavity with $r/a = 0.36$, $r'/a = 0.25$, $n = 3.53$ and with 5 periods surrounding the defect, as the slab thickness, d , is changed. The blue lines in the centre panel indicate the edges of the photonic band gap. The bottom panel shows the ratio of $Q/\sqrt{V_0}$ which is a figure of merit for strong coupling.

The thickness of the slab also greatly affects the strength of the confinement (see figure 2.10). Figure 6.5 shows how the Q -factor of the monopole mode in a H1 cavity with $r/a = 0.36$ and $r'/a = 0.25$ changes as the thickness of the slab is modified. As the thickness of the slab increases, the resonant wavelength of the mode increases since the cavity becomes larger. The Q -factor increases until $d/a = 1.1$ at which point it drops off dramatically due to the decrease in the size of the photonic band gap causing the monopole to enter the air band [62, 132]. However, a higher value for the strong coupling figure of merit $Q/\sqrt{V_0}$ is achievable for a thinner slab of $d/a = 0.65$ since the mode volume is strongly dependent on the slab height.

6.3.4 Optimised cavity

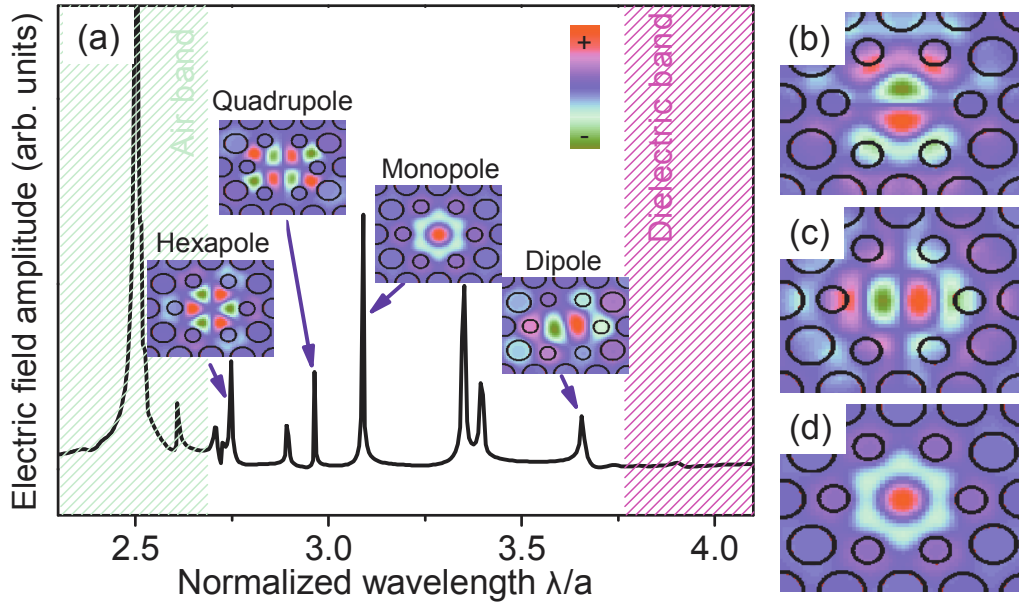


Figure 6.6: (a) Simulated mode structure of the optimised H1 cavity with $r/a = 0.36$, $r'/a = 0.25$ and $d/a = 0.65$. The structure is very similar to that in figure 6.2. The insets show the magnetic field profiles, H_z , for a selection of the modes. (b)-(d) E_x , E_y and H_z field distributions of the monopole mode.

Figure 6.6 shows the mode structure of the optimised H1 cavity with $r/a =$

0.36, $r'/a = 0.25$ and $d/a = 0.65$. A number of modes are present, as in figure 6.2. The insets show the magnetic field profiles, H_z , of a selection of the modes. The monopole in this optimised structure, has a Q -factor of $Q = 30000$ and a mode volume of $V_0 = 0.8(\lambda/n)^3$, calculated with 9 photonic crystal periods surrounding the defect. Its E_x , E_y and H_z field components are shown in figures 6.6 (b)-(d).

Both the E_x and E_y field profiles of the monopole have an odd mirror symmetry about the centre of the cavity. The size of the defect in x and y is around $a \sim \lambda/3$, so that the positive and negative components of the electric field will effectively cancel each other out in the far field. Therefore, the photons emitted from the cavity by coupling to the light cone (or scattering due to fabrication imperfections) will have no preferred polarisation [66].

6.4 Fabrication

The samples were fabricated as described in section 5.4. Based on the calculation in figure 6.6, the mode should appear at 900 nm, where the QDs emit, for a periodicity of around $a = 300$ nm. Therefore the slab thickness was set at $d = 0.65a \sim 200$ nm.

Since the fabrication is never perfect, a square array of cavities with varying parameters was made. On one axis the periodicity, a , was stepped to compensate for fabrication imperfection induced shifts in the monopole emission wavelength. On the other axis, the radius of the nearest neighbour holes, r' , was varied. This was done to compensate for any uneven etching rate of the different sized holes.

6.5 Optical characterisation

This section will detail PL measurements made on the fabricated structures to determine their quality.

6.5.1 Mode structure

By measuring cavities with varying values of r' , it was possible to see part of the cavity mode structure and to determine the location of the monopole mode.

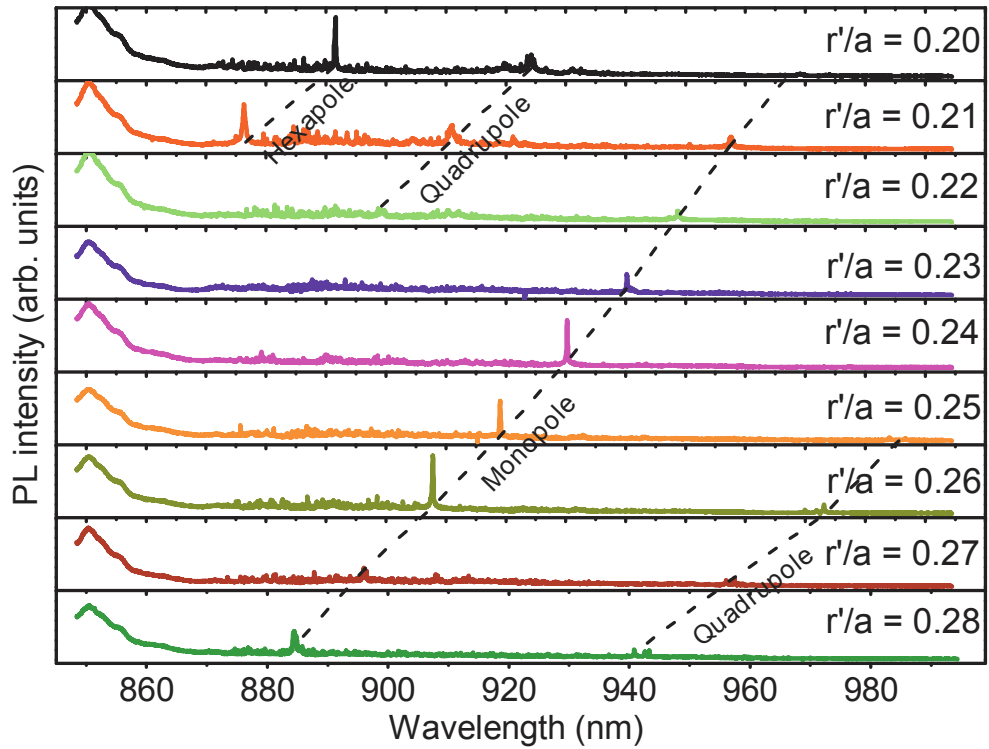


Figure 6.7: PL measured at 5 K of from several H1 cavities with $r/a = 0.36$, $d = 200$ nm, $a = 300$ nm and 5 photonic crystal periods surrounding the defect. Each spectrum is from a different cavity with varying r' as labeled. The black dashed lines are guides to the eye to show each of the modes shifting in wavelength between each cavity.

Figure 6.7 shows PL from a number of different H1 cavities with $r/a = 0.36$, $a = 300$ nm, $d = 200$ nm and varying values of r' as labeled. A number of modes appear in the spectra, which have been identified based on the wavelengths at which they appear. Each mode shifts to longer wavelengths as the radius of the nearest neighbour holes is reduced, as expected.

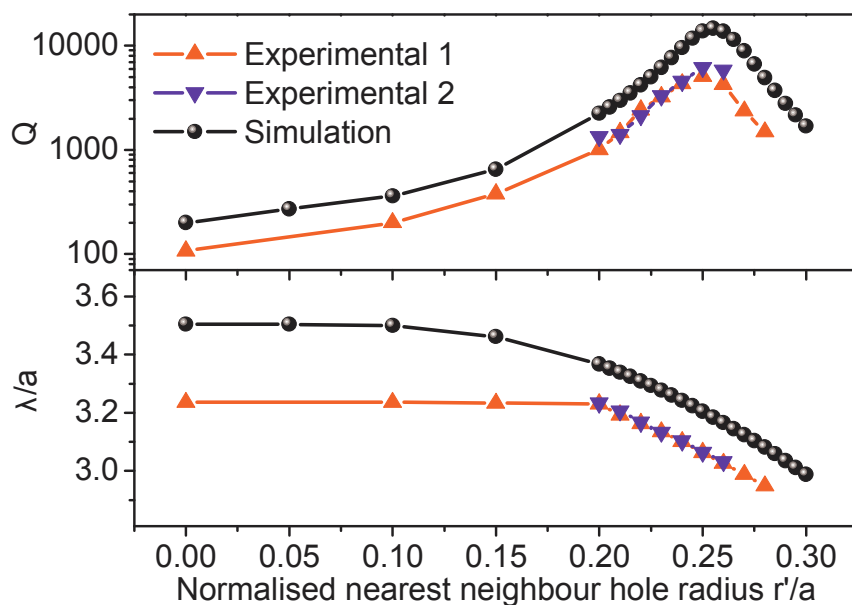


Figure 6.8: Q -factors (top panel) and normalised wavelengths (bottom panel) of the monopole mode as the nearest neighbour hole radius is changed. The red symbols show data extracted from the data in figure 6.7. The blue symbols show a similar set of data from a second array of cavities on the same chip. The black symbols show the calculated theoretical values.

Figure 6.8 show comparisons of the theoretical and experimentally measured Q -factor and emission wavelength of the monopole mode. An excellent agreement between the trends of the experimental data and the simulated values can be seen. The experimental Q -factors are consistently lower than the theoretical values due to the inevitable fabrication imperfections. The peaks in the two curves do not exactly match, owing to the uneven etching rates of the different sized holes.

Figure 6.9 shows PL from the monopole mode of a number of nominally identical H1 cavities from two different chips with $r/a = 0.36$ and $r'/a = 0.25$.

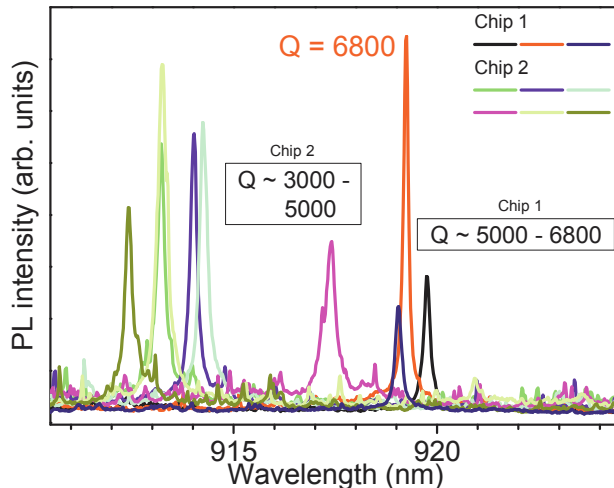


Figure 6.9: PL measured at 5 K of from the monopole mode from several H1 cavities with nominally identical parameters: $r/a = 0.36$, $r'/a = 0.25$, $d = 200$ nm and $a = 300$ nm.

The emission wavelengths are remarkably consistent between the cavities on each chip, typically within a few nanometres. The variation between different chips is somewhat larger and reflects the inconsistencies in the processing conditions from chip to chip. The cavities measured here do not represent the optimal processing as discussed in section 5.4.

6.6 Weak coupling

In the weak coupling regime, the spontaneous emission rate of a QD transition on resonance with a mode will be enhanced according to equation 2.10. As the temperature of a cavity is increased above 5 K, the modes redshift due to the change in the refractive index of GaAs, whereas lines from QDs redshift at a faster rate, following the change in the GaAs band gap. It is therefore possible to tune QD lines onto resonance with modes which lie close by at higher wavelengths, by increasing the temperature of the sample [68]. This process effectively maximises the spectral overlap term in equation 2.10.

The spatial overlap term, however, cannot be controlled since the QDs are

randomly positioned throughout the wafer. It is therefore necessary to fabricate a large number of cavities and to search through them to find one with a suitably positioned QD with a wavelength close to the mode. The measured Purcell enhancement is usually limited by imperfect spatial alignment between the QD dipole and the electric field of the mode.

Figure 6.10 shows PL from the monopole mode of a H1 cavity with a weakly coupled QD. As the temperature of the sample is increased, the line is tuned onto and then off of resonance with the mode. As the QD line shifts onto resonance, its intensity is enhanced due to the Purcell effect. Previous studies have directly shown that the spontaneous emission rate of QD transitions are enhanced in this way [46].

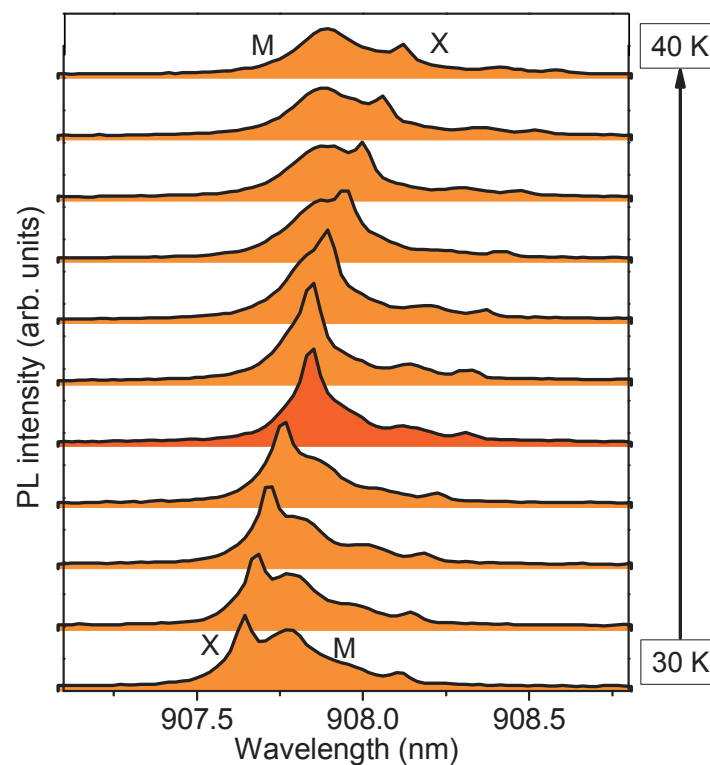


Figure 6.10: PL from a monopole mode with $Q = 4300$ of a H1 cavity with a low density of QDs at the centre of the slab, as the temperature is increased from 30 K to 40 K. The QD exciton line labeled X shifts onto, and then off of, resonance with the mode labeled M.

6.7 Strong coupling

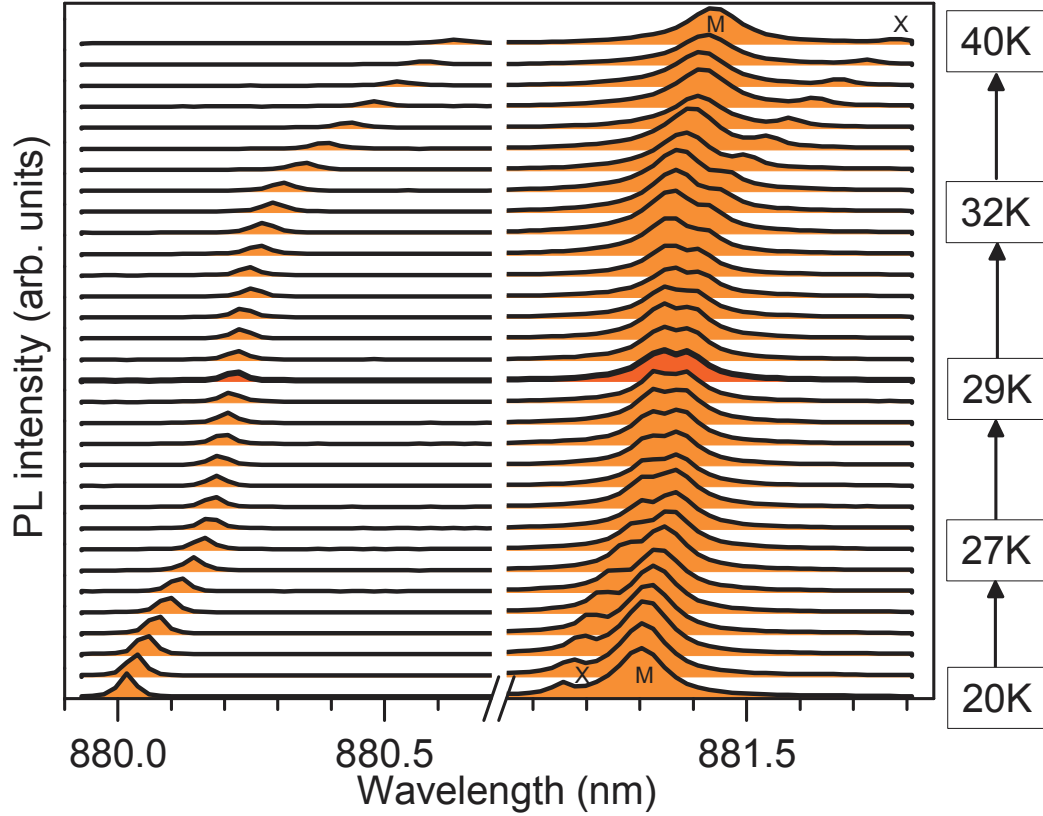


Figure 6.11: PL of from the monopole mode of a H1 cavity with $Q = 8500$ (labeled M) as the temperature is increased from 20 K to 40 K. The excitonic line labeled X comes exactly onto resonance with the mode at 29 K, at which point two peaks persist in the spectrum. The temperature step between each graph is smaller between 27 K and 32 K than elsewhere to emphasize the splitting at resonance.

After extensive optimisation of the processing, as described in section 5.4, it was possible to achieve very high Q -factors of up to 9900 for the monopole mode. Figure 6.11 shows PL from the monopole mode of a H1 cavity with $Q = 8500$ (labeled M) as the temperature of the sample was varied in unequal steps between 20 K and 40 K. The two other lines in the spectra (at 881.15 nm and 880.0 nm at 20 K) are from QD transitions. As the temperature of the sample was increased

above 20 K, the QD line labeled X was tuned onto resonance with the mode. In all the measurements, including when the line was exactly on resonance with the mode at 29 K, two peaks remained in the spectrum. As the temperature was increased beyond 29 K, the QD line detuned away from the mode.

There is a clear anti-crossing in the peak energies of the exciton and the mode. This behaviour can be seen more clearly in figure 6.12 in which the energies of the lines are plotted as a function of their energy detuning. The blue lines in the figure are the expected peak energies of the QD and mode in the weakly coupled case. This anti-crossing is a clear signature of the strong coupling regime as described in section 2.3.3 [108, 113, 149].

Figure 6.12 also shows how the behaviour of the linewidths and integrated PL intensities of the two lines as a function of their detuning. The linewidths of the two lines approach each other and converge to the same value when they are tuned onto resonance. As the QD is tuned away, the linewidths gradually approach their original values. The integrated intensities of the two lines show similar behaviour. These observations confirm the existence of strong coupling [112].

The intensity of the mode was much higher than that of the QD line when detuned. This suggests that other QD lines were contributing to the mode emission, even though they were not spectrally coupled [8, 57, 97, 145, 147].

Figure 6.13 (a) shows a high resolution PL spectrum from the strongly coupled QD/cavity at 29 K. At this point, the splitting between the two polariton peaks is at its minimum. By fitting two Lorentzian lines to the spectrum, a vacuum Rabi splitting (VRS) of $\Delta U^{vac} = 115 \mu\text{eV}$ was extracted. Figure 6.13 (b) shows a similar plot for a second strongly coupled QD/cavity system, with a larger VRS of $\Delta U^{vac} = 141 \mu\text{eV}$.

This value for the VRS corresponds to a QD-cavity coupling parameter of $\hbar g = 70 \mu\text{eV}$, which exceeds the strong coupling condition $g/\kappa = 0.27 > 1/4$ (see equation 2.15). The maximum possible QD-coupling parameter in the case of a perfectly positioned QD was calculated from equation 2.5 to be around $135 \mu\text{eV}$. The difference in the measured value is most likely due to the non-ideal position of the QD, away from the electric field maximum of the cavity mode.

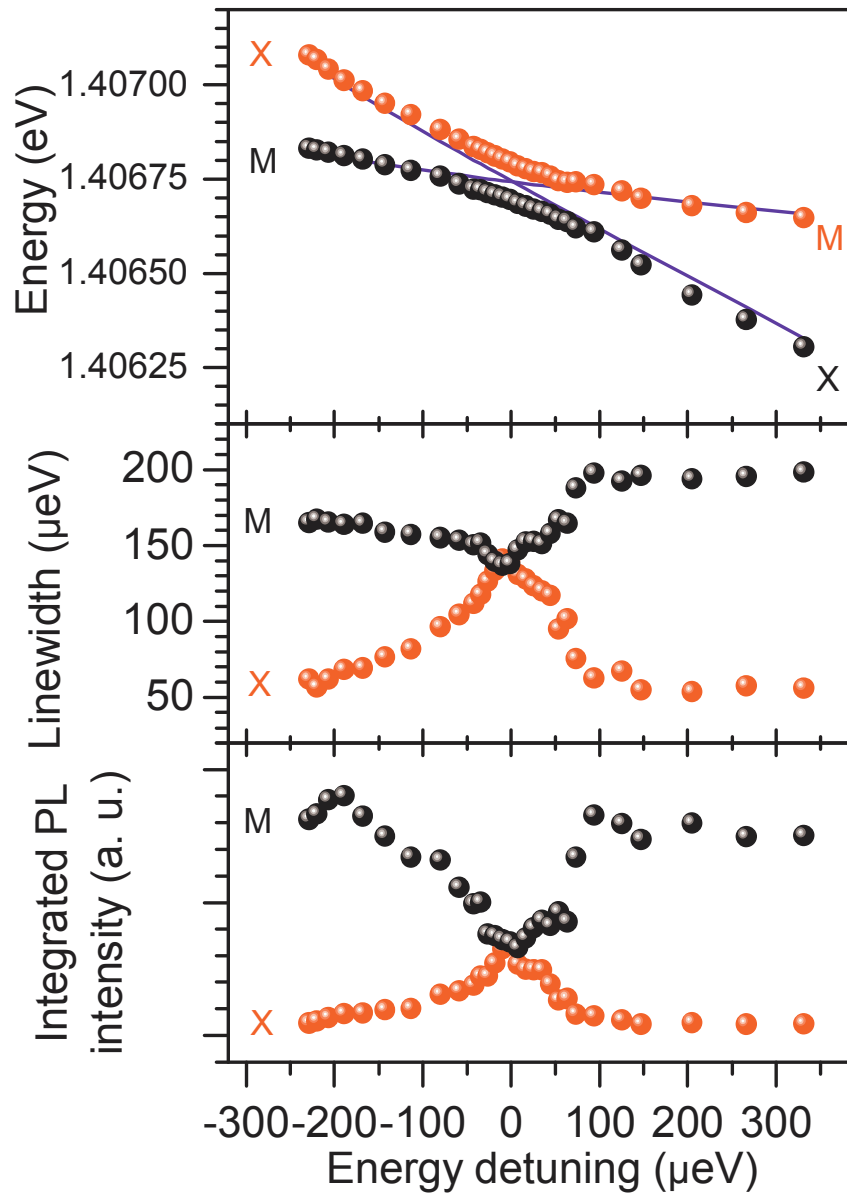


Figure 6.12: Peak energies of the mode and QD line (labeled M and X in figure 6.11) as they are tuned around resonance (top panel). A clear anti-crossing occurs between their peak energies. The centre and bottom panels show the behaviour of the linewidths and integrated intensities of the lines respectively.

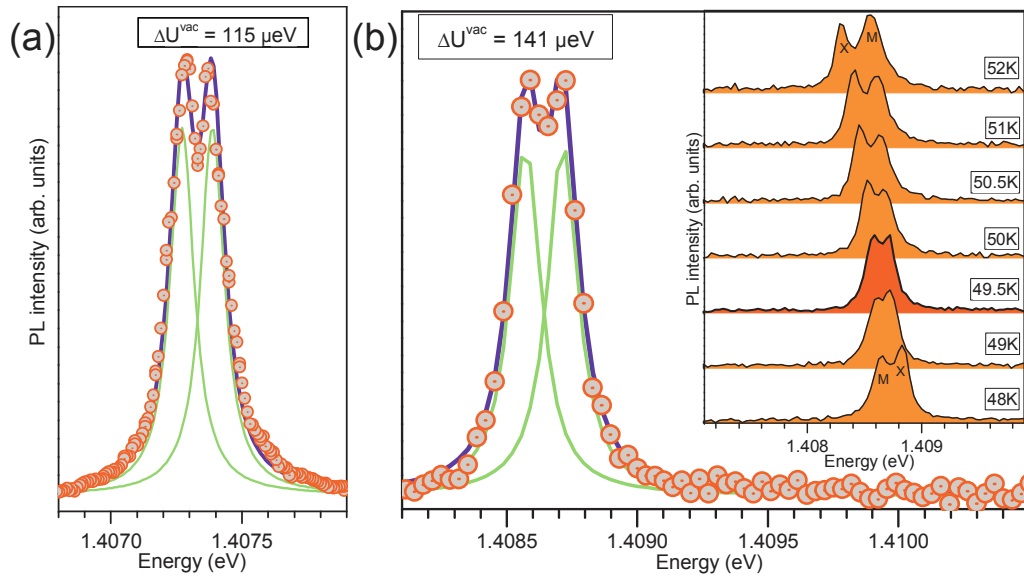


Figure 6.13: (a) PL from the strongly coupled QD/cavity in figure 6.11 when on resonance at 29K, taken by scanning the spectrometer and detecting with an APD (circles). The blue line shows a double Lorentzian fit to the data, with each Lorentzian shown in green. A splitting of $\Delta U^{vac} = 115 \mu\text{eV}$ is extracted from the fit. (b) As (a) but for a second strongly coupled QD/cavity with a larger splitting on resonance of $\Delta U^{vac} = 141 \mu\text{eV}$, and taken with the regular μPL setup. The inset shows PL from the QD/cavity at various temperatures close to resonance.

These results compare favourably to those recently presented in reference [103], in which strong coupling was achieved in a H1 cavity for the first time, using the dipole mode and an InAs QD. Despite having a theoretically higher Q of ~ 50000 , a smaller mode volume of $V_0 = 0.43(\lambda/n)^3$ and a higher operating wavelength of ~ 970 nm, the highest measured Q reported was 7300. This lead to a VRS of $124 \mu\text{eV}$.

6.8 Polarisation dependence

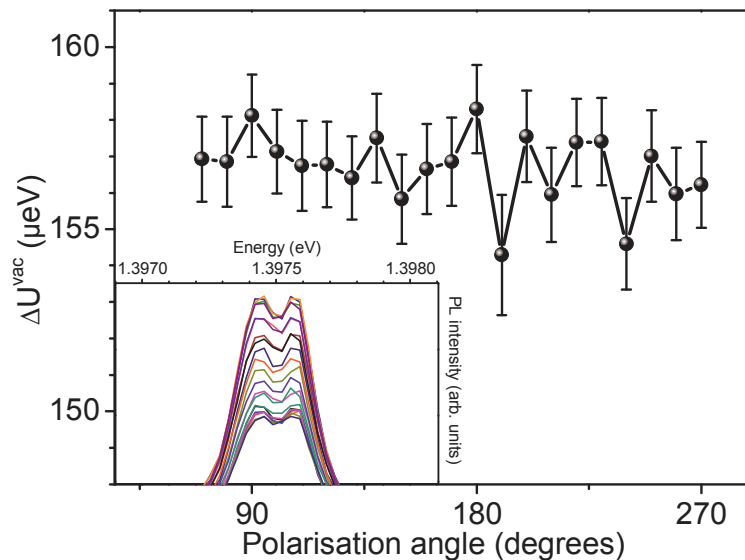


Figure 6.14: Polarisation dependence of the splitting of a strongly coupled QD/cavity. The average value is $\Delta U^{vac} = 157 \mu\text{eV}$. The random error results from errors in fitting the peak energies. The inset shows the raw data, the change in intensity is due to the in-built polarising nature of the measurement setup.

Figure 6.14 shows the polarisation dependence of the VRS of a third strongly coupled QD/cavity. The splitting persists for all polarisations with no angle-dependent variation in its magnitude. This is due to the unpolarised nature of the far-field of the monopole mode emission. A photon emitted from a QD may have some polarisation depending on the orientation of the QD axes, which will

be closely aligned to the direction of local electric field of the mode for strong coupling. However, the photon will take the electric field pattern of the whole mode before it leaks from the cavity. The emitted photons will therefore have no preferred polarisation.

6.9 Summary and outlook

The Q -factor of the monopole mode in a H1 cavity has been optimised for strong coupling, principally by modifying the six holes surrounding the defect. Strong coupling between a single InAs QD and the monopole mode has been observed for the first time. The VRS persists for all linear polarisations due to the unpolarised nature of the mode's far field emission pattern. This result expands on previous work in solid state cavity quantum electrodynamics and is an important step in the development of quantum information devices.

Several strongly coupled QD/cavities were found, demonstrating the usefulness of the monopole mode for strong coupling with randomly positioned dots, due to the low number of nodes in the electric field profile. The wavelength of the first strongly coupled QD/cavity was ~ 880 nm, where the neutral exciton fine structure splitting is zero or very close to zero [130]. This result leads the way towards the realisation of a strongly coupled entangled photon pair source.

Chapter 7

Unidirectional photonic crystal waveguides

7.1 Overview

This chapter will describe experiments carried out on unidirectional photonic crystal waveguides with the goal of working towards realising an in-plane quantum light source.

As explained in section 2.3, by coupling a QD transition to an optical cavity, it is possible to enhance its spontaneous emission rate and to allow efficient extraction of the light through the Purcell effect [111]. Large Purcell enhancements have been observed in micropillars [45], microdisks [68] and photonic crystal cavities [10, 29, 34, 46, 72, 82], in some cases entering the strong-coupling regime [50, 108, 113, 149] (as in chapter 6). However in all of these cavity architectures, the bulk of the emission is directed out of the plane of the semiconductor chip. Future photonic integrated circuits would benefit from in-plane quantum light sources [109].

Two-dimensional photonic crystal slab cavities are attractive because of their high Q s and small volumes. Light is confined in the plane with a photonic band gap and in the vertical direction by total internal reflection at semiconductor-air interfaces. However, to achieve high Q -factors it is necessary to design the cavity so that out-of-plane emission is suppressed [2], which is incompatible with high extraction efficiencies in the vertical direction. Nevertheless, recent theoretical

7.2 Photonic crystal waveguide mode structure

work has shown that large Purcell factors and high in-plane extraction efficiencies are achievable for QDs coupled to photonic crystal waveguides (PCWGs) [54].

PCWGs can be made from 2D photonic crystal slabs by removing a line of air holes [30]. These waveguides can support a number of guided modes which are confined in the plane by the photonic band gap and in the vertical direction by total internal reflection. The modes have flat regions in their dispersion relations, so that their group velocities go to zero for certain frequencies [9, 71]. In particular, at the edge of the Brillouin zone ($k_x = \pi/a$) light is coherently backscattered by the periodic crystal, and a standing wave forms. Just away from the zone boundary is the true slow-light regime, where light propagates slowly through the waveguide. Other standing wave resonances can occur, for example at the Γ point ($k_x = 0$) if it lies inside the photonic band gap. Large Purcell factors can be achieved due to the high local photon density of states associated with these slow-light resonances.

A recent theoretical proposal [91] suggested a design to utilize the properties of PCWGs to create an efficient in-plane quantum light source. A short waveguide can provide a large Purcell factor, while minimizing the detrimental effects due to fabrication imperfections [55] and easing the coupling of an individual QD. Furthermore, for a unidirectional PCWG (i.e. a PCWG with one end terminated by a photonic crystal mirror and at the other end by a semiconductor-air interface), the majority of the emission can be directed in one in-plane direction. PCWGs offer other advantages such as broadband large β -factors associated with the width of the mode beneath the light-line [81, 87, 90, 102], however the work presented in this chapter is concerned only with the Purcell enhancements due to the slow-light resonances [136].

7.2 Photonic crystal waveguide mode structure

Figure 7.1 shows a schematic diagram of a unidirectional PCWG, formed by a line of missing air holes along the Γ - K direction of a triangular lattice photonic crystal pattern. One end of the waveguide is terminated by a photonic crystal mirror, the other end by a semiconductor-air interface. The x - y - and z -directions are

7.2 Photonic crystal waveguide mode structure

defined as parallel to the length of the waveguide, perpendicular to the waveguide in the plane of the slab, and perpendicular to the plane of the slab, respectively.

The results of FDTD simulations of the structure with hole radii $r/a = 0.3$, slab thickness $d/a = 0.7$, waveguide width $w/a = 1$ and length $l/a = 12$ (parameters defined in figure 7.1) are shown in figure 7.2(a). The calculation was carried out with a single x - or y -polarised dipole source placed at the centre of the waveguide.

There are two main high- Q modes, as in [91], a y -polarised mode (i.e. electric field orientated in the y -direction, see section 7.3.4) labelled M1, and an x -polarised mode labelled M2. These are the standing waves formed at the Brillouin zone boundary of the two orthogonally polarised waveguide modes present inside the photonic band gap [102]. The other features in the y -polarised spectrum are due to Fabry-Perot like resonances between the semiconductor-air interface and the back photonic crystal mirror. The x -polarised spectrum includes a number of lower Q features, associated with slow-light resonances of the x -polarised waveguide mode which are above the light-line [131].

The identification of Fabry-Perot modes alongside the slow-light resonances was confirmed by repeating the calculation with the waveguide terminated at each end by PML absorbing boundaries, as shown in figure 7.2(b). In this case, the Fabry-Perot modes disappear from the spectrum since they are no longer confined along the length of the waveguide. Furthermore, the spacing between the Fabry-Perot modes matches well with the free spectral range for a one-dimensional cavity of the same length, and mode profile calculations show that each mode has one node more or less than the modes next to it in the spectrum, as expected for Fabry-Perot modes.

The slow-light resonances, on the other hand, are confined by Bragg reflection along the length of the waveguide, and therefore persist in the spectrum when the waveguide is terminated by PML absorbing boundaries. The work presented here focuses on the y -polarised resonance of the unidirectional PCWG, M1, which is expected to have a large in-plane collection efficiency [91].

7.2 Photonic crystal waveguide mode structure

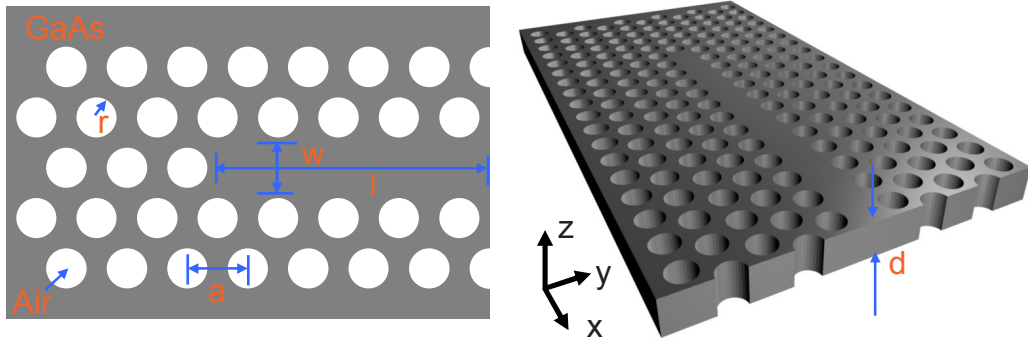


Figure 7.1: Schematic diagram of a unidirectional photonic crystal waveguide. The relevant parameters are labeled. The coordinates are defined with reference to the figure on the right.

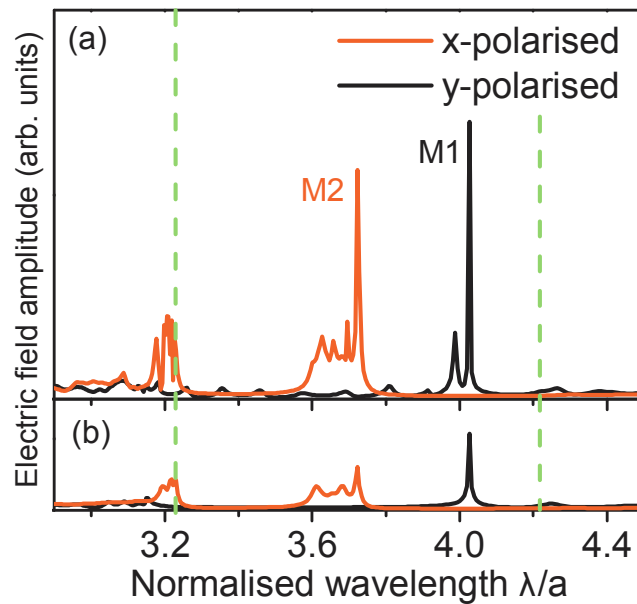


Figure 7.2: (a) FDTD simulation of the mode profile of a W1 (i.e. $w/a = 1$) unidirectional PCWG with $r = 0.3a$, $d = 0.7a$, $l = 12a$ and $n = 3.53$. The calculation is done with a single x - or y -polarised dipole source positioned at the centre of the waveguide. (b) Same as (a) except the PCWG is terminated by PML absorbing boundaries at each end. The dashed green lines indicate the positions of the photonic band gap edges.

7.3 Design and optimisation

In the same way as for H1 cavities, there are a number of parameters that can be changed to optimise the Q -factor of the slow-light resonances in a unidirectional PCWG [83]. These are summarised in figure 7.1 and include the bulk hole radius, r , the width of the slab, d , the length of the PCWG, l , the width of the waveguide, w , the position of the cleaved edge and the properties of the nearest neighbour holes. Using the original theoretical proposals of the device [91] as a starting point, this section details work undertaken to optimise the Q -factor of M1.

7.3.1 Basic parameters

In reference [89], the effect of the length of a unidirectional PCWG on the maximum Purcell factor of the mode M1 was theoretically investigated. For a W1 waveguide with $r/a = 0.275$ and $d/a = 0.5$, the maximum Purcell factor was found to increase with increasing length until it saturated at around $l/a = 20$ at $F_P = 252$. Since the confinement is due to Bragg reflection along the length of the waveguide, including more periods of photonic crystal should increase the confinement. However, this also has the effect of decreasing the in-plane collection efficiency. In light of this result, a trade-off value of $l/a = 12$ was chosen for this work.

In the same study, it was found that terminating the waveguide between nearest neighbour holes was slightly advantageous over terminating it through a nearest neighbour hole. Therefore, all the calculations and fabricated samples were terminated between the nearest neighbour holes, as in figure 7.1.

For simplicity, the width of the waveguide has been fixed at $w/a = 1$ and the parameters of the nearest neighbour holes have not been modified throughout this work. There may well be further scope to optimise the modes by modifying these parameters [83], however the Q -factors of the design described in the rest of this chapter are high enough so that the measured values are effectively determined by fabrication imperfections.

7.3.2 Hole radius

The first simulations carried out investigated the effect of changing the radii of the holes, r . The original theoretical proposal showed that for a 10 unit cell long PCWG with a hole radius of $r/a = 0.275$ and $d/a = 0.5$, a Q -factor of around 1000 was possible for M1, corresponding to a maximum Purcell factor of $F_P = 59$ [91]. Simulations carried out in this work showed that by simply increasing the radius of the holes, a dramatic increase in the Q -factor is possible.

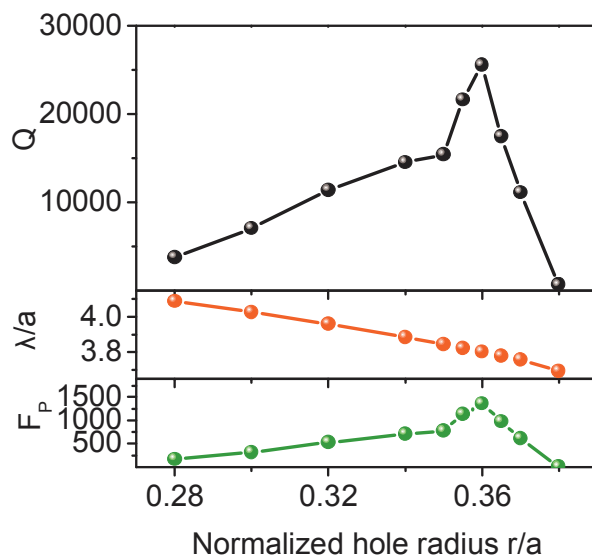


Figure 7.3: Results of FDTD simulations for the y -polarised mode M1 of a W1 unidirectional photonic crystal waveguide with $d/a = 0.7$, $l/a = 12$ and $n = 3.53$, as the radius of the holes, r/a , is changed.

The simulations were carried out with a W1 unidirectional PCWG with a slab thickness of $d/a = 0.7$, with five periods of the crystal on all sides, and with a length of $l/a = 12$. The radius of the holes was varied and the normalised wavelength, the Q -factor and the mode volume were simulated. The maximum Purcell factor was calculated from these numbers. Figure 7.3 shows the results. As the radius is increased, the mode's wavelength decreases as the size of the waveguide is decreased. It was found that M1 has the largest Q -factor for $r/a =$

0.36, with $Q = 25500$. The mode volume was calculated to be $V_0 \sim 1.4(\lambda/n)^3$, giving a maximum Purcell factor of $F_P = 1360$.

7.3.3 Slab height

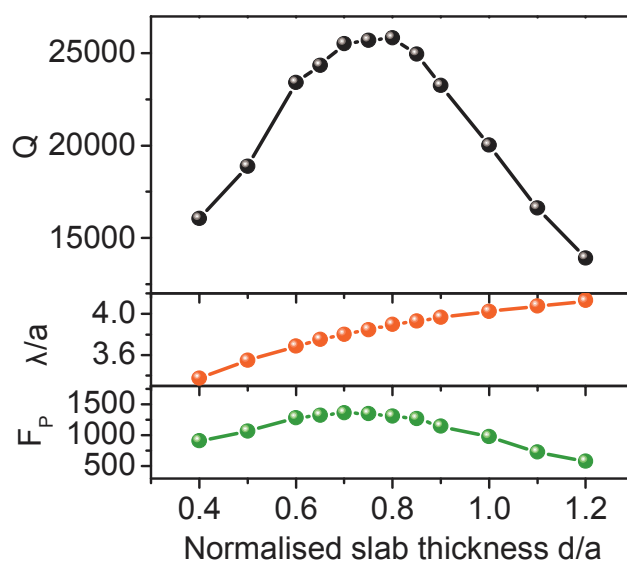


Figure 7.4: Results of FDTD simulations for the y -polarised mode M1 of a W1 unidirectional photonic crystal waveguide with $r/a = 0.36$, $l/a = 12$ and $n = 3.53$, as the height of the slab, d/a , is changed.

A similar set of simulations were run to optimise the slab height, with the results shown in figure 7.4. As the slab height is increased, the wavelength of the mode increases as the size of the waveguide increases. The Q -factor was found to increase slightly to $Q = 25800$ for a slab height of $d/a = 0.8$. However, the maximum Purcell factor was slightly lower for this value, at $F_P = 1310$, due to the mode volume increasing with the slab height. In fact, the highest Purcell factor was calculated to be $F_P = 1360$ at $d/a = 0.7$, as before.

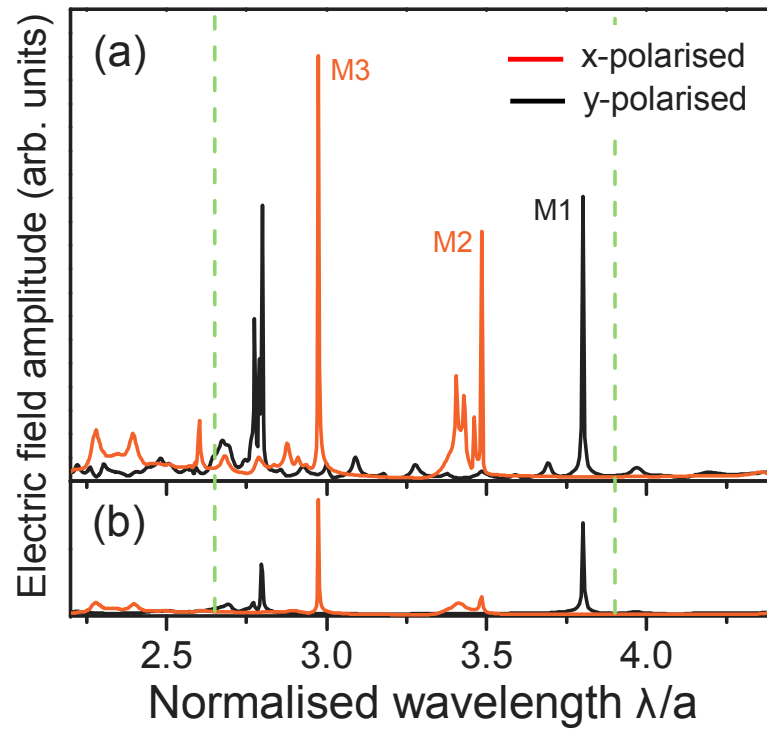


Figure 7.5: (a) FDTD simulation of the mode structure of a PCWG with $r/a = 0.36$ and $d/a = 0.7$, calculated with a single x - or y -polarised dipole placed at the centre of the structure and using 5 photonic crystal periods on each side. The dashed green lines indicate the location of the photonic band gap edges. (b) FDTD simulation of an equivalent PCWG without mirrors at either end.

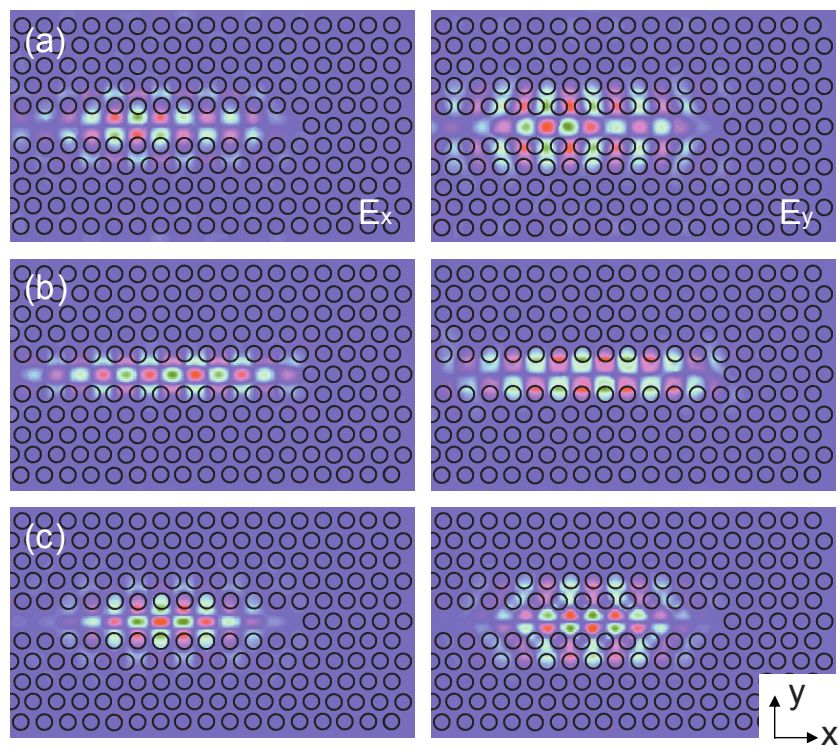


Figure 7.6: E_x and E_y electric field profiles at the centre of the slab for M1 (a), M2 (b) and M3 (c).

7.3.4 Optimised waveguide

Figure 7.5 (a) shows the calculated mode structure of the optimised waveguide with $r/a = 0.36$ and $d/a = 0.7$. The larger value of r/a results in a wider band gap than for $r/a = 0.3$ as in figure 7.2, so that some modes which were in the air band appear in the band gap (see figure 6.3). The slow-light resonance M1 appears close to the edge of the photonic band gap, with a calculated Q of 25500. Its electric field profile is shown in figure 7.6 (a). The E_x electric field profile has odd reflection symmetry along $y = 0$, hence the positive and negative components will cancel each other in the far field emission [65]. The E_y profile however, has an even mirror symmetry along $y = 0$ and the waveguide is asymmetric in the x -direction, so that the far field of the mode emission will be y -polarised. A slow-light resonance from a second y -polarised waveguide mode [83] appears in the spectrum at $\lambda/a \approx 2.7$, with $Q = 2200$. The other features in the y -polarised dipole spectrum are Fabry-Perot like resonances between the GaAs-air interface and the back photonic crystal mirror, all with $Q < 200$.

The equivalent calculation for x -polarised modes shows M2 further inside the band gap at $\lambda/a \approx 3.5$ with $Q = 4900$. The closeby features all have $Q < 1700$. The electric field profile of M2, as shown in figure 7.6 (b), confirms that its far-field is x -polarised. A second x -polarised feature M3, originating from another waveguide mode [83], appears at $\lambda/a \approx 3.0$, which will be discussed later. Its electric field profile is shown in figure 7.6 (c).

7.4 Fabrication

The process of fabricating PCWGs is almost identical to the H1 process, with the addition of a cleaving step to allow in-plane measurement. The sample design was developed to make this step possible. A large feature was positioned between two opposing unidirectional waveguides to form the semiconductor-air interface at one end of the waveguide, as shown in figure 7.7 (a). The sample was cleaved through this feature, leaving a waveguide on each piece of the cleaved wafer. An SEM image of a completed device is shown in figure 7.7 (b).

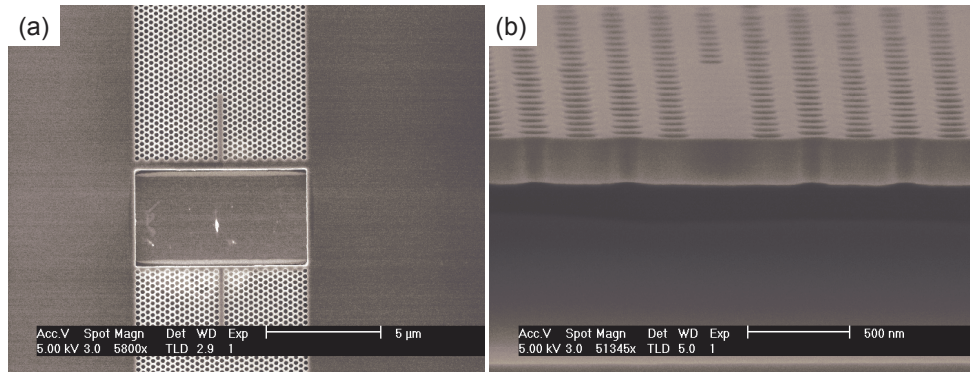


Figure 7.7: SEM images of (a) the mask design showing the large features between two opposing unidirectional photonic crystal waveguides, (b) a close up of a completed device. The waveguide is terminated between nearest neighbour holes.

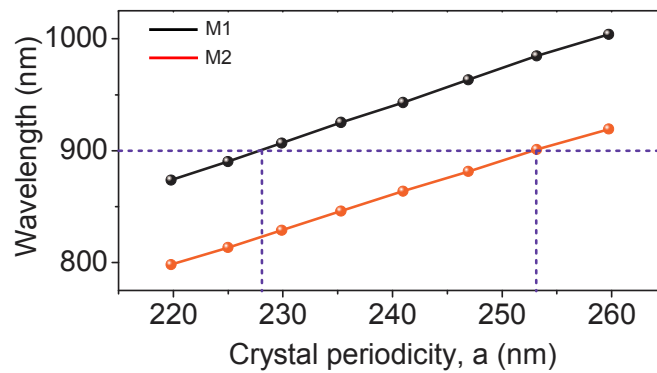


Figure 7.8: Calculated wavelengths of the modes M1 and M2 versus the periodicity, a , with a slab height of $d = 200$ nm and a GaAs refractive index of $n = 3.53$.

Experimentally, any of the modes can be accessed by choosing a suitable value of the crystal periodicity, a , so that the mode appears at around 900 nm, the wavelength at which the InAs QDs emit. Figure 7.8 shows the calculated wavelengths of M1 and M2 versus the periodicity for a slab height of $d = 200$ nm. According to the calculations, the x -polarised M2 should appear at 900 nm for a waveguide with $a = 253$ nm, and the y -polarised M1 should appear at $a = 228$ nm.

7.5 Optical characterisation

Figure 7.9 shows polarisation-resolved PL from four different waveguides containing a low density of QDs at the centre of the slab, with periodicities of $a = 230$ nm (figures 7.9 (a) and (b)) and $a = 255$ nm (figures 7.9 (c) and (d)). Figures 7.9 (a) and (c) are measured in-plane, whereas figures 7.9 (b) and (d) are measured in the out-of-plane setup as indicated. Modes were identified in each of the spectra and are indicated with green fitted lines. As the temperature of the device is increased, the modes redshift due to the change in the refractive index of GaAs, whereas the other sharper lines from QDs redshift at a faster rate, following the change in the GaAs band gap [68].

The modes can be unambiguously identified as M1 and M2 based on the values of a for which they appear, i.e. figures 7.9 (a) and (b) show M1 and figures 7.9 (c) and (d) show M2. The mode wavelengths are not exactly as calculated and are different for each sample because of the inevitable random fabrication imperfections.

Typically M2 was measured to have $Q = 2700$, around a factor of 2 lower than the calculated value. M1 typically had $Q = 1200$, much lower than the calculation of 25500. These values are limited by fabrication imperfections in the structures. The Q -factor of M1 is smaller because the imperfections are more significant in the waveguide with smaller features.

The mode M2 in figure 7.9 (d) is strongly x -polarised as expected. When measuring in-plane, the y - and z -polarised components of the field are sampled. Since E_z is not confined by two-dimensional slab photonic crystals, only E_y is relevant in this case. The emission of M2 is expected to be unpolarised because

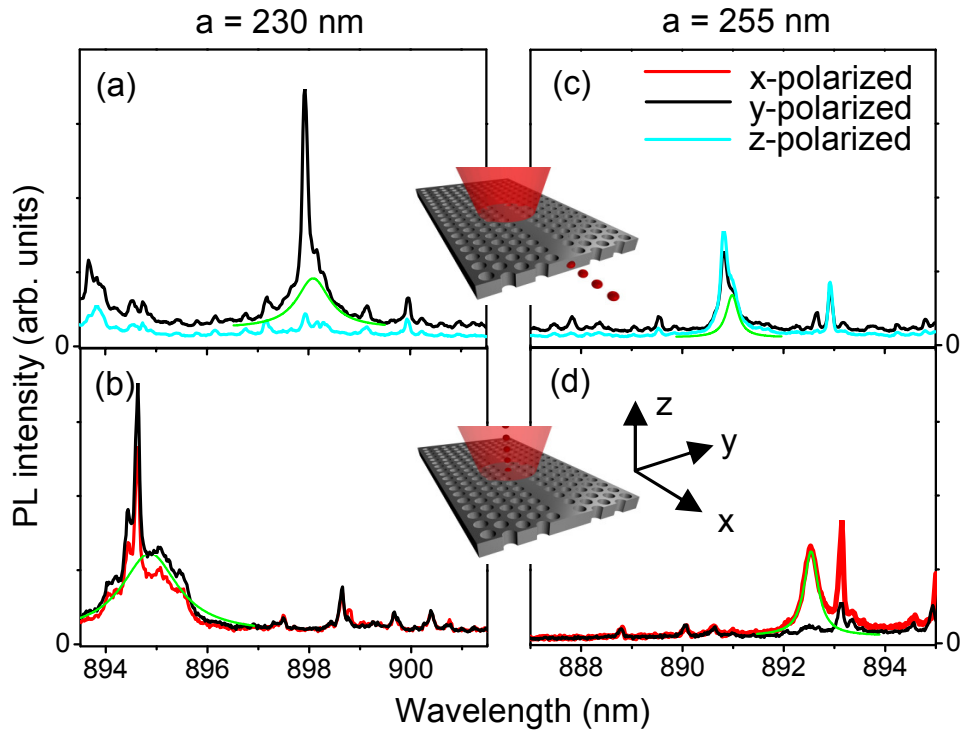


Figure 7.9: PL from four separate PCWG structures measured at 45 K, corrected for the polarisation of the measuring setup. The sharp lines are due to QD transitions, the broader features are the modes as indicated by the fitted green lines. These examples are chosen as they all have an excitonic transition on or near the relevant mode at 45 K. The insets show the two measurement setups: exciting from the top and collecting from the side (top inset) or from the top (bottom inset). (a) PCWG with $a = 230$ nm measured in-plane. (b) PCWG with $a = 230$ nm measured out-of-plane. (c) PCWG with $a = 255$ nm measured in-plane. (d) PCWG with $a = 255$ nm measured out-of-plane.

of the odd reflection symmetry of its E_y profile along $y = 0$. This is shown in figure 7.9 (c).

The in-plane PL of the mode M1 is strongly y -polarised as expected from the even symmetry of its E_y profile, and shown in figure 7.9 (a). The out-of-plane PL from M1 in figure 7.9 (b) is however, only weakly y -polarised. The presence of x -polarised photons implies that the E_x field components are not cancelling in the far-field as expected. This is attributed to the large fabrication imperfections in the $a = 230$ nm structure as evidenced by the low Q -factor, since the E_x field profile has anti-nodes close to the air hole walls.

7.6 Purcell effect

This section focuses on in-plane measurements of M1 in the PCWG shown in figure 7.9 (a). PL from the same device at 5 K is shown in figure 7.10 (a). As the temperature of the device is increased, each sharp QD line can be brought onto resonance with the mode (highlighted by the green line). The line labeled 2X is identified by power dependence measurements as biexcitonic, and lines X^a , X^b and X^c are identified as excitonic.

Time-resolved measurements of 2X and X^a at 5 K, and when they are on resonance with the mode are shown in figures 7.10 (b) and (c). Double exponentials were fitted to the curves to extract the lifetimes. This double exponential decay is typical of the studied samples, the long lifetime component arises from refilling by another state [123]. When the lines are on resonance, the lifetime of the transition is enhanced due to the Purcell effect. In contrast, over a similar temperature range, the lifetime of line X^c increases as it detunes away from the mode and is suppressed (see figure 7.10 (d)).

Lines 2X and X^a show Purcell enhancements of 1.9 and 2.7 respectively, suggesting that they originate from different QDs. The maximum calculated Purcell factor for a QD coupled to this mode with $Q = 1200$ is $F_P = 65$. The difference with the measured values is most likely due to a mismatch in the position and orientation of the QDs with respect to the maximum in the electric field of the mode profiles. In the future, the inclusion of prepositioned QDs could lead to higher Purcell enhancements [7, 125].

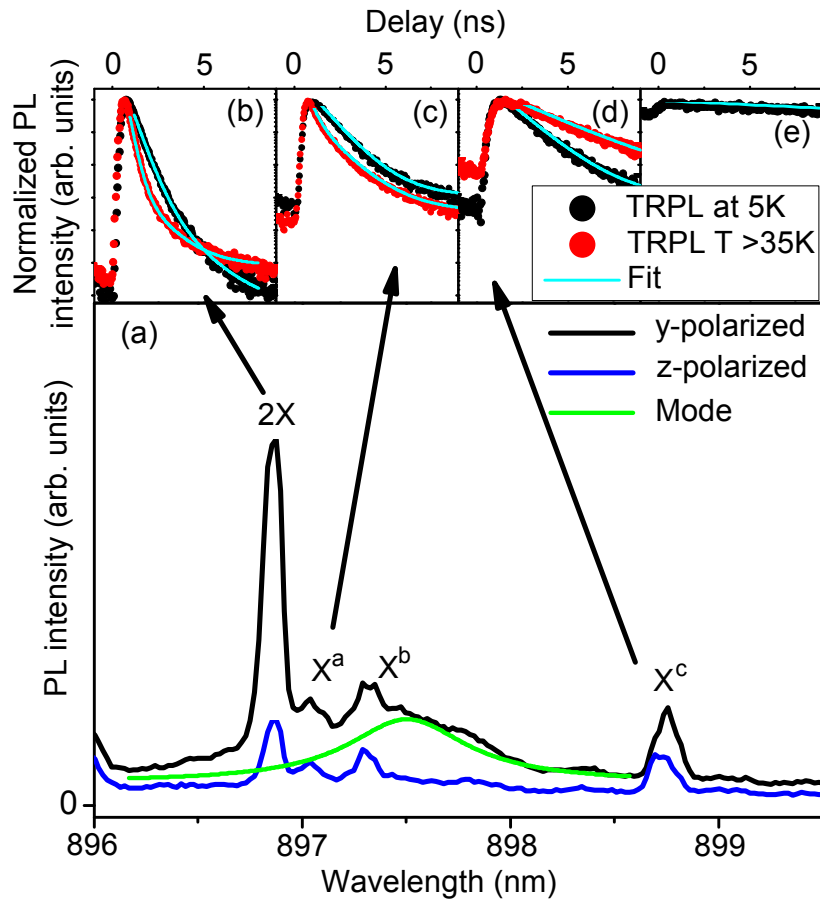


Figure 7.10: (a) In-plane polarisation-resolved PL from a PCWG with $a = 230$ nm at 5 K. The sharp lines are from QD transitions. The broad feature highlighted by the green line is the y -polarised mode M1. (b) Time-resolved PL from line 2X at 5 K and when on resonance with the mode at 50 K. (c) Time-resolved PL from line X^a at 5 K and when on resonance with the mode at 40 K. (d) Time-resolved PL from line X^c at 5 K and at 40 K. (e) TRPL from a QD exciton located inside the photonic crystal region.

Finally, figure 7.10 (e) shows time-resolved PL from a bright QD exciton emitting at 891 nm which has an estimated lifetime of 38.5 ns, a suppression by a factor ~ 30 . By moving the position of the laser and peaking up on the QD signal, it is apparent that this dot is located inside the photonic crystal region surrounding the waveguide. Accordingly the radiative lifetime is strongly suppressed due to the low density of states inside the photonic band gap. Similar lines with very long lifetimes appear in the spectra of many of the PCWGs measured.

7.7 Further work

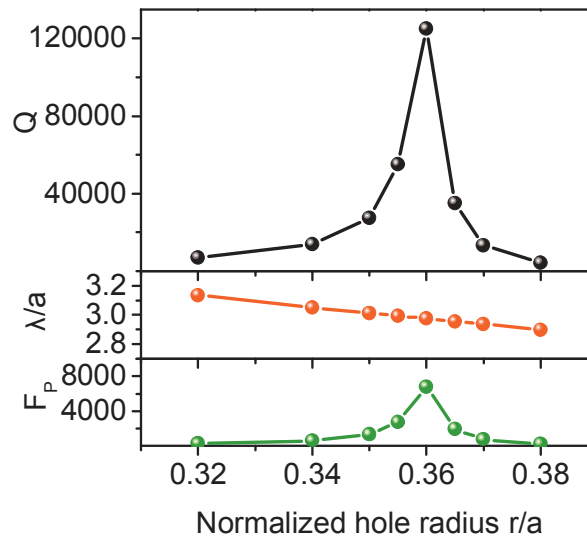


Figure 7.11: Results of FDTD simulations for the x -polarised mode M3 of a W1 unidirectional photonic crystal waveguide with $d/a = 0.7$, $l/a = 12$ and $n = 3.53$, as the radius of the holes, r/a , is changed.

Figure 7.11 shows the results of FDTD simulations of the Q -factor of the x -polarised mode M3 as the radius of the holes is changed. The maximum Q -factor is found to be very high at $Q = 125000$, with an equivalent maximum Purcell factor of $F_P = 6790$. In the same way that PL was measured in-plane from the first x -polarised mode M2, as shown in figure 7.12, it should be possible to

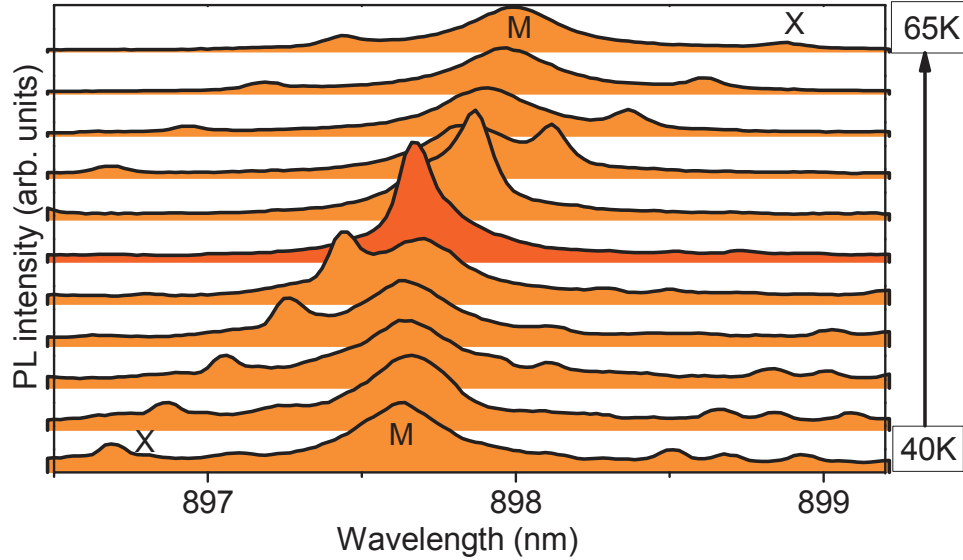


Figure 7.12: In-plane PL from a QD coupled to the x -polarised mode M2 between 40 K and 65 K. As the temperature is increased, the QD line (labeled X) comes onto resonance with the mode, before moving off resonance.

couple a QD to this very high Q mode to use as an in-plane quantum light source. Furthermore, since this mode occurs at a lower normalised wavelength than M1 and M2, a larger periodicity would be required to see the mode at around 900 nm, and it would therefore be much easier to avoid the effects of fabrication imperfections. Alternatively it may be possible to shift one of the other modes to be resonant at a lower value of the normalised wavelength by changing other parameters of the waveguide [83].

7.8 Summary and outlook

The operation of a new kind of optical cavity based on a photonic crystal waveguide has been investigated. The design has been significantly improved by FDTD simulations for a strong Purcell effect. The fabrication of the device led to the measurement of a Purcell enhancement of $F_P = 2.7$ for the in-plane emission of a QD for the first time. These results lead the way toward an in-plane quantum light source for a future photonic integrated circuit.

Chapter 8

Conclusions

Quantum dots hold great potential for new technologies based on the use of single photons. Their usefulness stems from the relatively simple internal dynamics, which often may be considered as two or three level systems, and the ease of their integration with other semiconductor techniques. Quantum dots can be manipulated by controlling either the population of carriers confined by the dot or the photonic environment that the dot experiences. In this thesis, both of these methods were used to develop a number of quantum dot based devices which may find uses as components in future quantum information technologies.

Controlling the polarisation correlation of photon pairs

The biexciton decay may be used to obtain two photons whose polarisations are either classically correlated in the linear (H or V) basis, or entangled, depending on the magnitude of the exciton fine structure splitting. For either of these applications, emission from other states (e.g. charged excitons) will reduce the efficiency of the source and may degrade the polarisation fidelity by contributing unwanted background light. It was demonstrated that by selectively controlling the hole population of a quantum dot with an electron tunnelling barrier and an electric field, the particular excitonic species which are present in its emission can be controlled. By choosing the appropriate conditions, the intensity of the emission from the biexciton decay (or from either charged exciton, if desired) can be maximised.

Furthermore it was found that the degree of classical polarisation correlation between the two photons emitted in the biexciton decay from this device was modified as the electric field applied to the quantum dot was changed. Cross-correlation and time-resolved measurements gave evidence that exciton spin scattering was responsible for this behaviour. By choosing conditions so that the intensity and degree of polarisation correlation are maximised, applications based on the biexciton decay may benefit.

Single quantum dot memory

The operation of a digital memory device based on a single quantum dot embedded in a *p-i-n* diode was demonstrated. The angular momentum selection rules of a photon exciting an electron inside the device when under an external magnetic field were exploited to populate a single quantum dot with an exciton, whose electron spin was determined by the circular polarisation of the photon. By applying an appropriate electric field across the dot, the exciton's hole was removed, leaving the electron behind due to the electron tunnelling barrier. In this way, spontaneous emission from the dot was prohibited for some time. By changing the electric field it was possible to reintroduce two holes into the dot on demand so that spontaneous emission could take place. It was found, as expected, that the emitted photon's polarisation was strongly correlated with that of the initial photon. The digital polarisation information of the initial photon was stored as the spin of an electron inside a quantum dot, and was deterministically recovered at up to 1 μ s later by the application of an electrical trigger.

Fabrication of photonic crystals

Extensive work was carried out in the development of a fabrication process to produce high quality two dimensional slab photonic crystal structures operating with a photonic band gap in the near infrared, for integration with InAs quantum dot devices.

Strong coupling in a H1 photonic crystal cavity

The phenomena of strong coupling, in which energy oscillates between an exciton in a quantum dot and a photon in a surrounding optical cavity, was achieved and investigated using a single quantum dot and the monopole mode of a H1 photonic crystal cavity. H1 cavities are appealing because of their tiny mode volume and because of the properties of the degenerate dipole modes, which are attractive for use in quantum dot entangled photon pair sources. The design of the cavity and optimisation of the fabrication process led to sufficiently high monopole Q -factors so that the photon could be confined in the cavity long enough for it to be reabsorbed by the quantum dot. The use of the monopole mode meant that the vacuum Rabi splitting persisted for all linear polarisations, a feature never seen before. Furthermore, strong coupling was achieved in a H1 cavity at a wavelength of ~ 880 nm, where the fine structure splitting of the exciton in InAs quantum dots is close to zero.

Unidirectional photonic crystal waveguide

Many quantum dot based devices require some kind of optical cavity to direct the emission in a useful direction, and to speed up the process of spontaneous emission. In the final chapter of this thesis, the potential of a new type of cavity based on the use of a photonic crystal waveguide was investigated. A unidirectional photonic crystal waveguide may provide all of the benefits of traditional optical cavities, with the added benefit of in-plane directed emission (among others). The design of the cavity was optimised, and its fabrication led to the measurement of a Purcell enhancement of the in-plane spontaneous emission from a quantum dot for the first time. This kind of cavity may find applications as an on-chip quantum light source and in future photonic integrated circuits.

Appendix A

Photonic band gap

This Appendix gives a summary of the theory behind photonic crystals, adapted from the analysis in reference [59]. The macroscopic behaviour of light is described by the Maxwell equations

$$\begin{aligned}\nabla \cdot \mathbf{B} &= 0 & \nabla \times \mathbf{E} + \frac{\partial \mathbf{B}}{\partial t} &= 0 \\ \nabla \cdot \mathbf{D} &= \rho & \nabla \times \mathbf{H} - \frac{\partial \mathbf{D}}{\partial t} &= \mathbf{J}\end{aligned}\tag{A.1}$$

where \mathbf{B} is the magnetic field, \mathbf{E} is the electric field, \mathbf{D} is the displacement field, \mathbf{H} is the magnetic induction field, ρ is the free charge density and \mathbf{J} is the current density. In a medium whose structure does not vary with time, with no free charges or currents, $\rho = 0$ and $\mathbf{J} = 0$.

Assuming that the field strengths are small, so that the effects of nonlinear optics can be ignored, and that the material is isotropic, transparent, and non-dispersive, then \mathbf{D} and \mathbf{E} are simply related by a real and positive scalar function $\epsilon(\mathbf{r})$. This is the dielectric function, where $\mathbf{D}(\mathbf{r}) = \epsilon_0 \epsilon(\mathbf{r}) \mathbf{E}(\mathbf{r})$, with ϵ_0 being the vacuum permittivity. Similarly \mathbf{H} and \mathbf{B} are related by a relative magnetic permeability, $\mu(\mathbf{r})$, like $\mathbf{B}(\mathbf{r}) = \mu_0 \mu(\mathbf{r}) \mathbf{H}(\mathbf{r})$, where μ_0 is the vacuum permeability. $\mu(\mathbf{r})$ is in general very close to unity for dielectric materials of interest, so using $\mathbf{B} = \mu_0 \mathbf{H}$, the Maxwell equations can be rewritten as

$$\begin{aligned}
\nabla \cdot \mathbf{H}(\mathbf{r}, t) &= 0 & \nabla \times \mathbf{E}(\mathbf{r}, t) + \mu_0 \frac{\partial \mathbf{H}(\mathbf{r}, t)}{\partial t} &= 0 \\
\nabla \cdot [\epsilon(\mathbf{r}) \mathbf{E}(\mathbf{r}, t)] &= 0 & \nabla \times \mathbf{H}(\mathbf{r}, t) - \epsilon_0 \epsilon(\mathbf{r}) \frac{\partial \mathbf{E}(\mathbf{r}, t)}{\partial t} &= 0
\end{aligned} \tag{A.2}$$

Since these equations are linear, the time- and spatial-dependence parts of their solutions can be separated out like

$$\begin{aligned}
\mathbf{H}(\mathbf{r}, t) &= \mathbf{H}(\mathbf{r}) e^{-i\omega t} \\
\mathbf{E}(\mathbf{r}, t) &= \mathbf{E}(\mathbf{r}) e^{-i\omega t}.
\end{aligned} \tag{A.3}$$

These equations describe a harmonic mode of the system as the product of a mode profile ($\mathbf{H}(\mathbf{r})$ or $\mathbf{E}(\mathbf{r})$) and a complex exponential. The real part of the complex exponential describes a sinusoidally varying field in time. Using Fourier analysis, any solution can be built out of a combination of these harmonic modes.

Inserting these equations back into the Maxwell equations gives

$$\begin{aligned}
\nabla \cdot \mathbf{H}(\mathbf{r}) &= 0 & \nabla \times \mathbf{E}(\mathbf{r}) - i\omega \mu_0 \mathbf{H}(\mathbf{r}) &= 0 \\
\nabla \cdot [\epsilon(\mathbf{r}) \mathbf{E}(\mathbf{r})] &= 0 & \nabla \times \mathbf{H}(\mathbf{r}) + i\omega \epsilon_0 \epsilon(\mathbf{r}) \mathbf{E}(\mathbf{r}) &= 0
\end{aligned} \tag{A.4}$$

The equations on the left hand side restrict the mode profiles to be composed of transverse electromagnetic waves. The other two equations can be combined to eliminate $\mathbf{E}(\mathbf{r})$ to give

$$\nabla \times \left(\frac{1}{\epsilon(\mathbf{r})} \nabla \times \mathbf{H}(\mathbf{r}) \right) = \left(\frac{\omega}{c} \right)^2 \mathbf{H}(\mathbf{r}) \tag{A.5}$$

where $c = 1/\sqrt{\epsilon_0 \mu_0}$, the speed of light. This equation is called the master equation of the system. By solving it subject to the transversality requirement, the allowed modes $\mathbf{H}(\mathbf{r})$ and their frequencies, for a given dielectric function, can be found.

	Quantum mechanics	Electrodynamics
Field	$\Psi(\mathbf{r}, t) = \Psi(\mathbf{r})e^{-iEt/\hbar}$	$\mathbf{H}(\mathbf{r}, t) = \mathbf{H}(\mathbf{r})e^{-i\omega t}$
Eigenvalue problem	$\hat{H}\Psi = E\Psi$	$\hat{\Theta}\mathbf{H} = (\omega/c)^2\mathbf{H}$
Hermitian operator	$\hat{H} = -(\hbar^2/2m)\nabla^2 + V(\mathbf{r})$	$\hat{\Theta} = \nabla \times (1/\epsilon(\mathbf{r}))\nabla \times$
Discrete translational symmetry	$V(\mathbf{r}) = V(\mathbf{r} + \mathbf{R})$	$\epsilon(\mathbf{r}) = \epsilon(\mathbf{r} + \mathbf{R})$
Bloch's theorem	$\Psi_{\mathbf{k}m}(\mathbf{r}) = u_{\mathbf{k}m}(\mathbf{r})e^{i\mathbf{k}\cdot\mathbf{r}}$	$\mathbf{H}_{\mathbf{k}m}(\mathbf{r}) = \mathbf{u}_{\mathbf{k}m}(\mathbf{r})e^{i\mathbf{k}\cdot\mathbf{r}}$

Table A.1: Comparison of quantum mechanics and electrodynamics. Adapted from [59].

The master equation has the form of an eigenvalue problem, and can be rewritten like

$$\hat{\Theta}\mathbf{H}(\mathbf{r}) = \left(\frac{\omega}{c}\right)^2 \mathbf{H}(\mathbf{r}) \quad (\text{A.6})$$

where the operator $\hat{\Theta}$ is defined as

$$\hat{\Theta} \equiv \nabla \times \left(\frac{1}{\epsilon(\mathbf{r})} \nabla \times \mathbf{H}(\mathbf{r}) \right). \quad (\text{A.7})$$

In this form, $(\omega/c)^2$ are the eigenvalues of the eigenfunctions $\mathbf{H}(\mathbf{r})$.

It turns out that the operator $\hat{\Theta}$ is Hermitian [59]. The master equation is therefore analogous to the time independent Schroedinger equation in quantum mechanics. Many of the interesting results concerning photonic crystals have analogies in quantum mechanics. Table A.1 summarises the similarities.

The Hermiticity of the operator implies that the eigenfunctions have real eigenvalues and that they are orthogonal. The eigenfunctions obey a variational theorem, analogous to the variational principle in quantum mechanics. In vague terms, this says that a mode tends to concentrate its electric field energy in regions of high dielectric constant and to minimize the amount of spatial oscillations in its profile, while remaining orthogonal to the modes below it in frequency. Furthermore, the spectrum of the system will become discrete if the fields are spatially bound, either because they are localized or because they are periodic.

In a photonic crystal, the structure has a periodic variation in the dielectric function. i.e.

$$\epsilon(\mathbf{r}) = \epsilon(\mathbf{r} + \mathbf{R}) \quad (\text{A.8})$$

where \mathbf{R} is any linear combination of the primitive lattice vectors of the periodic structure. As in solid state physics, the modes of this system are Bloch modes - a plane wave multiplied by a periodic function:

$$\mathbf{H}_{\mathbf{k}m}(\mathbf{r}) = \mathbf{u}_{\mathbf{k}m}(\mathbf{r})e^{i\mathbf{k}\cdot\mathbf{r}}, \quad (\text{A.9})$$

where \mathbf{k} is the Bloch wave vector, and $\mathbf{u}_{\mathbf{k}m}(\mathbf{r}) = \mathbf{u}_{\mathbf{k}m}(\mathbf{r} + \mathbf{R})$ is a periodic function. The behaviour of the modes can therefore be summarised in a band diagram spanning the Brillouin zone. For each value of \mathbf{k} , there is a discrete set of modes which are labeled with the band index m . For each of these modes, the frequency varies continuously with \mathbf{k} , so it is possible to speak of a frequency band with band index m .

The periodicity in the dielectric function causes Bragg reflections of photons which gives rise to band gaps between some of the bands, just as a periodic potential in solid state physics causes Bragg reflection of electrons which gives rise to electronic band gaps.

When a periodicity of a is introduced into the dielectric function, the modes which have a wavelength of $2a$ are forced into one of two distributions. Either the nodes of the electric field are positioned in the high- ϵ regions, or in the low- ϵ regions, due to the symmetry of the system. From the variational theorem, modes with more of their electric field energy concentrated in the high- ϵ regions have a lower frequency (and vice-versa). Therefore there is a frequency difference between the two cases, and a band gap appears.

The bands below the band gap tend to have more of their energy concentrated in the high- ϵ regions, and those above have more energy concentrated in the low- ϵ regions. In real implementations, often the low- ϵ regions are air regions. Hence the band above the band gap is called the air band and the band below is called the dielectric band.

Light with a frequency inside the band gap cannot propagate through the photonic crystal. Such light which is incident on a photonic crystal will decay exponentially inside the crystal and will be reflected.

References

- [1] S Adachi. GaAs, AlAs, and Al_xGa_{1-x}As - Material parameters for use in research and device applications. *JOURNAL OF APPLIED PHYSICS*, 58 (3):R1–R29, 1985. 34
- [2] Y Akahane, T Asano, BS Song, and S Noda. High-Q photonic nanocavity in a two-dimensional photonic crystal. *NATURE*, 425(6961):944–947, OCT 30 2003. 23, 77, 81, 94
- [3] Y Akahane, T Asano, BS Song, and S Noda. Fine-tuned high-Q photonic-crystal nanocavity. *OPTICS EXPRESS*, 13(4):1202–1214, FEB 21 2005. 23
- [4] N Akopian, NH Lindner, E Poem, Y Berlatzky, J Avron, D Gershoni, BD Gerardot, and PM Petroff. Entangled photon pairs from semiconductor quantum dots. *PHYSICAL REVIEW LETTERS*, 96(13), 2006. 37
- [5] LC Andreani, G Panzarini, and JM Gerard. Strong-coupling regime for quantum boxes in pillar microcavities: Theory. *PHYSICAL REVIEW B*, 60(19):13276–13279, NOV 15 1999. 14
- [6] T Asano, BS Song, and S Noda. Analysis of the experimental Q factors (similar to 1 million) of photonic crystal nanocavities. *OPTICS EXPRESS*, 14(5):1996–2002, MAR 6 2006. 63
- [7] P Atkinson, MB Ward, SP Bremner, D Anderson, T Farrow, GAC Jones, AJ Shields, and DA Ritchie. Site-control of InAs quantum dots using ex-situ electron-beam lithographic patterning of GaAs substrates. *JAPANESE JOURNAL OF APPLIED PHYSICS*, 45(4A):2519–2521, APR 2006. 107

REFERENCES

- [8] Alexia Auffèves, Benjamin Besga, Jean-Michel Gérard, and Jean-Philippe Poizat. Spontaneous emission spectrum of a two-level atom in a very-high- q cavity. *PHYSICAL REVIEW A*, 77(6):063833, Jun 2008. 89
- [9] Toshihiko Baba. Slow light in photonic crystals. *NATURE PHOTONICS*, 2(8):465–473, AUG 2008. 95
- [10] A Badolato, K Hennessy, M Atature, J Dreiser, E Hu, PM Petroff, and A Imamoglu. Deterministic coupling of single quantum dots to single nanocavity modes. *SCIENCE*, 308(5725):1158–1161, MAY 20 2005. 94
- [11] T Basche, WE Moerner, M Orrit, and H Talon. Photon antibunching in the fluorescence of a single dye molecule trapped in a solid. *PHYSICAL REVIEW LETTERS*, 69(10):1516–1519, SEP 7 1992. 2
- [12] M Bayer, G Ortner, O Stern, A Kuther, AA Gorbunov, A Forchel, P Hawrylak, S Fafard, K Hinzer, TL Reinecke, SN Walck, JP Reithmaier, F Klopff, and F Schafer. Fine structure of neutral and charged excitons in self-assembled in(ga)as/(al)gaas quantum dots. *PHYSICAL REVIEW B*, 65:195315, 2002. 7, 10
- [13] NS Beattie, BE Kardynal, AJ Shields, I Farrer, DA Ritchie, and M Pepper. Single-photon detection mechanism in a quantum dot transistor. *PHYSICA E-LOW-DIMENSIONAL SYSTEMS & NANOSTRUCTURES*, 26(1-4):356–360, FEB 2005. 3rd International Conference on Quantum Dots (QD 2004), Banff, CANADA, MAY 10-13, 2004. 2, 37
- [14] H Benisty, H De Neve, and C Weisbuch. Impact of planar microcavity effects on light extraction - Part I: Basic concepts and analytical trends. *IEEE JOURNAL OF QUANTUM ELECTRONICS*, 34(9):1612–1631, SEP 1998. 10, 17, 37
- [15] AJ Bennett, DC Unitt, P Atkinson, DA Ritchie, and AJ Shields. High performance single photon sources from photolithographically defined pillar microcavities. *OPTICS EXPRESS*, 13(1):50–55, JAN 10 2005. 2, 37

REFERENCES

- [16] CH Bennett and G Brassard. Quantum cryptography: Public key distribution and coin tossing. *PROCEEDINGS OF IEEE INTERNATIONAL CONFERENCE ON COMPUTERS, SYSTEMS AND SIGNAL PROCESSING*, page 175, 1984. 1, 45
- [17] O Benson, C Santori, M Pelton, and Y Yamamoto. Regulated and entangled photons from a single quantum dot. *PHYSICAL REVIEW LETTERS*, 84(11):2513–2516, MAR 13 2000. 37
- [18] L Besombes, K Kheng, and D Martrou. Exciton and biexciton fine structure in single elongated islands grown on a vicinal surface. *PHYSICAL REVIEW LETTERS*, 85(2):425–428, JUL 10 2000. 10
- [19] D Bimberg, M Grundmann, and MM Ledentsov. *Quantum Dot Heterostructures*. Wiley, Chichester, 1999. 3, 34
- [20] D Bimberg, N Kirstaedter, NN Ledentsov, ZI Alferov, PS Kopev, and VM Ustinov. InGaAs-GaAs quantum-dot lasers. *IEEE JOURNAL OF SELECTED TOPICS IN QUANTUM ELECTRONICS*, 3(2):196–205, APR 1997. 15th IEEE International Semiconductor Laser Conference (HAIFA 1996 ISLC), HAIFA, ISRAEL, OCT 13-18, 1996. 37
- [21] JC Blakesley, P See, AJ Shields, BE Kardynal, P Atkinson, I Farrer, and DA Ritchie. Efficient single photon detection by quantum dot resonant tunneling diodes. *PHYSICAL REVIEW LETTERS*, 94(6), FEB 18 2005. 2, 37
- [22] BB Blinov, DL Moehring, LM Duan, and C Monroe. Observation of entanglement between a single trapped atom and a single photon. *NATURE*, 428(6979):153–157, MAR 11 2004. 2, 76
- [23] D Bouwmeester, JW Pan, K Mattle, M Eibl, H Weinfurter, and A Zeilinger. Experimental quantum teleportation. *NATURE*, 390(6660):575–579, DEC 11 1997. 1

REFERENCES

- [24] J Brendel, N Gisin, W Tittel, and H Zbinden. Pulsed energy-time entangled twin-photon source for quantum communication. *PHYSICAL REVIEW LETTERS*, 82(12):2594–2597, MAR 22 1999. 1
- [25] HJ Briegel, W Dur, JI Cirac, and P Zoller. Quantum repeaters: The role of imperfect local operations in quantum communication. *PHYSICAL REVIEW LETTERS*, 81(26):5932–5935, DEC 28 1998. 1
- [26] HJ Briegel, T Calarco, D Jaksch, JI Cirac, and P Zoller. Quantum computing with neutral atoms. *JOURNAL OF MODERN OPTICS*, 47(2-3):415–451, FEB-MAR 2000. 45
- [27] C Brunel, B Lounis, P Tamarat, and M Orrit. Triggered source of single photons based on controlled single molecule fluorescence. *PHYSICAL REVIEW LETTERS*, 83(14):2722–2725, OCT 4 1999. 2
- [28] ARA Chalcraft, S Lam, D O’Brien, TF Krauss, M Sahin, D Szymanski, D Sanvitto, R Oulton, MS Skolnick, AM Fox, DM Whittaker, H-Y Liu, and M Hopkinson. Mode structure of the L3 photonic crystal cavity. *APPLIED PHYSICS LETTERS*, 90(24), JUN 11 2007. 77
- [29] WH Chang, WY Chen, HS Chang, TP Hsieh, JI Chyi, and TM Hsu. Efficient single-photon sources based on low-density quantum dots in photonic-crystal nanocavities. *PHYSICAL REVIEW LETTERS*, 96(11), MAR 24 2006. 37, 94
- [30] A Chutinan and S Noda. Waveguides and waveguide bends in two-dimensional photonic crystal slabs. *PHYSICAL REVIEW B*, 62(7):4488–4492, AUG 15 2000. 95
- [31] JI Cirac and P Zoller. Quantum computations with cold trapped ions. *PHYSICAL REVIEW LETTERS*, 74(20):4091–4094, MAY 15 1995. 45
- [32] F DIEDRICH and H WALTHER. Nonclassical radiation of a single stored ion. *PHYSICAL REVIEW LETTERS*, 58(3):203–206, JAN 19 1987. 2

REFERENCES

- [33] A Dousse, J Suffczynski, R Braive, A Miard, A Lemaitre, I Sagnes, L Lanco, J Bloch, P Voisin, and P Senellart. Scalable implementation of strongly coupled cavity-quantum dot devices. *APPLIED PHYSICS LETTERS*, 94(12), MAR 23 2009. 17, 76
- [34] D Englund, D Fattal, E Waks, G Solomon, B Zhang, T Nakaoka, Y Arakawa, Y Yamamoto, and J Vuckovic. Controlling the spontaneous emission rate of single quantum dots in a two-dimensional photonic crystal. *PHYSICAL REVIEW LETTERS*, 95(1), JUL 1 2005. 37, 94
- [35] Dirk Englund, Andrei Faraon, Ilya Fushman, Nick Stoltz, Pierre Petroff, and Jelena Vuckovic. Controlling cavity reflectivity with a single quantum dot. *NATURE*, 450(7171):857–861, DEC 6 2007. 2, 76
- [36] SH Fan, PR Villeneuve, JD Joannopoulos, and EF Schubert. High extraction efficiency of spontaneous emission from slabs of photonic crystals. *PHYSICAL REVIEW LETTERS*, 78(17):3294–3297, APR 28 1997. 20
- [37] A Faraon, D Englund, I Fushman, J Vuckovic, N Stoltz, and P Petroff. Local quantum dot tuning on photonic crystal chips. *APPLIED PHYSICS LETTERS*, 90(21), MAY 21 2007. 76
- [38] A Faraon, I Fushman, D Englund, N Stoltz, P Petroff, and J Vuckovic. Coherent generation of non-classical light on a chip via photon-induced tunnelling and blockade. *NATURE PHYSICS*, 4(11):859–863, NOV 2008. 76
- [39] JJ Finley, PW Fry, AD Ashmore, A Lemaitre, AI Tartakovskii, R Oulton, DJ Mowbray, MS Skolnick, M Hopkinson, PD Buckle, and PA Maksym. Observation of multicharged excitons and biexcitons in a single InGaAs quantum dot. *PHYSICAL REVIEW B*, 63(16), APR 15 2001. 41
- [40] M Fox. *Quantum Optics: An Introduction*. Oxford University Press, Oxford, 2006. 12, 45

REFERENCES

- [41] M Fujita, S Takahashi, Y Tanaka, T Asano, and S Noda. Simultaneous inhibition and redistribution of spontaneous light emission in photonic crystals. *SCIENCE*, 308(5726):1296–1298, MAY 27 2005. 20
- [42] I Fushman, D Englund, A Faraon, N Stoltz, P Petroff, and J Vuckovic. Controlled phase shifts with a single quantum dot. *SCIENCE*, 320(5877):769–772, MAY 9 2008. 76
- [43] D Gammon, ES Snow, BV Shanabrook, DS Katzer, and D Park. Fine structure splitting in the optical spectra of single GaAs quantum dots. *PHYSICAL REVIEW LETTERS*, 76(16):3005–3008, APR 15 1996. 8, 41
- [44] D Gerace and LC Andreani. Effects of disorder on propagation losses and cavity Q-factors in photonic crystal slabs. *PHOTONICS AND NANOSTRUCTURES-FUNDAMENTALS AND APPLICATIONS*, 3(2-3):120–128, DEC 2005. 6th International Symposium on Photonic and Electromagnetic Crystal Structures (PECS-VI), Aghia Pelaghia, GREECE, JUN, 2005. 24, 63
- [45] JM Gerard, B Sermage, B Gayral, B Legrand, E Costard, and V Thierry-Mieg. Enhanced spontaneous emission by quantum boxes in a monolithic optical microcavity. *PHYSICAL REVIEW LETTERS*, 81(5):1110–1113, AUG 3 1998. 94
- [46] DG Gevaux, AJ Bennett, RM Stevenson, AJ Shields, P Atkinson, J Griffiths, D Anderson, GAC Jones, and DA Ritchie. Enhancement and suppression of spontaneous emission by temperature tuning InAs quantum dots to photonic crystal cavities. *APPLIED PHYSICS LETTERS*, 88(13), MAR 27 2006. 63, 77, 87, 94
- [47] N Gisin, GG Ribordy, W Tittel, and H Zbinden. Quantum cryptography. *REVIEWS OF MODERN PHYSICS*, 74(1):145–195, JAN 2002. 1
- [48] A Hartmann, Y Ducommun, E Kapon, U Hohenester, and E Molinari. Few-particle effects in semiconductor quantum dots: Observation of multicharged excitons. *PHYSICAL REVIEW LETTERS*, 84(24):5648–5651, JUN 12 2000. 39

REFERENCES

- [49] K Hennessy, C Hoegerle, E Hu, A Badolato, and A Imamoglu. Tuning photonic nanocavities by atomic force microscope nano-oxidation. *APPLIED PHYSICS LETTERS*, 89(4), JUL 24 2006. 77
- [50] K Hennessy, A Badolato, M Winger, D Gerace, M Atatuere, S Gulde, S Faelt, EL Hu, and A Imamoglu. Quantum nature of a strongly coupled single quantum dot-cavity system. *NATURE*, 445(7130):896–899, FEB 22 2007. 76, 94
- [51] MA Herman and H Sitter. MBE growth physics: Application to device technology. *MICROELECTRONICS JOURNAL*, 27(4-5):257–296, JUL-AUG 1996. 25
- [52] R Herrmann, T Sunner, T Hein, A Loffler, M Kamp, and A Forchel. Ultrahigh-quality photonic crystal cavity in GaAs. *OPTICS LETTERS*, 31(9):1229–1231, MAY 1 2006. 20
- [53] CK HONG and L MANDEL. Experimental realization of a localized one-photon state. *PHYSICAL REVIEW LETTERS*, 56(1):58–60, JAN 6 1986. 1
- [54] S Hughes. Enhanced single-photon emission from quantum dots in photonic crystal waveguides and nanocavities. *OPTICS LETTERS*, 29(22):2659–2661, NOV 15 2004. 95
- [55] S Hughes, L Ramunno, JF Young, and JE Sipe. Extrinsic optical scattering loss in photonic crystal waveguides: Role of fabrication disorder and photon group velocity. *PHYSICAL REVIEW LETTERS*, 94(3), JAN 28 2005. 95
- [56] J Huh, JK Hwang, HY Ryu, and YH Lee. Nondegenerate monopole mode of single defect two-dimensional triangular photonic band-gap cavity. *JOURNAL OF APPLIED PHYSICS*, 92(2):654–659, JUL 15 2002. 77
- [57] E. Illes and S. Hughes. Photon antibunching in strongly coupled exciton-semiconductor cavity systems: Role of off-resonant coupling to multiple excitons. *PHYSICAL REVIEW B*, 81:121310, MAR 2010. 89

REFERENCES

- [58] A Imamoglu, DD Awschalom, G Burkard, DP DiVincenzo, D Loss, M Sherwin, and A Small. Quantum information processing using quantum dot spins and cavity QED. *PHYSICAL REVIEW LETTERS*, 83(20):4204–4207, NOV 15 1999. 2, 76
- [59] JD Joannopoulos, SG Johnson, JN Winn, and RD Meade. *Photonic Crystals: Molding the Flow of Light*. Princeton University Press, Princeton, second edition. 20, 22, 77, 80, 115, 117
- [60] S John. Strong localization of photons in certain disordered dielectric superlattices. *PHYSICAL REVIEW LETTERS*, 58(23):2486–2489, JUN 8 1987. 18
- [61] R Johne, NA Gippius, G Pavlovic, DD Solnyshkov, IA Shelykh, and G Malpuech. Entangled photon pairs produced by a quantum dot strongly coupled to a microcavity. *PHYSICAL REVIEW LETTERS*, 100(24), JUN 20 2008. 76
- [62] SG Johnson, SH Fan, PR Villeneuve, JD Joannopoulos, and LA Kolodziejski. Guided modes in photonic crystal slabs. *PHYSICAL REVIEW B*, 60(8):5751–5758, AUG 15 1999. 82
- [63] G Khitrova, HM Gibbs, M Kira, SW Koch, and A Scherer. Vacuum Rabi splitting in semiconductors. *NATURE PHYSICS*, 2(2):81–90, FEB 2006. 76
- [64] J Kim, O Benson, H Kan, and Y Yamamoto. A single-photon turnstile device. *NATURE*, 397(6719):500–503, FEB 11 1999. 2
- [65] SH Kim, GH Kim, SK Kim, HG Park, YH Lee, and SB Kim. Characteristics of a stick waveguide resonator in a two-dimensional photonic crystal slab. *JOURNAL OF APPLIED PHYSICS*, 95(2):411–416, JAN 15 2004. 103
- [66] SH Kim, SK Kim, and YH Lee. Vertical beaming of wavelength-scale photonic crystal resonators. *PHYSICAL REVIEW B*, 73(23), JUN 2006. 69, 83

REFERENCES

- [67] HJ Kimble, M Dagenais, and L Mandel. Photon anti-bunching in resonance fluorescence. *PHYSICAL REVIEW LETTERS*, 39(11):691–695, 1977. 2
- [68] A Kiraz, P Michler, C Becher, B Gayral, A Imamoglu, LD Zhang, E Hu, WV Schoenfeld, and PM Petroff. Cavity-quantum electrodynamics using a single InAs quantum dot in a microdisk structure. *APPLIED PHYSICS LETTERS*, 78(25):3932–3934, JUN 18 2001. 86, 94, 105
- [69] E Knill, R Laflamme, and GJ Milburn. A scheme for efficient quantum computation with linear optics. *NATURE*, 409(6816):46–52, JAN 4 2001. 1, 45
- [70] P Kok, WJ Munro, Kae Nemoto, TC Ralph, Jonathan P Dowling, and GJ Milburn. Linear optical quantum computing with photonic qubits. *REVIEWS OF MODERN PHYSICS*, 79(1):135–174, JAN-MAR 2007. 1, 45
- [71] TF Krauss. Slow light in photonic crystal waveguides. *JOURNAL OF PHYSICS D-APPLIED PHYSICS*, 40(9):2666–2670, MAY 7 2007. 95
- [72] A Kress, F Hofbauer, N Reinelt, M Kaniber, HJ Krenner, R Meyer, G Bohm, and JJ Finley. Manipulation of the spontaneous emission dynamics of quantum dots in two-dimensional photonic crystals. *PHYSICAL REVIEW B*, 71(24), JUN 2005. 94
- [73] M Kroutvar, Y Ducommun, D Heiss, M Bichler, D Schuh, G Abstreiter, and JJ Finley. Optically programmable electron spin memory using semiconductor quantum dots. *NATURE*, 432(7013):81–84, NOV 4 2004. 46, 53
- [74] VD Kulakovskii, G Bacher, R Weigand, T Kummell, A Forchel, E Borovitskaya, K Leonardi, and D Hommel. Fine structure of biexciton emission in symmetric and asymmetric CdSe/ZnSe single quantum dots. *PHYSICAL REVIEW LETTERS*, 82(8):1780–1783, FEB 22 1999. 8
- [75] E Kuramochi, M Notomi, S Mitsugi, A Shinya, T Tanabe, and T Watanabe. Ultrahigh-Q photonic crystal nanocavities realized by the local width

REFERENCES

- modulation of a line defect. *APPLIED PHYSICS LETTERS*, 88(4), JAN 23 2006. 20
- [76] C Kurtsiefer, S Mayer, P Zarda, and H Weinfurter. Stable solid-state source of single photons. *PHYSICAL REVIEW LETTERS*, 85(2):290–293, JUL 10 2000. 2
- [77] L Landin, MS Miller, ME Pistol, CE Pryor, and L Samuelson. Optical studies of individual InAs quantum dots in GaAs: Few-particle effects. *SCIENCE*, 280(5361):262–264, APR 10 1998. 39
- [78] M. Larque, T. Karle, I. Robert-Philip, and A. Beveratos. Optimizing H1 cavities for the generation of entangled photon pairs. *NEW JOURNAL OF PHYSICS*, 11, MAR 17 2009. 77
- [79] A Laucht, F Hofbauer, N Hauke, J Angele, S Stobbe, M Kaniber, G Boehm, P Lodahl, M-C Amann, and JJ Finley. Electrical control of spontaneous emission and strong coupling for a single quantum dot. *NEW JOURNAL OF PHYSICS*, 11, FEB 20 2009. 76
- [80] S Laurent, S Varoutsis, L Le Gratiet, A Lemaitre, I Sagnes, F Raineri, A Levenson, I Robert-Philip, and I Abram. Indistinguishable single photons from a single-quantum dot in a two-dimensional photonic crystal cavity. *APPLIED PHYSICS LETTERS*, 87(16), OCT 17 2005. 37
- [81] G Lecamp, P Lalanne, and JP Hugonin. Very large spontaneous-emission beta factors in photonic-crystal waveguides. *PHYSICAL REVIEW LETTERS*, 99(2), JUL 13 2007. 95
- [82] P Lodahl, AF van Driel, IS Nikolaev, A Irman, K Overgaag, DL Vanmaekelbergh, and WL Vos. Controlling the dynamics of spontaneous emission from quantum dots by photonic crystals. *NATURE*, 430(7000):654–657, AUG 5 2004. 94

REFERENCES

- [83] M Loncar, J Vuckovic, and A Scherer. Methods for controlling positions of guided modes of photonic-crystal waveguides. *JOURNAL OF THE OPTICAL SOCIETY OF AMERICA B-OPTICAL PHYSICS*, 18(9):1362–1368, SEP 2001. 98, 103, 110
- [84] D Loss and DP DiVincenzo. Quantum computation with quantum dots. *PHYSICAL REVIEW A*, 57(1):120–126, JAN 1998. 45
- [85] B Lounis and M Orrit. Single-photon sources. *REPORTS ON PROGRESS IN PHYSICS*, 68(5):1129–1179, MAY 2005. 1
- [86] B Lounis, HA Bechtel, D Gerion, P Alivisatos, and WE Moerner. Photon antibunching in single CdSe/ZnS quantum dot fluorescence. *CHEMICAL PHYSICS LETTERS*, 329(5-6):399–404, OCT 27 2000. 2
- [87] T Lund-Hansen, S Stobbe, B Julsgaard, H Thyrrstrup, T Suenner, M Kamp, A Forchel, and P Lodahl. Experimental realization of highly efficient broadband coupling of single quantum dots to a photonic crystal waveguide. *PHYSICAL REVIEW LETTERS*, 101(11), SEP 12 2008. 95
- [88] H Mabuchi and AC Doherty. Cavity quantum electrodynamics: Coherence in context. *SCIENCE*, 298(5597):1372–1377, NOV 15 2002. 76
- [89] VSC Manga Rao and S Hughes. Numerical study of exact Purcell factors in finite-size planar photonic crystal waveguides. *OPTICS LETTERS*, 33(14):1587–1589, JUL 15 2008. 98
- [90] VSC Manga Rao and S Hughes. Single quantum-dot Purcell factor and beta factor in a photonic crystal waveguide. *PHYSICAL REVIEW B*, 75(20), MAY 2007. 95
- [91] VSC Manga Rao and S Hughes. Single quantum dot spontaneous emission in a finite-size photonic crystal waveguide: Proposal for an efficient “On chip” single photon gun. *PHYSICAL REVIEW LETTERS*, 99(19), NOV 9 2007. 95, 96, 98, 99

REFERENCES

- [92] P Michler, editor. *Single Quantum Dots: Fundamentals, Applications and New Concepts*. Springer-Verlag, Berlin, 2003. 5
- [93] P Michler, A Imamoglu, MD Mason, PJ Carson, GF Strouse, and SK Buratto. Quantum correlation among photons from a single quantum dot at room temperature. *NATURE*, 406(6799):968–970, AUG 31 2000. 5, 7, 37
- [94] P Michler, A Kiraz, C Becher, WV Schoenfeld, PM Petroff, LD Zhang, E Hu, and A Imamoglu. A quantum dot single-photon turnstile device. *SCIENCE*, 290(5500):2282+, DEC 22 2000. 2, 7
- [95] S Mosor, J Hendrickson, BC Richards, J Sweet, G Khitrova, HM Gibbs, T Yoshie, A Scherer, OB Shchekin, and DG Deppe. Scanning a photonic crystal slab nanocavity by condensation of xenon. *APPLIED PHYSICS LETTERS*, 87(14), OCT 3 2005. 76
- [96] DJ Mowbray and MS Skolnick. New physics and devices based on self-assembled semiconductor quantum dots. *JOURNAL OF PHYSICS D-APPLIED PHYSICS*, 38(13):2059–2076, JUL 7 2005. 2
- [97] A. Naesby, T. Suhr, P. T. Kristensen, and J. Mørk. Influence of pure dephasing on emission spectra from single photon sources. *PHYSICAL REVIEW A*, 78(4):045802, Oct 2008. 89
- [98] Y Nakamura, YA Pashkin, and JS Tsai. Coherent control of macroscopic quantum states in a single-Cooper-pair box. *NATURE*, 398(6730):786–788, APR 29 1999. 45
- [99] GA Narvaez, G Bester, A Franceschetti, and A Zunger. Excitonic exchange effects on the radiative decay time of monoexcitons and biexcitons in quantum dots. *PHYSICAL REVIEW B*, 74(20), NOV 2006. 44
- [100] S Noda, A Chutinan, and M Imada. Trapping and emission of photons by a single defect in a photonic bandgap structure. *NATURE*, 407(6804):608–610, OCT 5 2000. 20

REFERENCES

- [101] S Noda, M Fujita, and T Asano. Spontaneous-emission control by photonic crystals and nanocavities. *NATURE PHOTONICS*, 1(8):449–458, AUG 2007. 17
- [102] M Notomi, K Yamada, A Shinya, J Takahashi, C Takahashi, and I Yokohama. Extremely large group-velocity dispersion of line-defect waveguides in photonic crystal slabs. *PHYSICAL REVIEW LETTERS*, 87(25), DEC 17 2001. 95, 96
- [103] Y Ota, M Shirane, M Nomura, N Kumagai, S Ishida, S Iwamoto, S Yorozu, and Y Arakawa. Vacuum Rabi splitting with a single quantum dot embedded in a H1 photonic crystal nanocavity. *APPLIED PHYSICS LETTERS*, 94(3), JAN 19 2009. 76, 92
- [104] ZY Ou and L Mandel. Violation of Bells-inequality and classical probability in a 2-photon correlation experiment. *PHYSICAL REVIEW LETTERS*, 61(1):50–53, JUL 4 1988. 1
- [105] O Painter, RK Lee, A Scherer, A Yariv, JD O’Brien, PD Dapkus, and I Kim. Two-dimensional photonic band-gap defect mode laser. *SCIENCE*, 284(5421):1819–1821, JUN 11 1999. 20, 37
- [106] O Painter, J Vuckovic, and A Scherer. Defect modes of a two-dimensional photonic crystal in an optically thin dielectric slab. *JOURNAL OF THE OPTICAL SOCIETY OF AMERICA B-OPTICAL PHYSICS*, 16(2):275–285, FEB 1999. 20, 77
- [107] HG Park, JK Hwang, J Huh, HY Ryu, YH Lee, and JS Kim. Nondegenerate monopole-mode two-dimensional photonic band gap laser. *APPLIED PHYSICS LETTERS*, 79(19):3032–3034, NOV 5 2001. 77
- [108] E Peter, P Senellart, D Martrou, A Lemaitre, J Hours, JM Gerard, and J Bloch. Exciton-photon strong-coupling regime for a single quantum dot embedded in a microcavity. *PHYSICAL REVIEW LETTERS*, 95(6), AUG 5 2005. 76, 89, 94

REFERENCES

- [109] A Politi, JCF Matthews, and JL O'Brien. Shor's Quantum Factoring Algorithm on a Photonic Chip. *SCIENCE*, 325(5945):1221, SEP 4 2009. 94
- [110] D Press, S Goetzinger, S Reitzenstein, C Hofmann, A Loeffler, M Kamp, A Forchel, and Y Yamamoto. Photon antibunching from a single quantum-dot-microcavity system in the strong coupling regime. *PHYSICAL REVIEW LETTERS*, 98(11), MAR 16 2007. 76
- [111] EM Purcell. Spontaneous emission probabilities at radio frequencies. *PHYSICAL REVIEW*, 69, 1946. 10, 13, 94
- [112] Johann Peter Reithmaier. Strong exciton-photon coupling in semiconductor quantum dot systems. *SEMICONDUCTOR SCIENCE AND TECHNOLOGY*, 23(12), DEC 2008. 12, 14, 15, 17, 76, 89
- [113] JP Reithmaier, G Sek, A Loffler, C Hofmann, S Kuhn, S Reitzenstein, LV Keldysh, VD Kulakovskii, TL Reinecke, and A Forchel. Strong coupling in a single quantum dot-semiconductor microcavity system. *NATURE*, 432 (7014):197–200, NOV 11 2004. 76, 89, 94
- [114] HY Ryu, M Notomi, and YH Lee. High-quality-factor and small-mode-volume hexapole modes in photonic-crystal-slab nanocavities. *APPLIED PHYSICS LETTERS*, 83(21):4294–4296, NOV 24 2003. 77
- [115] C Santori, D Fattal, M Pelton, GS Solomon, and Y Yamamoto. Polarization-correlated photon pairs from a single quantum dot. *PHYSICAL REVIEW B*. 41
- [116] C Santori, M Pelton, G Solomon, Y Dale, and E Yamamoto. Triggered single photons from a quantum dot. *PHYSICAL REVIEW LETTERS*, 86 (8):1502–1505, FEB 19 2001. 2
- [117] C Santori, D Fattal, J Vuckovic, GS Solomon, and Y Yamamoto. Indistinguishable photons from a single-photon device. *NATURE*, 419(6907): 594–597, OCT 10 2002. 37

REFERENCES

- [118] D Sanvitto, A Daraei, A Tahraoui, M Hopkinson, PW Fry, DM Whittaker, and MS Skolnick. Observation of ultrahigh quality factor in a semiconductor microcavity. *APPLIED PHYSICS LETTERS*, 86(19), MAY 9 2005. 15, 17
- [119] AJ Shields. Semiconductor quantum light sources. *NATURE PHOTONICS*, 1:215–223, 2007. 1
- [120] YH Shih and CO Alley. New type of Einstein-Podolsky-Rosen-Bohm experiment using pairs of light quanta produced by optical parametric down conversion. *PHYSICAL REVIEW LETTERS*, 61(26):2921–2924, DEC 26 1988. 1
- [121] M Shirane, S Kono, J Ushida, S Ohkouchi, N Ikeda, Y Sugimoto, and A Tomita. Mode identification of high-quality-factor single-defect nanocavities in quantum dot-embedded photonic crystals. *JOURNAL OF APPLIED PHYSICS*, 101(7), APR 1 2007. 17, 77
- [122] PW Shor. Algorithms for quantum computation: Discrete logarithms and factoring. *PROCEEDINGS OF THE 35TH ANNUAL SYMPOSIUM ON FOUNDATIONS OF COMPUTER SCIENCE*, pages 124–134, 1994. 1
- [123] JM Smith, PA Dalgarno, RJ Warburton, AO Govorov, K Karrai, BD Gerardot, and PM Petroff. Voltage control of the spin dynamics of an exciton in a semiconductor quantum dot. *PHYSICAL REVIEW LETTERS*, 94(19), MAY 20 2005. 107
- [124] BS Song, S Noda, T Asano, and Y Akahane. Ultra-high-Q photonic double-heterostructure nanocavity. *NATURE MATERIALS*, 4(3):207–210, MAR 2005. 20, 23
- [125] HZ Song, T Usuki, S Hirose, K Takemoto, Y Nakata, N Yokoyama, and Y Sakuma. Site-controlled photoluminescence at telecommunication wavelength from InAs/InP quantum dots. *APPLIED PHYSICS LETTERS*, 86(11), MAR 14 2005. 107

REFERENCES

- [126] K Srinivasan and O Painter. Linear and nonlinear optical spectroscopy of a strongly coupled microdisk-quantum dot system. *NATURE*, 450(7171): 862–U15, DEC 6 2007. 17
- [127] K Srinivasan and O Painter. Momentum space design of high-Q photonic crystal optical cavities. *OPTICS EXPRESS*, 10(15):670–684, JUL 29 2002. 23
- [128] TM Stace, GJ Milburn, and CHW Barnes. Entangled two-photon source using biexciton emission of an asymmetric quantum dot in a cavity. *PHYSICAL REVIEW B*, 67(8), FEB 15 2003. 77
- [129] RM Stevenson, RM Thompson, AJ Shields, I Farrer, BE Kardynal, DA Ritchie, and M Pepper. Quantum dots as a photon source for passive quantum key encoding. *PHYSICAL REVIEW B*, 66(8), AUG 15 2002. 41
- [130] RM Stevenson, RJ Young, P Atkinson, K Cooper, DA Ritchie, and AJ Shields. A semiconductor source of triggered entangled photon pairs. *NATURE*, 439(7073):179–182, JAN 12 2006. 2, 8, 37, 41, 93
- [131] Wolfgang C. Stumpf, Masayuki Fujita, Makoto Yamaguchi, Takashi Asano, and Susumu Noda. Light-emission properties of quantum dots embedded in a photonic double-heterostructure nanocavity. *APPLIED PHYSICS LETTERS*, 90(23), JUN 4 2007. 20, 96
- [132] A Tandaechanurat, S Iwamoto, M Nomura, N Kumagai, and Y Arakawa. Increase of Q-factor in photonic crystal H1-defect nanocavities after closing of photonic bandgap with optimal slab thickness. *OPTICS EXPRESS*, 16(1):448–455, JAN 7 2008. 82
- [133] RM Thompson, RM Stevenson, AJ Shields, I Farrer, CJ Lobo, DA Ritchie, ML Leadbeater, and M Pepper. Single-photon emission from exciton complexes in individual quantum dots. *PHYSICAL REVIEW B*, 64(20), NOV 15 2001. 5, 7

REFERENCES

- [134] SM Ulrich, S Strauf, P Michler, G Bacher, and A Forchel. Triggered polarization-correlated photon pairs from a single CdSe quantum dot. *APPLIED PHYSICS LETTERS*, 83(9):1848–1850, SEP 1 2003. 41
- [135] KJ Vahala. Optical microcavities. *NATURE*, 424(6950):839–846, AUG 14 2003. 10, 17
- [136] E Viasnoff-Schwoob, C Weisbuch, H Benisty, S Olivier, S Varoutsis, I Robert-Philip, R Houdre, and CJM Smith. Spontaneous emission enhancement of quantum dots in a photonic crystal wire. *PHYSICAL REVIEW LETTERS*, 95(18), OCT 28 2005. 95
- [137] J Vuckovic, M Loncar, H Mabuchi, and A Scherer. Optimization of the Q factor in photonic crystal microcavities. *IEEE JOURNAL OF QUANTUM ELECTRONICS*, 38(7):850–856, JUL 2002. 23
- [138] J Vuckovic, M Loncar, H Mabuchi, and A Scherer. Design of photonic crystal microcavities for cavity QED. *PHYSICAL REVIEW E*, 65(1, Part 2), JAN 2002. 76
- [139] E Waks, K Inoue, C Santori, D Fattal, J Vuckovic, GS Solomon, and Y Yamamoto. Secure communication: Quantum cryptography with a photon turnstile. *NATURE*, 420(6917):762, DEC 26 2002. 1
- [140] RJ Warburton, C Schafflein, D Haft, F Bickel, A Lorke, K Karrai, JM Garcia, W Schoenfeld, and PM Petroff. Optical emission from a charge-tunable quantum ring. *NATURE*, 405(6789):926–929, JUN 22 2000. 41
- [141] Evelin Weidner, Sylvain Combrie, Nguyen-Vi-Quynh Tran, Alfredo De Rossi, Julien Nagle, Simone Cassette, Anne Talneau, and Henri Benisty. Achievement of ultrahigh quality factors in GaAs photonic crystal membrane nanocavity. *APPLIED PHYSICS LETTERS*, 89(22), NOV 27 2006. 20
- [142] C Weisbuch, M Nishioka, A Ishikawa, and Y Arakawa. Observation of the coupled exciton-photon mode splitting in a semiconductor quantum

REFERENCES

- microcavity. *PHYSICAL REVIEW LETTERS*, 69(23):3314–3317, DEC 7 1992. 14
- [143] M Wimmer, SV Nair, and J Shumway. Biexciton recombination rates in self-assembled quantum dots. *PHYSICAL REVIEW B*, 73(16), APR 2006. 44
- [144] M Winger, A Badolato, KJ Hennessy, EL Hu, and A Imamoglu. Quantum Dot Spectroscopy Using Cavity Quantum Electrodynamics. *PHYSICAL REVIEW LETTERS*, 101(22), NOV 28 2008. 76
- [145] Martin Winger, Thomas Volz, Guillaume Tarel, Stefano Portolan, Antonio Badolato, Kevin J. Hennessy, Evelyn L. Hu, Alexios Beveratos, Jonathan Finley, Vincenzo Savona, and Atac Imamoglu. Explanation of Photon Correlations in the Far-Off-Resonance Optical Emission from a Quantum-Dot-Cavity System. *PHYSICAL REVIEW LETTERS*, 103(20), NOV 13 2009. 89
- [146] E Yablonovitch. Inhibited spontaneous emission in solid-state physics and electronics. *PHYSICAL REVIEW LETTERS*, 58(20):2059–2062, MAY 18 1987. 18
- [147] Makoto Yamaguchi, Takashi Asano, and Susumu Noda. Photon emission by nanocavity-enhanced quantum anti-Zeno effect in solid-state cavity quantum-electrodynamics. *OPTICS EXPRESS*, 16(22):18067–18081, OCT 27 2008. 89
- [148] T Yoshie, OB Shchekin, H Chen, DG Deppe, and A Scherer. Quantum dot photonic crystal lasers. *ELECTRONICS LETTERS*, 38(17):967–968, AUG 15 2002. 37
- [149] T Yoshie, A Scherer, J Hendrickson, G Khitrova, HM Gibbs, G Rupper, C Ell, OB Shchekin, and DG Deppe. Vacuum Rabi splitting with a single quantum dot in a photonic crystal nanocavity. *NATURE*, 432(7014):200–203, NOV 11 2004. 76, 89, 94

REFERENCES

- [150] RJ Young, RM Stevenson, P Atkinson, K Cooper, DA Ritchie, and AJ Shields. Improved fidelity of triggered entangled photons from single quantum dots. *NEW JOURNAL OF PHYSICS*, 8, FEB 23 2006. 37, 42
- [151] ZL Yuan, BE Kardynal, RM Stevenson, AJ Shields, CJ Lobo, K Cooper, NS Beattie, DA Ritchie, and M Pepper. Electrically driven single-photon source. *SCIENCE*, 295(5552):102–105, JAN 4 2002. 2, 7, 37
- [152] V Zwiller, T Aichele, W Seifert, J Persson, and O Benson. Generating visible single photons on demand with single InP quantum dots. *APPLIED PHYSICS LETTERS*, 82(10):1509–1511, MAR 2003. 7
- [153] V Zwiller, T Aichele, and O Benson. Quantum optics with single quantum dot devices. *NEW JOURNAL OF PHYSICS*, 6, JUL 29 2004. 2, 10